Title

Thermal Transport in Heterogeneous Nanostructures

Author

Li, Man

Publication Date

2022

Peer reviewed|Thesis/dissertation

UNIVERSITY OF CALIFORNIA

Los Angeles

Thermal Transport in Heterogeneous Nanostructures

A dissertation submitted in partial satisfaction

of the requirements for the degree

Doctor of Philosophy in Mechanical Engineering

by

Man Li

2022

ABSTRACT OF THE DISSERTATION

Thermal Transport in Heterogeneous Nanostructures

by

Man Li

Doctor of Philosophy in Mechanical Engineering

University of California, Los Angeles, 2022

Professor Yongjie Hu, Chair

Heterogeneous nanostructures involve nanoscale interfaces with different materials components, such as matrix and fillers in composites, stacking planer structures in electronics, and aggregates of nanomaterials. Thermal transport in heterogenous nanostructures is critical to the safety and performance of various applications ranging from high temperature turbines, microelectronics, solar cells, thermoelectrics, buildings' thermal management and so on. However, it remains challenging to achieve rational control of the thermal properties in heterogeneous nanostructures due to limitations in current characterization techniques and fundamental understandings of interface thermal transport. My PhD research focuses on developing new thermal measurement techniques and investigating fundamental interface transport mechanisms through the combination of experiments and modeling, to provide rational control over heterogeneous nanostructures for better addressing practical heat management and energy conversion problems using nanoengineering.

The study of thermal transport in heterogeneous nanostructures in my dissertation spans from technical development of new tools, experimental measurements at nanoscale interfaces and porous structures, and atomistic modelling of fundamental transport physics to practical device applications. First, I have developed a new metrology based on asymmetric beam time-domain thermoreflectance (AB-TDTR) that enables accurate measurements over three-dimensional thermal transport. Through the design of an asymmetric laser beam with controlled elliptical ratio and spot size, the experimental signals can be exploited to be dominantly sensitive to measure anisotropic thermal conductivity along the cross-plane or any specific in-plane directions. I have further applied this new approach to investigate anisotropic transport phenomena that enables unique applications. Second, I have explored the effects of crystal orientations and dipole-dipole interactions on interface thermal transport. In particular, for the first time, we have observed a record-high anisotropy ratio of 3.25 in the thermal boundary resistance across a prototype two-dimensional material, i.e., black phosphorus. Moreover, my study has resulted in the first observation of strong effects from long-range molecular dipole-dipole interactions on interface thermal transport. In addition, I have also investigated the heterogeneous integration of our recently developed new high thermal conductivity materials with prototyped high-power semiconductor, i.e., gallium nitride. Our in-situ measurement demonstrated substantially reduced hot-spot temperatures in devices using boron arsenide cooling substrates, beyond the best state-of-the-art HEMTs using diamond or silicon carbide. Lastly, I have investigated thermal transport in porous and mesoporous structures, including super-hydrophobic polymer aerogel, transparent mesoporous silica, and flexible tin selenide nanosheet films for applications in buildings, windows, and thermoelectric energy conversion.

The dissertation of Man Li is approved.

Adrienne G Lavine

Xiaochun Li

Laurent G. Pilon

Yongjie Hu, Committee Chair

University of California, Los Angeles

2022

Dedicated to my family

TABLE OF CONTENTS

LIST OF FIGURES

LIST OF TABLES

ACKNOWLEDGEMENTS

I would like to express my deepest appreciation to my PhD advisor, Professor Yongjie Hu. Without his strong support and invaluable advice, it would be impossible for me to successfully complete so many projects and finally finish my PhD thesis. I benefitted a lot from the inspiring and critical discussion with him, and appreciate the chance to perform multidisciplinary research in Hu's Lab. There is no doubt that his research philosophy on locating the right problem in a field and providing the fundamental understanding would be most precious gift in this journey.

Many thanks to Prof. Adrienne Lavine, Prof. Xiaochun Li, Prof. Laurent Pilon for serving on my PhD thesis committee and their invaluable comments. The knowledge about convective and radiative heat transfer from Prof. Adrienne Lavine and Prof. Laurent Pilon helped me a lot understand the heat transfer pathways in my projects. The generous sharing of research equipment from Prof. Xiaochun Li and Prof. Laurent Pilon saved me a lot of efforts.

I am also thankful to Prof. Sarah Tolbert, Prof. Bruce Dunn, Prof. Paul Weiss, Prof. Timothy Fisher, Prof. Tomas Base for their invaluable advice on our collaboration projects.

I am also grateful for the help from my labmates in Hu’s lab, Joon Sang Kang, Ming Ke, Hongyan Xia, Huan Wu, Huuduy Nguyen, Hang Fan, Nicolas Augustus Rongione, Zihao Qin, Ying Cui, Suixuan Li, Lingyun Dai, Jounghwan Choi, Changyu Deng, Chiyu Yang. Without their help, many of my research would be much more challenging and even impossible.

This endeavor would not have been possible without my family and girlfriend. Their accompany, sacrifice and love are the biggest support for me to fight with different challenges. There are no words to express my deepest thanks to them.

VITA

Education

2012 B.S. in Thermal engineering, Huazhong university of Science and Technology

Selected Publications (* denotes co-first author):

[1] **M. Li***, L. Dai*, Y. Hu, Machine Learning for Harnessing Thermal Energy: From Materials Discovery to System Optimization. ACS Energy Letters 7, 3204-3226 (2022).

[2] J. S. Kang*, **M. Li***, H. Wu*, H. Nguyen*, Y. Hu, Integration of boron arsenide cooling substrates into gallium nitride devices. Nature Electronics 4, 416–423 (2021).

[3] **M. Li**, J. S. Kang, H. D. Nguyen, H. Wu, T. Aoki, Y. Hu, Anisotropic Thermal Boundary Resistance across 2D Black Phosphorus: Experiment and Atomistic Modeling of Interfacial Energy Transport. Advanced Materials 31, 1901021 (2019).

[4] **M. Li***, J. S. Kang*, Y. Hu, Anisotropic thermal conductivity measurement using a new Asymmetric-Beam Time-Domain Thermoreflectance (AB-TDTR) method. Rev. Sci. Instrum. 89, 084901 (2018).

[5] **M. Li**, Z. Qin, Y. Cui, C. Yang, C. Deng, Y. Wang, J. S. Kang, H. Xia, Y. Hu, Ultralight and Flexible Monolithic Polymer Aerogel with Extraordinary Thermal Insulation by A Facile Ambient Process. Adv. Mater. Interfaces 6, 1900314 (2019).

[6] Y. Cui*, **M. Li***, Y. Hu, Emerging interface materials for electronics thermal management: Experiments, modeling, and new opportunities. J. Mater. Chem. C. 8, 10568 (2020).

[7] J. S. Kang, **M. Li**, H. Wu, H. Nguyen, Y. Hu, Experimental observation of high thermal conductivity in boron arsenide. Science 361, 575–578 (2018).

[8] J. S. Kang, **M. Li**, H. Wu, H. Nguyen, Y. Hu, Basic physical properties of cubic boron arsenide. Appl. Phys. Lett. 115, 122103 (2019).

[9] Z. Qin, **M. Li**, J Flohn, Y Hu, Thermal Management Materials for Energy-Efficient and Sustainable Future Buildings. Chem. Communications 12, 1-7 (2021).

[10] N. A. Rongione, **M. Li**, H. Wu, H. D. Nguyen, J. S. Kang, B. Ouyang, H. Xia, Y. Hu, High-Performance Solution-Processable Flexible SnSe Nanosheet Films for Lower Grade Waste Heat Recovery. Adv. Electron. Mater. 5, 1800774 (2019).

[11] Y. Yan, **M. Li**, S. King, T. Galy, M. Marszewski, J. S. Kang, L. Pilon, Y. Hu, S. H. Tolbert, Controlling Thermal Conductivity in Mesoporous Silica Films Using Pore Size and Nanoscale Architecture. J. Phys. Chem. Lett. 11, 3731–3737 (2020).

[12] S. C. King, **M. Li**, T. Galy, Y. Yan, J. S. Kang, V. M. Basile, Y. L. Li, M. Marszewski, L. Pilon, Y. Hu, S. H. Tolbert, Examining the role of atomic scale heterogeneity on the thermal conductivity of transparent, thermally insulating, mesoporous silica−titania thin films. J. Phys. Chem. C. 124, 27442–27452 (2020).

[13] Y. Cui, Z. Qin, H. Wu, **M. Li**, and Y. Hu, Self-assembled manufacturing for thermal management of wearable electronics and soft robotics, Nature Communications 12, 1284 (2021)

[14] J. S. Kang, H. Wu, **M. Li**, Y. Hu, Intrinsic Low Thermal Conductivity and Phonon Renormalization Due to Strong Anharmonicity of Single-Crystal Tin Selenide. Nano Lett. 19, 4941–4948 (2019).

[15] Y. Yan, S. C. King, **M. Li**, T. Galy, M. Marszewski, J. S. Kang, L. Pilon, Y. Hu, S. H. Tolbert, Exploring the Effect of Porous Structure on Thermal Conductivity in Templated Mesoporous Silica Films. J. Phys. Chem. C. 123, 21721–21730 (2019).

[16] H. D. Nguyen, J. S. Kang, **M. Li**, Y. Hu, High-performance field emission based on nanostructured tin selenide for nanoscale vacuum transistors. Nanoscale 11, 3129–3137 (2019).

[17] M. Marszewski, S. C. King, T. Galy, G. Kashanchi, A. Dashti, Y. Yan, **M. Li**, D. M. Butts, P. E. McNeil, E. Lan, B. Dunn, Y. Hu, S. H. Tolbert, L. Pilon, Transparent silica aerogel slabs synthesized from nanoparticle colloidal suspensions at near ambient conditions on omniphobic liquid substrates. J. Colloid Interface Sci. 606, 884-897 (2022).

[18] M. Ke, H. D. Nguyen, H. Fan, **M. Li**, H. Wu, Y. Hu, Complementary doping of van der Waals materials through controlled intercalation for monolithically integrated electronics. Nano Res. 13, 1369–1375 (2020).

[19] D. M. Butts, P. E. McNeil, M. Marszewski, E. Lan, T. Galy, **M. Li**, J. S. Kang, D. Ashby, S. King, S. H. Tolbert, Y. Hu, L. Pilon, B. S. Dunn, Engineering mesoporous silica for superior optical and thermal properties. MRS Energy Sustain. 7, E39 (2020).

CHAPTER 1

Introduction

1.1 Motivation and background

With the continuing miniaturization of electronic and photonic devices, the power density increases extremely and heat dissipation becomes one of the key technological challenges for the semiconductor industry[1]. In the meanwhile, environmental problems caused by our energy demands have been stressed the needs of sustainable technologies[2] such as solar cells and thermoelectric devices. To address these challenges, manipulating and managing heat transfer is critical to achieving their high performance[3,4]. The introduction of nanostructures has made substantial contributions in the recent studies[5,6]. Therefore, my thesis study focus on investigating thermal transport across nanoscale interfaces and aims to develop fundamental understanding for interface thermal transport that is essential to the future development for information and energy technologies.

During the last two decades, intensive studies have been made on nanoscale thermal transport[7,8]. The development of thermal characterization techniques such as 3ω, time-domain thermoreflectance, Raman thermometry and micro-bridge have enabled measurements from macroscopic samples to nanostructures[9–12]. The fundamental knowledge of heat conduction based on phonons, which is the quantized atomic vibrations in crystal, have been greatly broaden due to the experimental discovery of new phonon transport phenomenon, such as diffusive to ballistic phonon transport in nanostructures, spectral mapping of phonon transport in crystals, and unique

thermal transport properties of low-dimensional materials[13–16]. On the theory side, first principles calculation[17,18] provides the recent breakthrough in predictive determination of thermal conductivity in bulk solids. Density functional theory has been applied to calculate interatomic force constants and phonon scattering. Combined with Boltzmann transport equation, thermal conductivity can be calculated only based on the physical constants and atomic structure of elements without any fitting parameters. The metrology is called first principles calculation of phonon transport Taking advantage of these predictive capability, people can find the right directions to explore new materials with extraordinary thermal properties, for example, the ultrahigh thermal conductivity solid, boron arsenide[19]. Despite these great success, most of the current research have been focused on homogeneous systems. However, many aspects in thermal transport has yet to be explored for systems involving heterogenous nanostructures, such as composites, porous materials, alloys and polycrystals.

However, thermal transport in heterogeneous materials is much more complicated than in homogeneous materials. For example, there are numerous effective thermal conductivity models for composites, implying none of them works well for a relatively large group of composites[20]. The main challenges include the irregular structures, lack of periodicity, thermal boundary resistance between the homogeneous counterparts, anisotropic properties of the component materials and so on. In mesoporous materials, the nanoscale pores impose more complexity on the phonon transport in the porous network. Due to the nanoscale characteristic length, phonons scatter more frequently than in the dense counterpart and thermal conductivity can be suppressed significantly, for example more than 90 % with porosity less than 50 % in holy silicon[21]. In alloys, the atomic level of disorder also strongly affects the thermal transport properties[22]. Although the so-called first principle calculations can explain well the experimental data like the U shape trend between

thermal conductivity and germanium concentration in silicon germanium alloy, the virtual crystal approximation is dispensable[23]. The effects of variation of local interatomic forces and random distribution of mass on phonon transport are still unclear. For composite, the problems become even challenging. The thermal resistance between different phases can usually dominate the heat conduction in composites. However, the interfacial thermal transport is determined by a lot of factors, e.g. the crystal directions, bonding energy between materials, roughness and disorder at the interfaces, most of which are not well studied[24]. Obviously, the thermal properties of heterogenous materials are determined by the nanoscale features, from the nanoscale structures to the atomic level interfaces and disorder.

Understanding thermal transport in heterogeneous nanostructures still remains challenging, despite their wide applications such as in thermal interfaces, thermoelectrics, and supercapacitors[25–27]. For example, it is well known that alloys with hierarchical architectures can significantly improve the thermoelectric figure of merit[28]. But it's unclear how the grain boundaries affect electron and phonon transport. There are still many unknow things about thermal transport at interfaces, such as the crystal orientation and dipole-dipole effects. Based on our fundamental understanding of interfaces, can we design electronics devices with good thermal management? Composites with graphene fillers had been studied as a highly efficient thermal interface material[29]. But the extremely anisotropic thermal properties of graphene made the fundamental understanding of thermal transport in composites with graphene fillers extremely challenging. To solve this problem, the first challenge is to develop new thermal characterization techniques. Mesoporous silica held promise for the transparent thermal insulation applications due to its low thermal conductivity and optical transparency for the visible light. But the previous measurements were performed on samples with relatively narrow porosity range. The effects of mesoporous structures

on vibrational modes in silica are also not clear[30]. A systematic study of thermal properties of mesoporous solid is urgently needed.

1.2 Outline of the dissertation

In this dissertation, I will present thermal transport across heterogeneous nanostructures as well as the application in thermal management and energy conversion.

In chapter 2, I introduce a new metrology based on asymmetric beam time-domain thermoreflectance (AB-TDTR), developed to measure three-dimensional anisotropic thermal transport by extending the conventional TDTR technique ultrafast pump-probe spectroscopy which is called time-domain thermoreflectance (TDTR) method for thermal conductivity measurement. Using an elliptical laser beam with controlled elliptical ratio and spot size, the experimental signals can be exploited to be dominantly sensitive to measure thermal conductivity along the cross-plane or any specific in-plane directions. An analytic solution for a multi-layer system is derived for the AB-TDTR signal in response to the periodical pulse, elliptical laser beam, and heating geometry, to extract the anisotropic thermal conductivity from experimental measurement. Examples with experimental data are given for various materials with in-plane thermal conductivity from 5 W/mK to 2000W/mK, including isotropic materials (silicon, boron phosphide, boron nitride), transversely isotropic materials (graphite, quartz, sapphire) and transversely anisotropic materials (black phosphorus). Furthermore, a detailed sensitivity analysis is conducted to guide the optimal setting of experimental configurations for different materials.

In Chapter 3, I report the observation of a highly anisotropic TBR across a prototype two-dimensional material, i.e., black phosphorus through crystal orientation dependent interfacial transport study. Atomistic ab-initio calculations are conducted to analyze the anisotropic and

temperature-dependent TBR using density functional theory calculated full phonon dispersion relation and molecular dynamics simulation. This study provides a critical fundamental understanding of interfacial thermal transport and TBR-structure relationships

In Chapter 4, I reveal the significant thermal transport contribution by long-range dipole-dipole interaction between molecules. By delicate design of molecular structures, we altered the dipole moment of self-assembled monolayer without changing the short-range interactions, i.e., covalent and van der Waals interactions. The thermal transport enhancement is verified with molecular dynamics simulations, where the dipole-dipole interactions can be artificially turn on and off.

In Chapter 5, I report the heterogeneous integration of boron arsenide (BAs) and boron phosphide (BP), with different metals and the prototype high power semiconductor gallium nitride (GaN). In addition, multiscale and non-equilibrium simulation were performed to quantify device-level hot spot temperatures in both diffusive and ballistic regimes. The study represents an important step towards device integration of emerging high thermal condutivity materials for power electronics applications and establishes a benchmark performance in comparison with the current state of the arts.

In Chapter 6, I report a facile ambient processing approach to synthesize a highly insulating and flexible monolithic polyvinyl chloride aerogel. We measured the thermal conductivity and performed thermal modeling to understand the thermal conductivity contributions from different heat transport pathways.

In Chapter 7, I report a low-cost and scalable solution process to fabricate a nanostructured tin selenide thin film and demonstrate a record-high thermoelectric performance near room temperature. Moreover, I demonstrate that the tin selenide thin film can be readily implemented

on flexible plastic substrates and preserve the high thermoelectric performance over 1000 bending cycles. Together, our study demonstrates a low-cost and scalable approach to achieve high-performance flexible thin film energy harvesting devices to power electronics and sensors near room temperature.

In Chapter 8, I report the thermal transport measurement of mesoporous amorphous silica and observe strong correlations between nanoarchitecture and effective thermal conductivity. Three semi-classical thermal models are constructed to interpret the thermal conductivity with consideration of the characteristic size effects on vibrational modes. The fundamental understanding of vibrational modes transport in mesoporous silica is verified by comparing the experimental results with simulations based on spectral Boltzmann transport equation.

CHAPTER 2

Anisotropic Thermal Conductivity Measurement using Asymmetric Beam Time-Domain Thermoreflectance (AB-TDTR) Method

2.1 Introduction to anisotropic thermal measurements

Anisotropic thermal transport is of both fundamental and practical importance. Orientation-dependent thermal conductivity has been observed in many materials systems because of their highly asymmetric crystal structures[8]. For example, the in-plane thermal conductivity of most familiar two-dimensional (2D) materials, e.g. graphene, hexagonal boron nitride, and molybdenum disulfide can be more than 10 times, even 100 times higher than their cross-plane thermal conductivity[31–37]. Furthermore, some 2D materials like black phosphorus can have three-dimensional anisotropy, i.e., the in-plane thermal conductivity also depends on crystal orientation[37–43]. Importantly, the interaction between 2D lattices and external defects has been revealed to be highly anisotropic and phonon mode dependent through in situ thermal-electrochemical characterizations[37]. Polymers can also exhibit strong orientation dependent thermal conductivity, like more than 40 times larger thermal conductivity along chain direction than that of the transverse direction in polyethylene[44,45]. In addition to these van der Waals and covalent bonding mixed system, materials with single form of bonding can also possess anisotropic thermal conductivity, like quartz, uranium dioxide, perovskites and so on[46–48]. Even materials considered as isotropic materials can display anisotropic thermal transport due to nonhomogeneous grains and defects during crystal growth, high aspect ratio nanostructure[49–51], superlattice or

heterostructures[52], and measurement or device heating geometries[14,53,54]. For many applications, understanding the anisotropic thermal properties is a key merit to evaluate performance, e.g. thermal management in electronics[55,56], nuclear reactor design and safety[47,57], thermally stable photovoltaic conversion[48,58], directional thermoelectric conversion efficiency[59,60] and thermal regulation[37,61]. However, accurately measuring the anisotropic thermal transport remains challenging, despite that significant progress has been made recently.

The traditional spirit of measuring anisotropic thermal conductivity is to align temperature gradient and heat flux along the sample orientation that is of interest, so that no temperature gradient exists in any other directions, like steady-state methods and transient laser flash[62–65]. The prerequisite of big size samples or specified geometry limits their application for anisotropic measurement on novel materials. Modified 3ω-method and micro-bridge techniques can enable anisotropic thermal conductivity measurement on small samples[66–74], however, these methods usually require complicated microfabrications and materials processing to produce heating elements or resistive temperature sensors on the sample surface. Compared with micro-fabricated devices and 3ω method, the pump-probe optical spectroscopies such as time-domain thermoreflectance (TDTR), frequency-domain thermoreflectance, and transient thermal grating techniques can be used to perform non-contact and fast thermal conductivity measurement on both bulk and nanoscale samples[75–81], while isotropic heat conduction model was assumed in its early stage of development. To facilitate directional thermal conductivity measurement, TDTR has been recently modified to improve the measurement sensitivity to in-plane heat conduction[82–84]. Beam offset method was developed, but requires extra setups for translating beam positions and its data fitting under anisotropic heat conduction model can be time-consuming if the material is three-

dimensional anisotropic[83]. Variable circular spot size has been applied but this method is not able to distinguish the in-plane anisotropy[84].

Here we develop a new metrology based on asymmetric beam time-domain thermoreflectance (AB-TDTR) to measure anisotropic thermal transport along cross-plane or any in-plane directions. The AB-TDTR signal sensitivity to thermal transport along different in-plane directions is decoupled and exploited using an elliptical laser beam with controlled elliptical ratio and spot size, to accomplish fast three-dimensional anisotropic thermal conductivity measurement. We first develop a mathematical model of anisotropic heat diffusion in multilayers heated by elliptical laser beam and provide the working principle of AB-TDTR method. Sensitivity analysis is conducted to guide the setting of experimental configuration for various materials. Demonstration experiment is performed on standard materials, including silicon (Si), cubic boron nitride (c-BN), boron phosphide, graphite, sapphire, quartz. Finally, the angle dependent thermal conductivity of black phosphorus is measured and compared with theoretical prediction to show the capability of our approach to measure thermal conductivity of three-dimensional anisotropic materials.

2.2 Mathematical model and experimental principles

2.2.1 Frequency domain solution to multilayer heat conduction equation with anisotropic thermal conductivity and asymmetric laser heating

For TDTR measurement, a thin metal film is coated on the sample surface to serve as a thermal transducer, which is instantaneously heated by absorbing femtosecond pump laser pulses. This metal film also serves as the temperature sensor by reflecting a probe beam to photo diode

with its reflectivity linearly proportional to temperature under a small temperature change. Thus, the transient temperature decay with time can be continuously detected by controlling the delay time between pump and probe beams using a mechanical stage and fitted with a multilayer thermal model to obtain the thermal conductivity (κ) of the sample. To achieve high signal to noise ratio, the laser pulses are modulated, and lock-in technique are used to detect temperature response at modulation frequency f_0. Under the assumption that temperature response of the sample to laser heating is both linear and time invariant, the detected signal by lock-in amplifier was given by Cahill as[80]

$$Z(f_0) = \frac{\beta Q Q_s}{T_s^2} \sum_{k=-\infty}^{\infty} H(2\pi f_0 + 2\pi f_s k) e^{2\pi i f_s k \tau} \qquad (2\text{-}1)$$

where H(f) is the frequency response of sample heated periodically, β indicating temperature coefficient of reflectivity and electronic gains, Q and Q_s power of each pump pulse and probe pulse respectively, T_s the period of laser pulses, f_0 the modulation frequency, f_s the frequency of laser pulses, τ the delay time between pump beam and probe beam. The detected in-phase signal V_{in} and out-of-phase signal V_{out} by lock-in amplifier are real part and imaginary part of $Z(f_0)$. Since the phase signal $\tan^{-1}(V_{out}/V_{in})$ can exclude effects from some of the noise signals, we would discuss only the phase signals in the rest sections. For conventional TDTR, more details of experimental setup and derivation of H(f) can be found in literatures[80,81]. As follows, the frequency response of anisotropic materials with elliptical laser heating is derived for analyzing AB-TDTR measurement signal.

Different from isotropic medium, where heat flux is always along temperature gradient direction, heat conduction in anisotropic medium is much more complicated, where heat flux is related with temperature gradient along all the directions. Mathematically, it can be expressed in cartesian coordinates as[46]

$$q_i = -\sum_{j=1}^{3} \kappa_{ij} \frac{\partial T}{\partial x_j} \quad (2\text{-}2)$$

where i, j mean the directions and T is temperature. Nine κ_{ij} elements constitute a second rank tensor,

$$\kappa = \begin{bmatrix} \kappa_{xx} & \kappa_{xy} & \kappa_{xz} \\ \kappa_{yx} & \kappa_{yy} & \kappa_{yz} \\ \kappa_{zx} & \kappa_{zy} & \kappa_{zz} \end{bmatrix} \quad (2\text{-}3)$$

which is called thermal conductivity tensor. When the Cartesian coordinates are along the principal thermal transport axes, the off-diagonal elements in thermal conductivity tensor would vanish and the anisotropic heat conduction equation in AB-TDTR measurement is expressed as

$$\kappa_{xx} \frac{\partial^2 T}{\partial x^2} + \kappa_{yy} \frac{\partial^2 T}{\partial y^2} + \kappa_{zz} \frac{\partial^2 T}{\partial z^2} + S = C_v \frac{\partial T}{\partial t} \quad (2\text{-}4)$$

where S is the heat source term, C_v volumetric heat capacity of anisotropic solids[46]. In the multi-layers model of AB-TDTR experiment, heat source term is zero. The laser heating term $I(x, y) = \frac{2A_0}{\pi w_{0,x} w_{0,y}} \exp\left(-\frac{2x^2}{{w_{0,x}}^2} - \frac{2y^2}{{w_{0,y}}^2}\right)$ is treated as a heat flux boundary condition, where A_0 is the absorbed power of pump beam, $w_{0,x}$ and $w_{0,y}$ the $1/e^2$ semi-minor axis length and $1/e^2$ semi-major axis length respectively as shown in Fig. 1(a), which mean the distance from ellipse center to points on major axis and minor axis where laser intensity is $1/e^2$ of the peak intensity. In the following sections, the $1/e^2$ will not be explicitly given. To obtain frequency-domain solution of temperature response, heat conduction equation is written as after Fourier transformation

$$\frac{\partial^2 \hat{T}}{\partial z^2} = \lambda \hat{T} \quad (2\text{-}5)$$

$$\lambda = \frac{2\pi i f C_v}{\kappa_{zz}} + \frac{\kappa_{xx}}{\kappa_{zz}} \xi^2 + \frac{\kappa_{yy}}{\kappa_{zz}} \eta^2 \quad (2\text{-}6)$$

where $\hat{T}$ is temperature in frequency domain, f, ξ and η the variables in Fourier space corresponding to t, x and y. This one-dimensional multi-layer heat conduction equation was solved by Schmidt et al. following the approach of Carslaw and Jaegar[81,85]

$$\hat{T}(f,\xi,\eta) = \left(-\frac{D}{C}\right)\frac{A_0}{2\pi}\exp\left(-\frac{{w_0}^2\xi^2+{w_s}^2\eta^2}{8}\right) \quad (2\text{-}7)$$

where C and D are elements of transfer matrix as function of thickness and λ, indicating geometry and thermal properties of each layer[81]. After inverse Fourier transformation and taking the elliptical shape of probe beam into account, the frequency response function of AB-TDTR is derived as

$$H(f) = \frac{A_0 A_s}{4\pi^2}\iint_{-\infty}^{\infty}\left(-\frac{D}{C}\right)\exp\left(-\frac{({w_{0,x}}^2+{w_{s,x}}^2)\xi^2+({w_{0,y}}^2+{w_{s,y}}^2)\eta^2}{8}\right)d\xi d\eta \quad (2\text{-}8)$$

where A_s is the reflected power of probe beam, $w_{s,x}$ and $w_{s,y}$ the semi-minor length and semi-major length of probe beam. Here it should be noted that the only important characteristic sizes of laser beams in AB-TDTR are the root mean square of the minor axis length $D_x = 2\sqrt{\frac{{w_{0,x}}^2+{w_{s,x}}^2}{2}}$ and of the major axis length $D_y = 2\sqrt{\frac{{w_{0,y}}^2+{w_{s,y}}^2}{2}}$.

Note, the alignment between the elliptical beams and the principal crystal directions can be controlled using a rotating sample holder (Figure. 2.1 (a)). Even under the coordinates that the asymmetric beams are not aligned with the principal crystal directions, when elliptical beams with very high elliptical ratio is used and cross-plane is along z axis, the heat conduction would be two-dimensional in x-z plane and the terms involving $\frac{\partial^2 T}{\partial x \partial y}$, $\frac{\partial^2 T}{\partial x \partial z}$ and $\frac{\partial^2 T}{\partial y \partial z}$ in heat conduction equation would also vanish[46]. The mathematical form of anisotropic heat conduction would stay unchanged as Eqn. (2-4). More discussion about anisotropic heat conduction will be given in the following for the demonstrative experiment on black phosphorus (BPh).

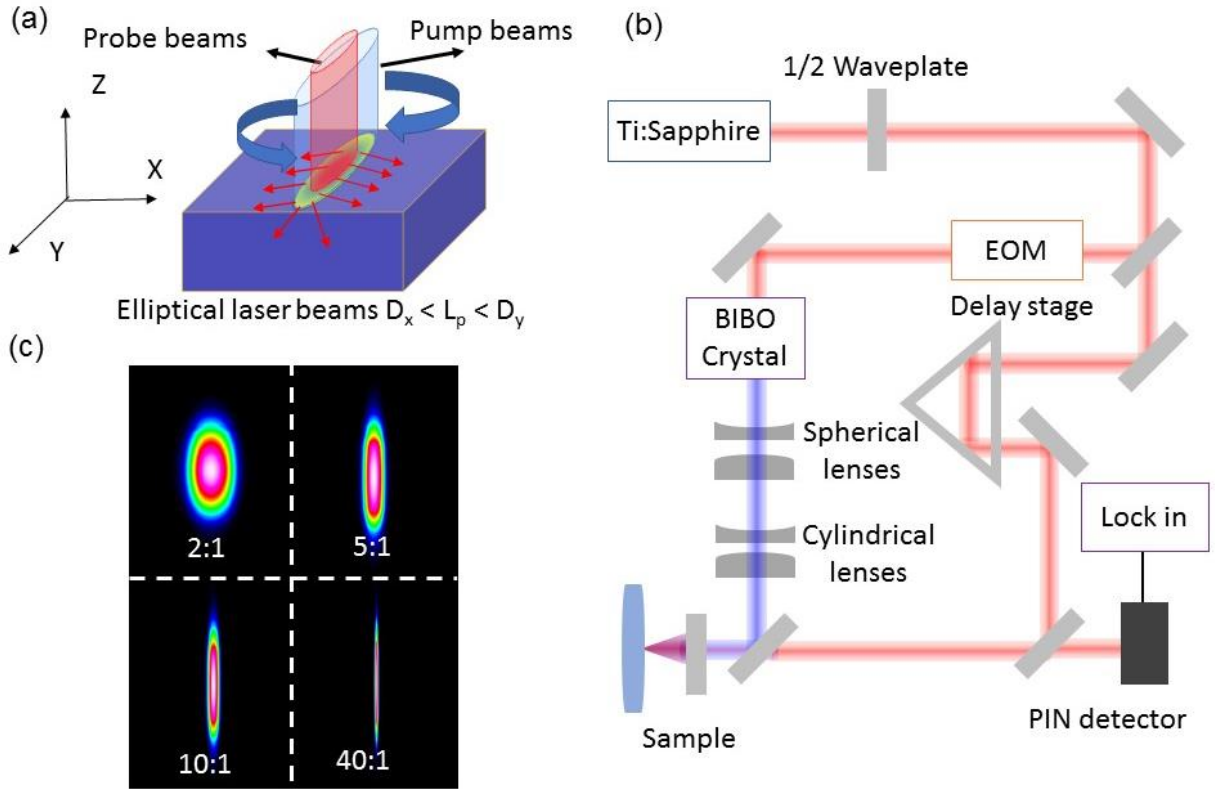

Figure 2.1 Working principles of the asymmetric beam TDTR (AB-TDTR) for measuring anisotropic thermal conductivity. (a) Schematic illustrates the surface temperature distribution of samples heated by an elliptical laser beam. The major principal axis (y) and minor axis (x) represents the longest and shortest diameter of the laser beam. To measure anisotropic thermal conductivity, the heat conduction direction of interest is aligned to be in parallel with the y axis. (b) Schematic of an AB-TDTR setup. (c) Four beam profiler images of laser beams with different aspect ratios controlled by the cylindrical lens.

2.2.2 Experimental principles and sensitivity analysis

The setup schematic of AB-TDTR is shown in Figure 2.1 (b). In addition to the spherical lenses used in normal TDTR setup, a pair of cylindrical lenses are included to tune the elliptical shape of laser beams. The combination of using both cylindrical and sphere lens allows the control of both principal axis lengths (D_x and D_y) independently. The use of asymmetric beams instead of

circular beams in AB-TDTR measurement enables the capability to precisely measure thermal conductivity along arbitrary directions of interest.

The key design of AB-TDTR is to decouple thermal transport along different directions. For conventional TDTR experiment, high modulation frequency and large beam spot size are usually used so that the thermal penetration depth ($L_p = \sqrt{\kappa/\omega_0 C_V}$) is much smaller than laser spot size. In this case, the temperature gradient is only along the cross-plane direction. By reducing the laser spot size to be close to or smaller than the in-plane L_p, in-plane thermal transport can affect the detection signal, however, it is not possible to distinguish thermal conductivity difference between different in-plane directions due to the circular beam symmetry. For AB-TDTR experiment, the D_x and D_y can be controlled to be much longer and close to the in-plane L_p respectively, so that the detected signal is dominantly sensitive to the heat transfer along D_x (versus D_y) direction. Therefore, AB-TDTR enables the precise measurement of anisotropic in-plane thermal conductivity.

In addition, it should be noted that the elliptical modeling for AB-TDTR can minimize the measurement uncertainty from an imperfect laser beam profile. In conventional TDTR, circular beams are usually assumed in data analysis despite that the actual beam shape always deviates from a perfect circular shape. Such a deviation from a perfect circular beam to a practically elliptical beam can bring non-negligible errors for the fitted thermal conductivity. A hypothetical example is given below with the following listed parameters: isotropic thermal conductivity κ = 100 W/mK, volumetric heat capacity $C_v = 2\times10^6$ J/m^{3}K, interfacial thermal conductance $G = 1\times10^8$ W/m^{2}K. The actual elliptical ratio of is 1.25 and D_x is 5 μm. Under modulation frequency of 1 MHz and a circular beam assumption, the fitted κ would be 87 W/mK, 13 % lower than the actual

value. Therefore, the anisotropic mathematical modeling presented for the AB-TDTR would avoid such an error to improve measurement accuracy.

To provide a guideline for optimizing experimental settings for different materials, a comprehensive sensitivity analysis is conducted in this work by varying materials anisotropy, beam spot size and modulation frequency. Considering the generality of this analysis, some properties are fixed at most common values. For example, the volumetric heat capacity is fixed at 2×10^6 J/m^{3}K since most of solid materials at room temperature have values from $1\sim3\times10^6$ J/m^{3}K[86], while G between our hypothetical sample and aluminum is 1×10^8 W/m^{2}K, located in the most common range of $1\times10^{7\sim9}$ W/m^{2}K[7]. The sensitivity of TDTR phase signal to a certain parameter α was defined as[87]

$$S_\alpha = \frac{\partial \ln(\theta)}{\partial \ln(\alpha)} \quad (2\text{-}9)$$

where α can be κ_{xx}, κ_{yy}. Here, a sensitivity ratio is defined as $\gamma = S_{\kappa_{xx}}/S_{\kappa_{yy}}$, representing the key metric to quantitatively determine the measurement uncertainty due to the two competing fitting parameters, i.e. κ_{xx}, κ_{yy}. The sensitivity ratio as a function of thermal conductivity and beam diameter are plotted as a color couture in Figure. 2.2.

Figure. 2.2 clearly shows that the Sκ_{xx} is much higher than S_κ_{yy} for most D_x and materials thermal conductivity, which verifies that the measurement signal is dominantly sensitive to κ_{xx}. The sensitivity ratio depends on the beam spot size, κ_{xx}, κ_{yy} and modulation frequency. Small D_x, high frequency and large κ_{xx} contribute to a relatively small γ, which can be explained by the comparison between in-plane L_p and spot size. For example, when the in-plane thermal conductivity is 10000 W/mK, the in-plane L_p is 40 μm at modulation frequency of 1 MHz. If the D_x is only 0.5 μm, the D_y will be 50 μm given the fixed elliptical ratio of 100, close to the in-plane

L_p, which means the y-direction temperature gradient probed by the laser beam is significant. Therefore, the signal would not be solely determined by the κ_{xx} in this case. Although the effect of κ_{zz} on γ is relatively weak compared with other parameters, it is still clear that high cross-plane thermal conductivity can increase the value of γ. The reason is that higher κ_{zz} means longer cross-plane L_p, which indicates the detection depth along cross-plane direction is deeper. As heat dissipate farther beneath the top surface, the effective spot size is larger in the deeper layer. Thus, in-plane L_p tenders to be even smaller than the effective D_y. As a result, the signal sensitivity to κ_{yy} becomes weak.

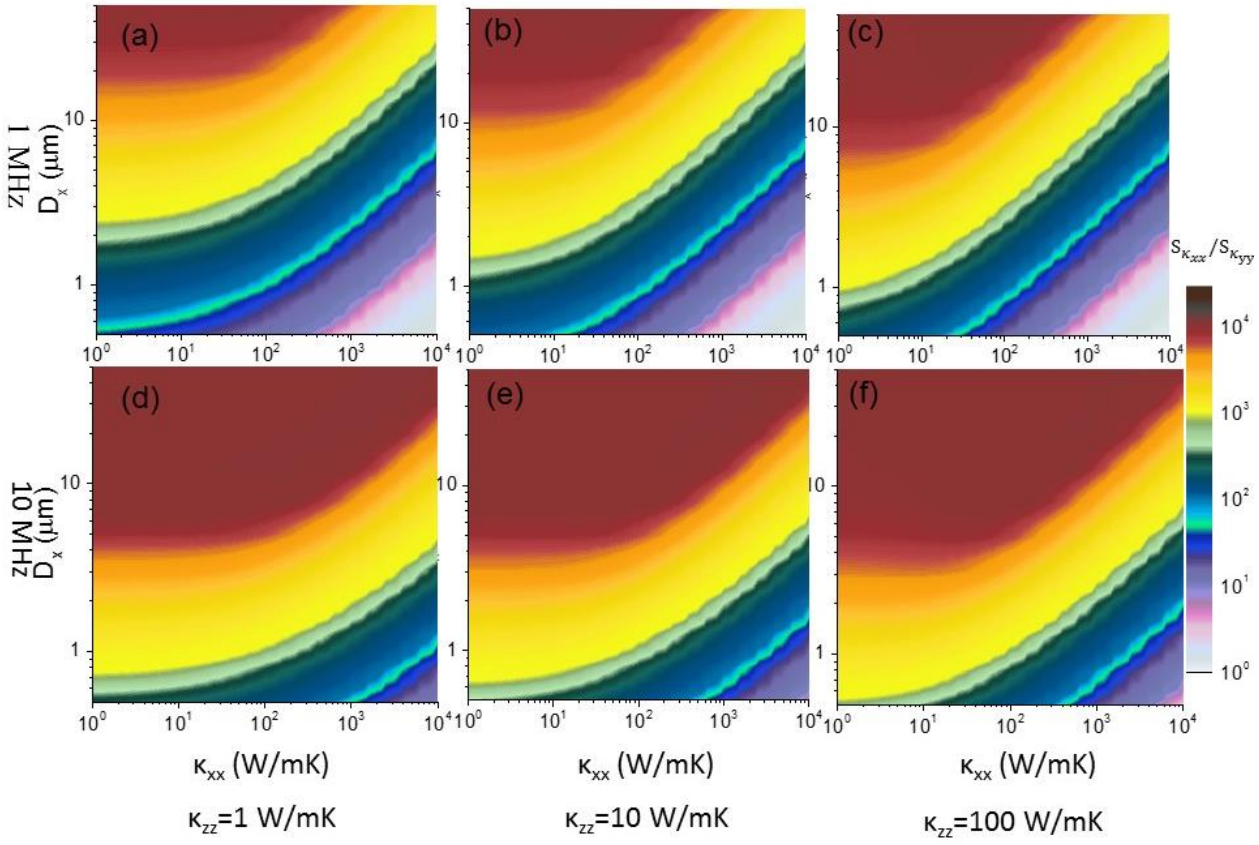

Figure 2.2 Sensitivity contour for design setting of the modulation frequency, the laser spot size for materials with different thermal conductivity and anisotropy. The amplitude of the color scale is defined as the ratio of phase sensitivity, i.e. $S_{\kappa_{xx}}/S_{\kappa_{yy}}$, and calculated at a fixed delay time of 100 ps and a fixed elliptical ratio of laser beam of 100. (a), (b) and (c) give the sensitivity analysis for different materials with κ_{zz} from 1~100 W/mK at modulation frequency of 10 MHz. while (d), (e) and (f) are corresponding to 1MHz. Some basic rules can be found from the comparison. Higher modulation frequency and bigger spot size can enhance sensitivity ratio of κ_{xx} over κ_{yy}. Smaller spot size can be used when materials have smaller κ_{zz}.

We have also calculated the absolute values of the sensitivity of AB-TDTR and plotted it in Figure 2.3. To make a quantitative comparison with state-of-the-art anisotropic measurement techniques, we have also performed the sensitivity calculations of the beam-offset TDTR technique and plotted in the following Figure 2.4. The calculation parameters for absolute sensitivity analysis of the following AB-TDTR and beam-offset TDTR are kept the same with

those used for Figure 2.2. In comparison of the two techniques, the absolution sensitivity results show that the AB-TDTR method has higher absolute sensitivity than the beam-offset TDTR for most of the thermal conductivity and spot size ranges.

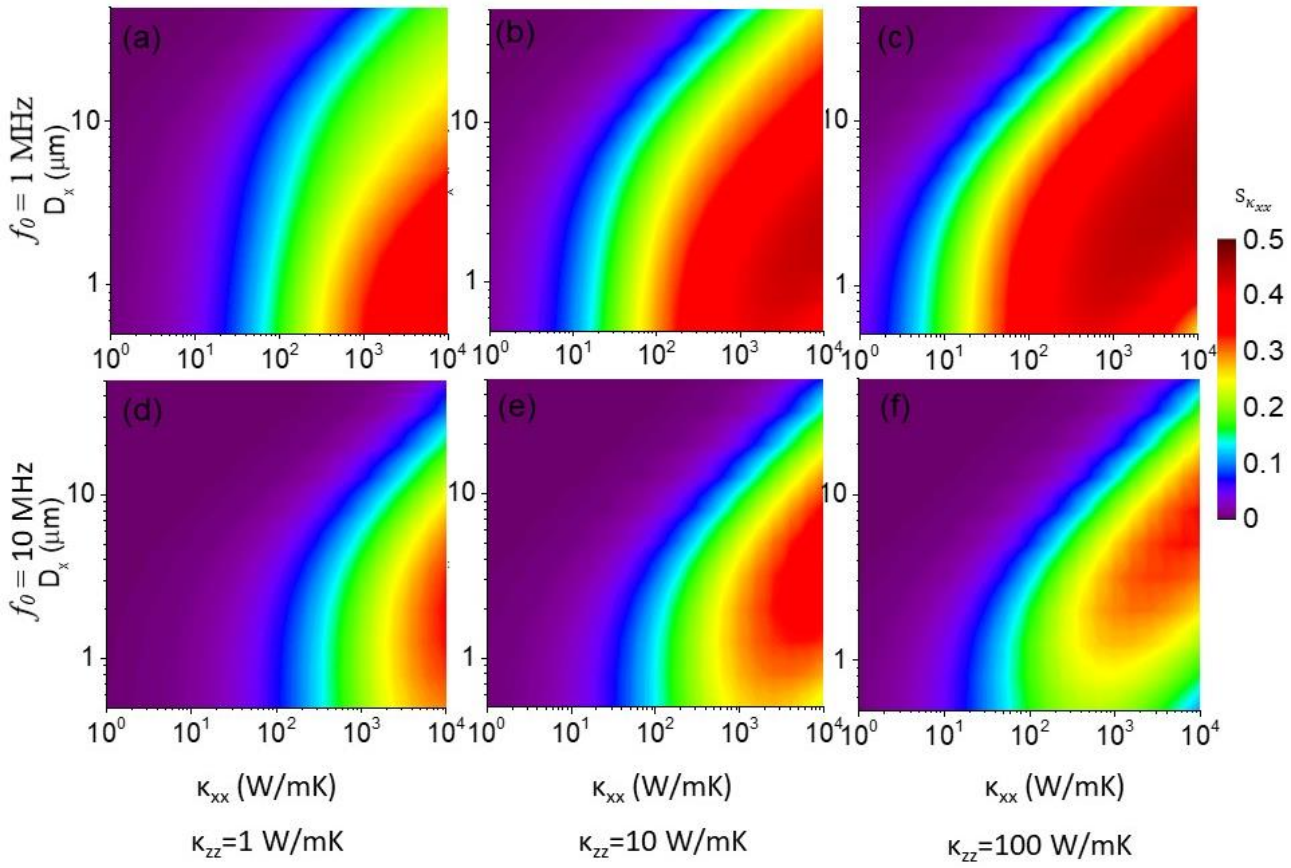

Figure 2.3 The absolute sensitivity to $\boldsymbol{\kappa_{xx}}$ for the AB-TDTR method. Simulation parameters are kept the same as Figure 2.2.

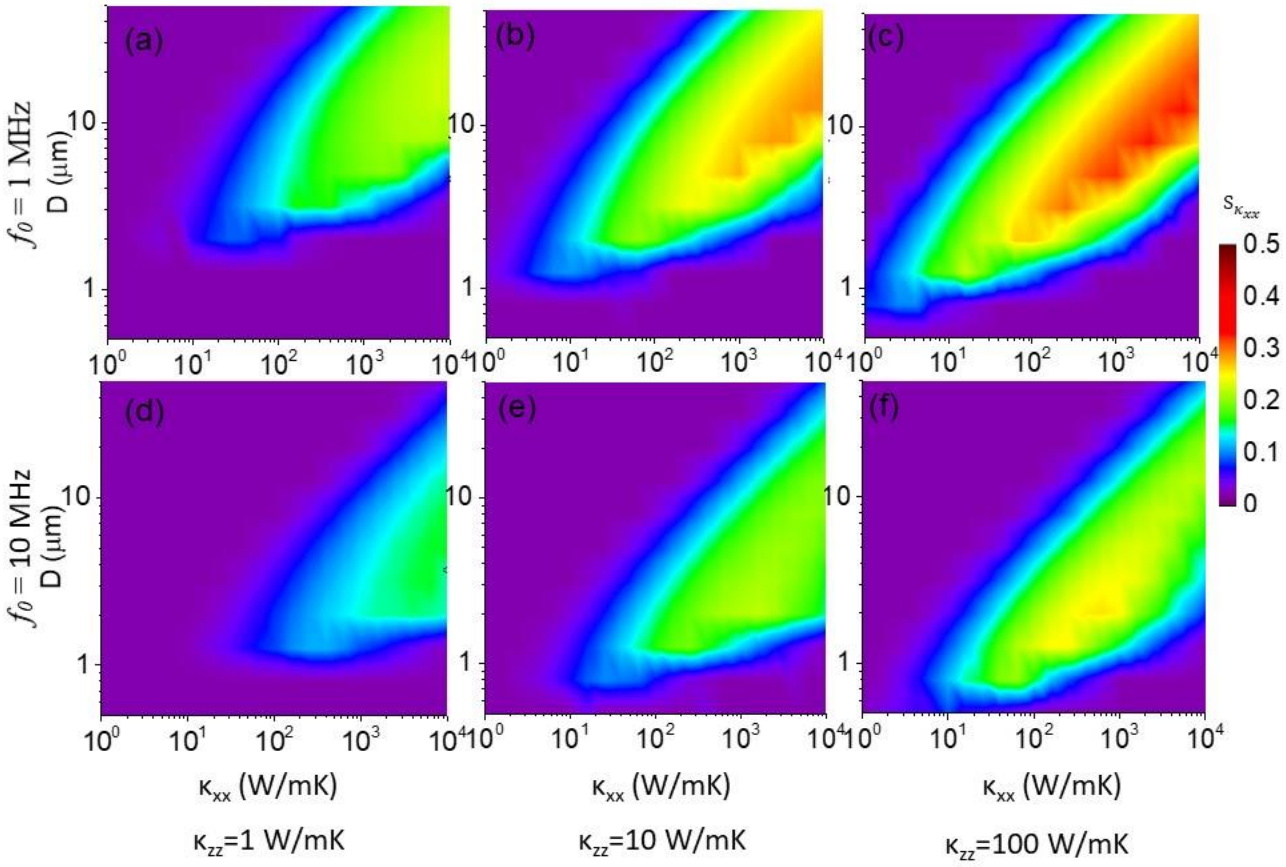

Figure 2.4 The absolute sensitivity to $\boldsymbol{\kappa_{xx}}$ for the beam-offset TDTR method. Simulation parameters are kept the same as Figure 2.2.

2.3 Demonstrative AB-TDTR on various materials

2.3.1 Experimental details

Examples of AB-TDTR experiments are conducted on different materials from isotropic materials, 2D anisotropic materials, to 3D anisotropic materials. The optical setup of AB-TDTR is illustrated in Figure. 2.1 (b). In this setup, a Ti:Sapphire oscillator (Tsunami, Spectra-physics) generates a train of femtosecond laser pulses with 800 nm wavelength and 80 MHz repetition rate.

A polarizing beam splitter divides the beam into a pump and a probe pulse. The pump beam is sinusoidally modulated by the electro-optic modulator (EOM) typically from 1 MHz to 20 MHz and fundamental frequency of pump beam was doubled by (BIBO), corresponding to the wavelength of 400 nm. Probe beam is delayed using mechanical delay stage from 0 to 6000 ps with a resolution of less than 1 ps. The signal is detected by a lock-in amplifier at modulation frequency after the photo diode converts the reflected probe beam intensity into electrical signal. Before the recombination of the pump and probe beams, four lenses are introduced to tune the size and shape of the pump beam, two of which are cylindrical lenses and the other two are spherical lenses as shown in Figure. 2.1 (b). By controlling the distance of the plano-concave and plano-convex lenses, the beam size can be manipulated. And the elliptical ratio can be tuned by controlling the distance between convex and concave cylindrical lens as shown in Figure. 2.1 (c). For all the samples in the following sections, 80nm aluminum films are coated on them to serve as transducer by using e-beam evaporator. To evaluate the measurement reliability, 10 measurements are performed at each sample condition for all the following experiments.

2.3.2 Measurement of isotropic materials ($\kappa_{xx} = \kappa_{yy} = \kappa_{zz}$)

First, the AB-TDTR experiment is conducted on prototype isotropic materials, including silicon, cubic boron nitride, and cubic boron phosphide. As the first step, the cross-plane thermal conductivity κ_{zz} is accurately measured. Based on the sensitivity analysis (Figure. 2.2), the experiment is designed to achieve high sensitivity to the cross-plane thermal transport, for example, using a big beam spot size (D_x ~30 μm) and high modulation frequency (9.8 MHz). As an example, The cross-plane thermal conductivity of the silicon sample was measured as 138.2 ± 5.1 W/mK, consistent with literature[88,89]. Then by using smaller spot size D_x = 7 μm and D_y = 210 μm and

small modulation frequency of 1.1 MHz, the phase data with delay time from 500 ps to 5000 ps was probed as displayed in Figure. 2.5. By fitting with the thermal diffusion model described in section II. A, the in-plane thermal conductivity can be obtained as 146.4±5.2 W/mK, within 10% error compared with κ_{zz}. Since silicon is isotropic, the in-plane thermal conductivity is supposed to be same with the cross-plane thermal conductivity, which is consistent with our experimental results. We also applied our AB-TDTR to measure cubic boron nitride and boron phosphide and summarize data in Figure. 2.8[53,90].

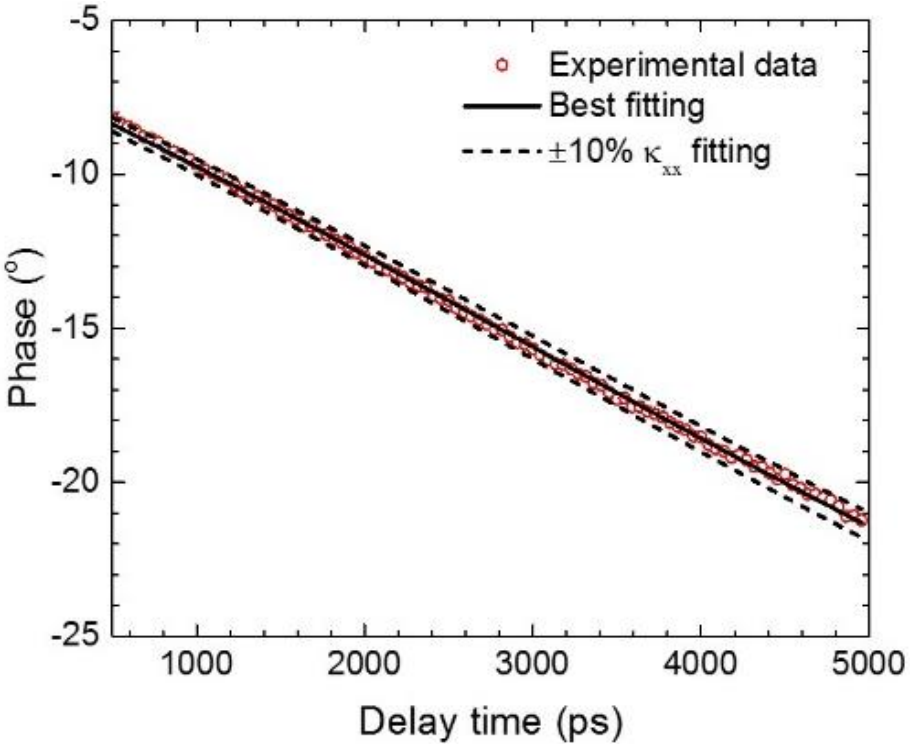

Figure 2.5 A typical AB-TDTR measurement data set (circles) for silicon, along with the best fitting curve (black line) from the thermal diffusion model. Calculated curves (dash lines) with ±10% variation of the best fitting value κ_{zz} are plotted to show the sensitivity. The modulation frequency is set as 1.1 MHz and beam size is D_x = 7 μm, D_y = 210 μm.

2.3.3 Measurement of transversely isotropic materials ($\kappa_{xx} = \kappa_{yy} \neq \kappa_{zz}$)

Next, AB-TDTR is performed on transversely isotropic material which possesses isotropic in-plane thermal conductivity but different from the cross-plane thermal conductivity. Highly oriented pyrolytic graphite (HOPG) is used as a prototype exemplary material here. Since in each layer of graphite carbon atoms are arranged at honeycomb lattice, thermal transport in basal plane is isotropic. A two-step measurement procedure is performed. First of all, the interfacial thermal conductance (G) and k_{zz} are measured using TDTR at a high *f* value and a large beam spot to ensure highest signal sensitivity to G. Specifically, here by using modulation frequency of 9.8 MHz and big circular spot with diameter of 30 μm, the interface conductance between graphite and aluminum is measured as 5.5×10^7 W/m^{2}K, which is consistent with the reported value at room temperature by Schmidt *et al*[91]. Next, AB-TDTR is applied with a low *f* value for in-plane measurement. Specifically, the modulation frequency is set as f = 1.1 MHz and beam spot size are D_x = 30 μm and D_y = 900 μm. Consequently, with the value of G fixed, κ_{xx} and κ_{zz} were extracted simultaneously by fitting the AB-TDTR measurement data (Figure 2.6 (a)). In addition, the angle dependent thermal conductivity of graphite is measured using AB-TDTR method by rotating sample around the laser incidence direction (Figure 2.6 (b)). κ_{xx} and κ_{zz} of graphite are measured as 2054.0±313.9 W/mK and 5.5±0.7 W/mK respectively with no angle dependence, consistent with literature data[81,82,84,92].

In addition to the highly anisotropic graphite, AB-TDTR is applied to measure weakly anisotropic materials with relatively low thermal conductivity such as quartz and sapphire are also used as examples. For quartz, because of the absolute value of thermal conductivity is less than 10 W/mK, smaller spot size D_x = 3 μm is adopted to improve sensitivity to in-plane thermal conductivity. The AB-TDTR results on these relatively low thermal conductivity materials show

consistency with literature (Figure. 2.8), proving the applicability of our new metrology on relatively low thermal conductivity materials with small anisotropy[83,93]. In addition, we note that a modulation frequency (f) dependent κ_{zz} was observed in transition metal chalcogenides[94]. To consider such an effect from modulation frequency dependence, κ_{zz} will be simultaneously fitted with κ_{xx} from the AB-TDTR data.

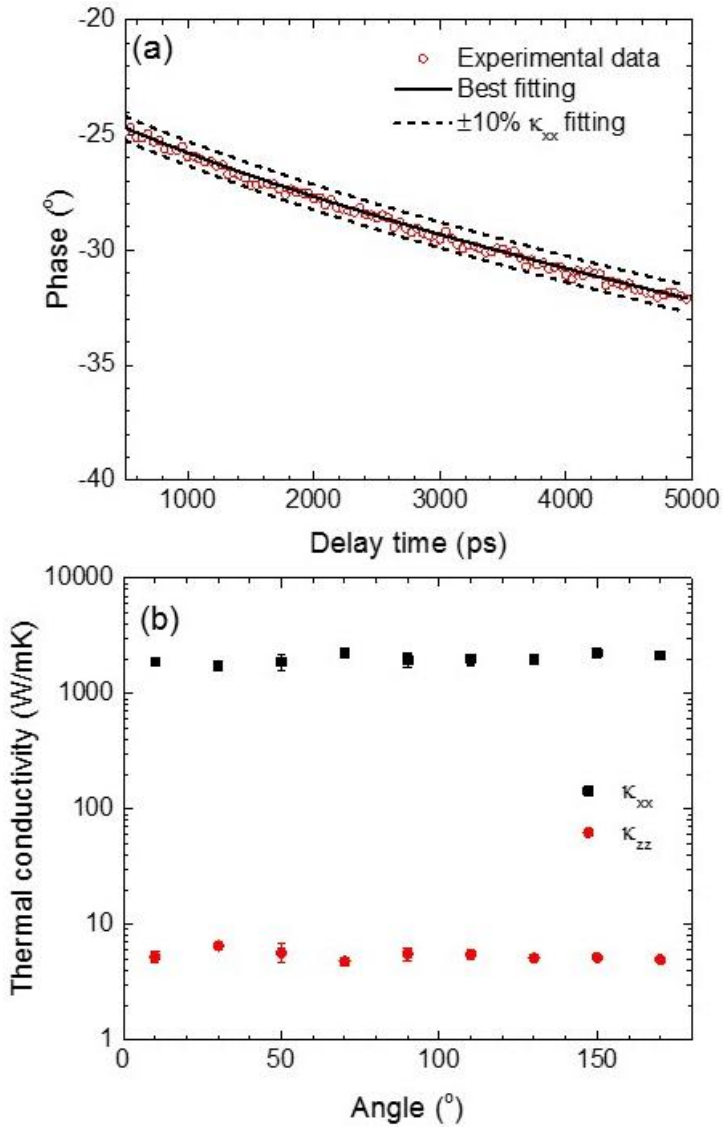

Figure 2.6 AB-TDTR measurement of angle-dependent thermal conductivity of graphite. (a) A typical AB-TDTR phase data set for graphite, along with the best fitting curve and ±10% κ_{zz} fitting curves. The modulation frequency is set as 1.1 MHz and beam size is D_x = 30 μm, D_y = 900 μm. (b) Angle dependence of in-plane and cross-plane thermal conductivity of graphite.

2.3.4 Measurement of transversely-anisotropic materials ($\kappa_{xx} \neq \kappa_{yy} \neq \kappa_{zz}$)

As we mentioned in the previous section, the most important advantage of AB-TDTR over variable spot size approach[84] is the extended capability of measuring transversely anisotropic materials, in which the thermal conductivity show significant difference even in the transverse plane. Black phosphorus (BPh) is an ideal material platform that shows strong three-dimensional isotropy due to its highly anisotropic lattice structure.

Here, we performed AB-TDTR measured and studied the angle dependent thermal conductivity of BPh. The G between BPh and aluminum is measured as 3.3×10^7 W/m^{2}K by using a modulation frequency f= 9.8 MHz and circular beam spot diameter of 30 μm. Measurement sensitivity analysis is simulated in Figure 2.7 (a) and shows that the phase signal has sufficient measurement sensitivity to the thermal conductivity along zigzag or armchair direction when it is aligned with the major elliptical direction. AB-TDTR data of BPh are displayed in Figure. 2.7 (b). Thermal conductivity are measured as 84.4±1.0 and 24.1±1.8 W/mK for zigzag and armchair direction respectively, in good agreement with the literature values[37,38,95,96].

Importantly, AB-TDTR measurement can clearly identify the diagonal elements in the thermal conductivity tensor, i.e., κ_{xx}, κ_{yy}, and κ_{zz}. As a contrast, previous methods such as beam-offset TDTR measure a mixed contribution from diagonal and off-diagonal elements (κ_{xy}, κ_{yz}, and κ_{zx}). Mathematically, the off-diagonal elements of thermal conductivity tensor as described by the anisotropic heat conduction equation[46,97]

$$\kappa_{xx}\frac{\partial^2 T}{\partial x^2}+\kappa_{yy}\frac{\partial^2 T}{\partial y^2}+\kappa_{zz}\frac{\partial^2 T}{\partial z^2}+2\kappa_{xy}\frac{\partial^2 T}{\partial x\partial y}+2\kappa_{xz}\frac{\partial^2 T}{\partial x\partial z}+2\kappa_{yz}\frac{\partial^2 T}{\partial y\partial z}=C_v\frac{\partial T}{\partial t} \quad (2\text{-}10)$$

In AB-TDTR measurement, the temperature gradient (i.e., $2\kappa_{xy}\frac{\partial^2 T}{\partial x\partial y}$) along major direction is vanishing, under a large elliptical ratio of laser beams. When the incidence direction of laser beam

is normal to one principal directions, the other two off-diagonal terms would also vanish, and the heat conduction equation would become

$$\kappa_{xx}\frac{\partial^2 T}{\partial x^2}+\kappa_{yy}\frac{\partial^2 T}{\partial y^2}+\kappa_{zz}\frac{\partial^2 T}{\partial z^2}=C_v\frac{\partial T}{\partial t} \qquad (2\text{-}11).$$

Based on equation (9), we can calculate the thermal conductivity when we rotate an angle θ between zigzag direction of BPh and the minor axis direction of beam. First, we can build a new coordinate by rotating θ degree along z axis. In the new coordinate, $x'\cos\theta = x$ and $x'\sin\theta = y$, where x' is along the minor axis direction of laser beams, x along zigzag direction and y along armchair direction. The new heat conduction equation would be

$$\kappa_{xx}cos^2\theta\frac{\partial^2 T}{\partial x'^2}+\kappa_{yy}sin^2\theta\frac{\partial^2 T}{\partial x'^2}+\kappa_{zz}\frac{\partial^2 T}{\partial z^2}=C_v\frac{\partial T}{\partial t} \qquad (2\text{-}12)$$

So the thermal conductivity along x' would be

$$k_{x'x'}=k_{xx}cos^2\theta+k_{yy}sin^2\theta \qquad (2\text{-}13)$$

where κ_{xx} and κ_{yy} are thermal conductivity along zigzag and armchair direction respectively. Based on Eqn. (2-13), the angle-dependent diagonal elements of thermal conductivity tensor is predicted (Figure. 2.7 (c)). Experimentally measured thermal conductivity using AB-TDTR as a function of angle is plotted together and shows great agreement with the model prediction (Figure. 2.7 (c)). This suggests that our AB-TDTR measurement is a direct representation of the diagonal elements.

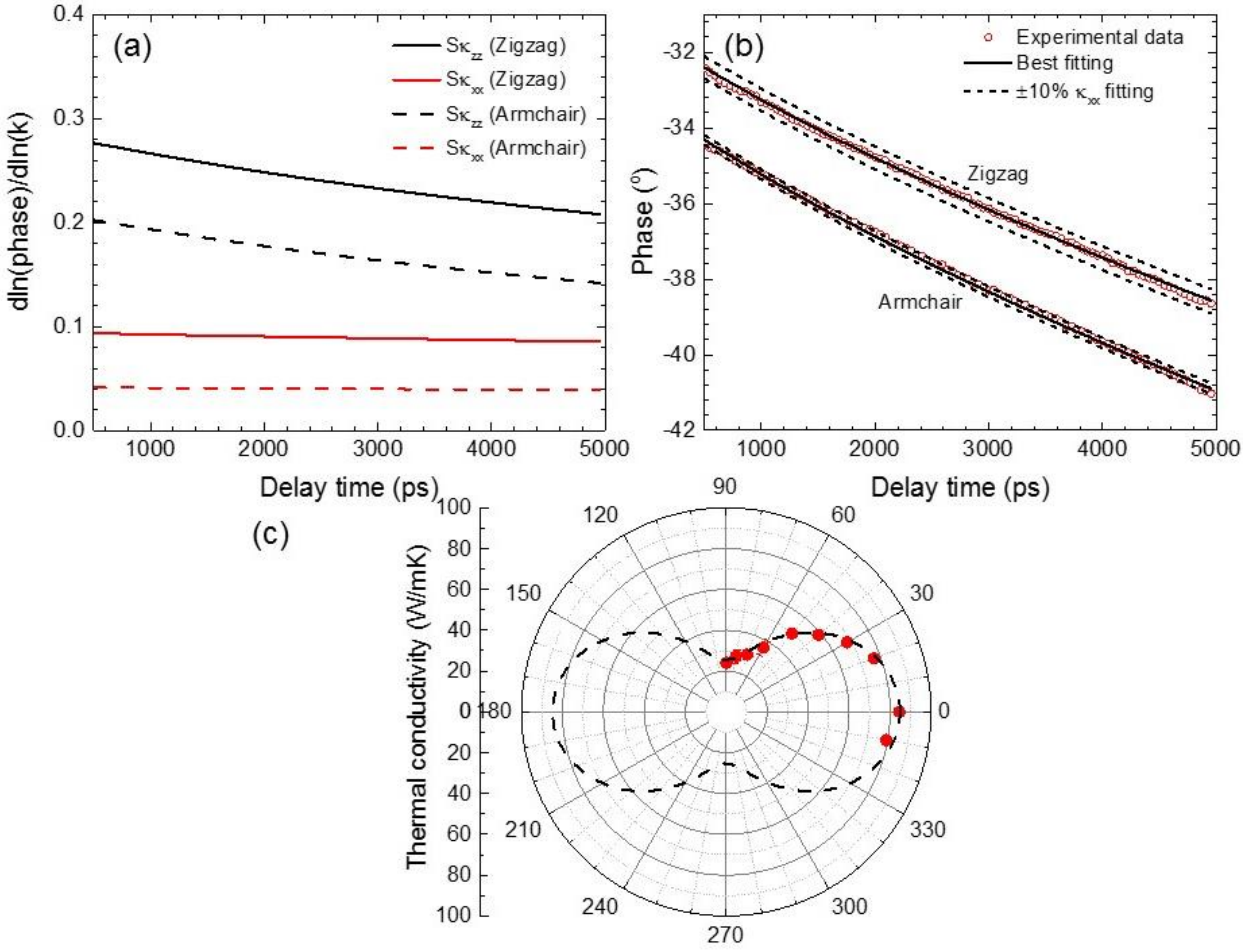

Figure 2.7 AB-TDTR measurement of anisotropic thermal conductivity of black phosphorus with angel dependence. (a) Sensitivity analysis for κ_{xx} measurement when the major direction of elliptical beam aligned with armchair or zigzag directions. The modulation frequency is 1.1 MHz and spot size is D_x = 10 μm, D_y = 300 μm. (b) Two typical AB-TDTR phase data sets for in-plane thermal conductivity measurement along armchair and zigzag directions. (c) Angle dependent thermal conductivity of BPh. The dash line is the theoretical prediction of thermal conductivity based on thermal conductivity of zigzag direction and armchair direction.

2.4 Uncertainty Analysis

The uncertainty analysis of thermal conductivity measurement using AB-TDTR is performed here using the exemplary samples, i.e. silicon, graphite, black phosphorus, by following the procedure of Malen et al.[69]. The uncertainty of κ_{xx} comes mainly from the uncertainty of κ_{zz}, interfacial

thermal conductance G, spot size D_x, metal thickness d_m and volumetric heat capacity of the samples C_v. Mathematically, the uncertainty of κ_{xx} can be calculated from the uncertainty using

$$\Delta\kappa_{xx} = \sqrt{\sum_j (\Delta\kappa_{xx,j})^2}$$

$$j = \kappa_{zz}, G, D_x, d_m, C_v \quad (2\text{-}14)$$

where $\Delta\kappa_{xx}$ is the uncertainty of κ_{xx} measurement and $\Delta\kappa_{xx,j}$ the uncertainty of κ_{xx} contributed by the factor j. $\Delta\kappa_{xx}$ of our exemplary materials along with the uncertainty contributions from each individual factor are listed in Table 2.1. From the analysis, the $\Delta\kappa_{xx}$ measurement uncertainty is around 10 %. And most of the error comes from the uncertainty of κ_{zz} and G, which can be further reduced by using bigger beam spot size and more repetitive measurements.

Table 2.1 Uncertainty analysis of AB-TDTR in-plane thermal conductivity measurement of silicon,

graphite and black phosphorus.

.

	Silicon			Graphite			Black phosphorus X along zigzag direction		
j	value	Δj	$\Delta\kappa_{xx,j}$	value	Δj	$\Delta\kappa_{xx,j}$	value	Δj	$\Delta\kappa_{xx,j}$
d_m (nm)	80.0	±1.0	±0.2	80.0	±1.0	±40.2	80.0	±1.0	±2.4
D_x (μm)	7.0	±0.1	±3.8	30.0	±0.3	±41.1	10.0	±0.1	±2.5
κ_{zz} (W/mK)	138.2	±5.1	±4.8	5.5	±0.7	±242.4	4.2	±0.2	±6.5
G (MW/ m^2K)	86	±4.3	±11.4	55	±2.8	±50.6	3.3	±0.2	±5.0
C_v (MJ/m^3K)	1.65	±0.1	±0.3	1.59	±0.1	±4.6	1.59	±0.1	±3.1
total	144.2		±12.9	2054.0		±254.3	84.4		±9.4

2.5 Conclusion

In summary, AB-TDTR measurements are conducted for different materials with wide range of thermal conductivity values from ~5 W/mK to 2000 W/mK and thermal conductivity anisotropy from 0.5 to 400. The measurement results are plotted in Figure. 2.8 in good agreement with the literature. This study proves that AB-TDTR method as a new metrology to precisely measure anisotropic thermal transport properties. This development enable a powerful platform to understand thermal transport mechanism in anisotropic materials.

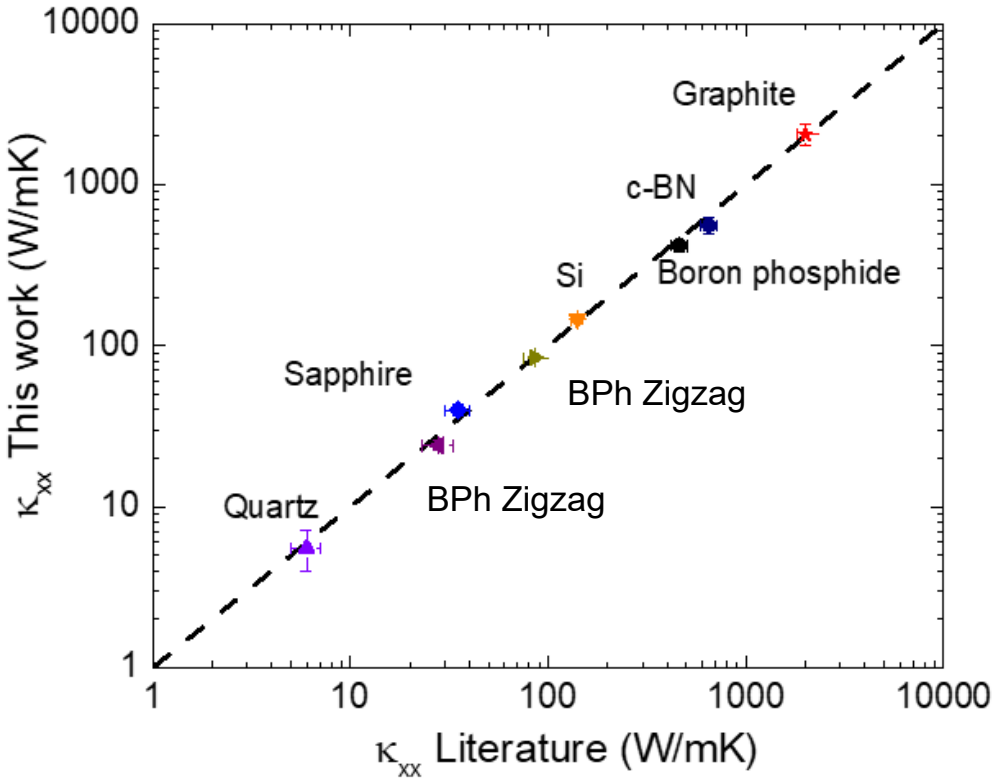

Figure 2.8 Summary of example measurement data from AB-TDTR versus literature reported values.

CHAPER 3

Anisotropic Thermal Boundary Resistance Across Black Phosphorous

3.1 Introduction

With the continuous miniaturization of modern electronic devices, power density increases dramatically in nanoscale chips and heat dissipation becomes a key technological challenge for the semiconductor industry[1–12]. Intensive efforts have been devoted to thermal management including the recent development of new semiconductor materials with ultrahigh thermal conductivity, such as cubic boron phosphide (~500 W/mK)[53] and boron arsenide (~ 1300 W/mK)[102,106,107]. In parallel to heat transfer in homogenous materials, heat dissipation in high power devices can also be severely limited by the near-junction thermal resistance across heterogeneous interfaces, *i.e.*, the thermal boundary resistance (TBR)[55,98,105,108,109]. On the other hand, thermal isolation applications, such as jet engine turbines require interfaces with large TBR and high temperature stability[110]. Therefore, controlling TBR at the interfaces between different materials is of primary significance. However, the current understanding of TBR remains elusive and is far below that of heat transfer in homogenous materials. Fundamentally, TBR measures an interface's resistance to thermal flow and results from the scattering of energy carriers, due to the difference in vibrational and electronic band structures from both sides of the interface. The earliest discovery of TBR can be traced back to 1941 and the Kapitza resistance between liquid and solid

helium[111]. Thereafter, TBR was confirmed to exist at all heterogenous interfaces regardless of the atomic perfection[112]. Despite decades of efforts, understanding and improving TBR still remains challenging. Most studies are usually limited to idealized interfaces or isotropic considerations, and a synergy between TBR and materials structures has not been well established[24].

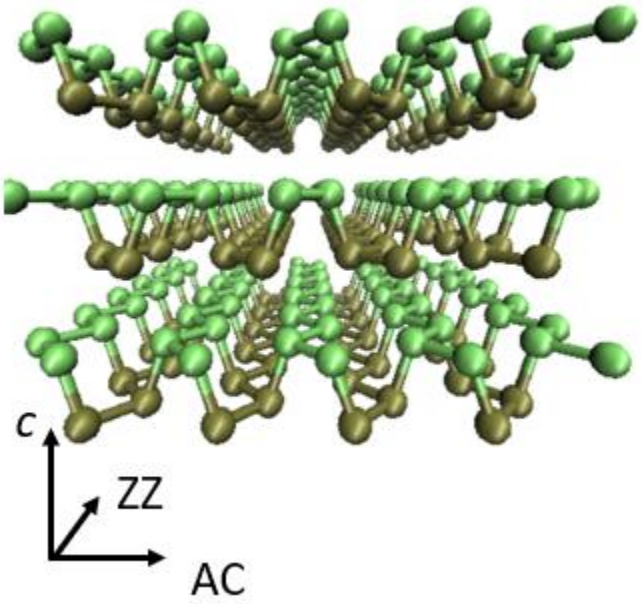

Figure 3.1 Schematic of the crystal structure of BPh.

In the meantime, two-dimensional (2D) van der Waals materials and their heterostructures are under intense exploration as building blocks for nanoelectronics, making studying heat dissipation across their interfaces of high interest[113–118]. Moreover, 2D materials are the ideal platform for exploring the structural relationship with TBR because of their highly orientation-dependent phonon band structures. In particular, black phosphorus (BPh) has a highly anisotropic puckered orthorhombic crystal structure[118–120]. As illustrated in Figure 3.1, each P atom forms three covalent bonds from the 3p orbitals. Inside each 2D lattice layer, there are two types of phosphorus bonds: the longer bond connects P atoms in the top and bottom planes, and the shorter

bond connects the nearest P atoms in the same plane. The interlayer interaction is based on van der Waals forces. So there are three characteristic directions in BPh defined as armchair (AC), zigzag (ZZ) and cross-plane (CP) directions (Figure 3.1) which lead to their respective thermal conductivity of 85.80, 27.58, and 3.86 W/mK[37–42,96]. *In situ* measurements, conducted with ionic intercalations has also revealed anisotropic defect scattering on the phonon transport[37]. Therefore, BPh can serve as a powerful platform to explore the mechanisms for the formation of TBR and its crystal structural relationship. As illustrated in Fig 1b, TBR is generally understood as resulting from the breakdown of coherence of energy carriers' transport across the interface. When the incident phonons encounter the interface, some of them transmit through the interface, while the remainders are reflected by the interface. The sudden impedance to the phonon transport leads to discontinuous equilibrium distribution of phonons at the interface, *i.e.,* a sharp temperature drop (ΔT, Figure 3.2). At steady state, the total heat flux (Q) near the interface regime on both sides should match with each other. Therefore, as the heat flux is mainly carried by the phonons, the anisotropy of the phonon band structures of BPh may result in different spectral phonon fluxes along different directions. However, on the metal side, the nearly isotropic structure will result in the same spectral heat flux regardless of the orientation. In the meanwhile, to conserve the energy flow across the interface, the spectral phonon transmissivity needs to be orientation dependent. Therefore, studying such interfacial energy transport across directional 2D lattice could be strongly affected by the intrinsic anisotropic phonon spectra and provide direct TBR-structure relationships but remains unexplored so far[24].

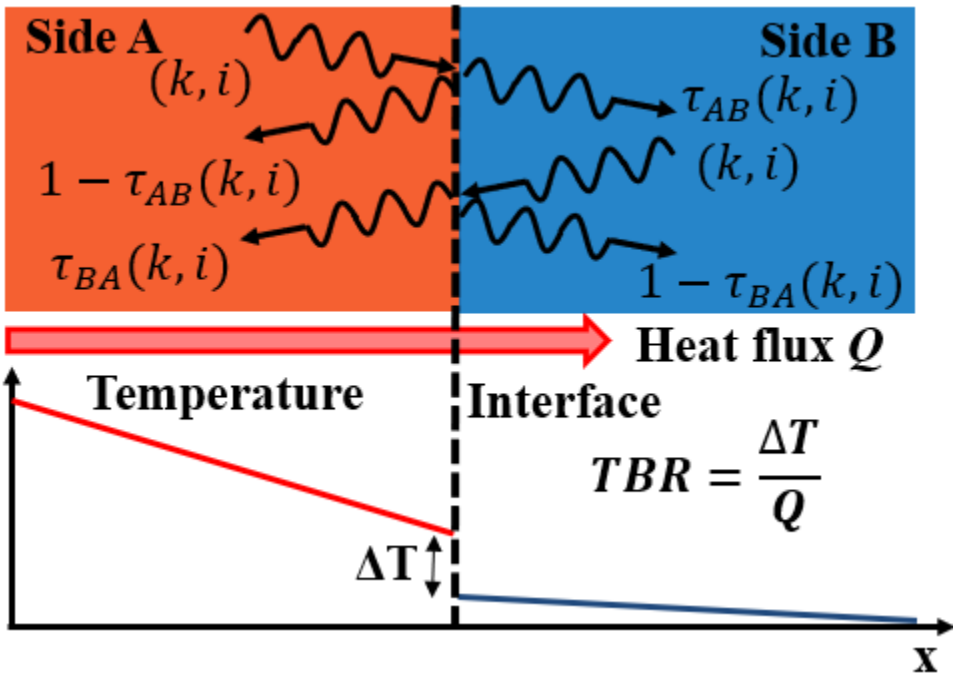

Figure 3.2 Schematic of thermal transport and temperature profile across a materials interface. τ_{AB} represents the mode-specific transmission of phonons from Material A to Material B. (k, i) represent the phonon wave vector and polarization respectively. An abrupt temperature drop (ΔT) at the materials interface indicate a TBR that restricts the heat flux (Q) going across the interface.

3.2 Experimental observation of anisotropic thermal boundary resistance

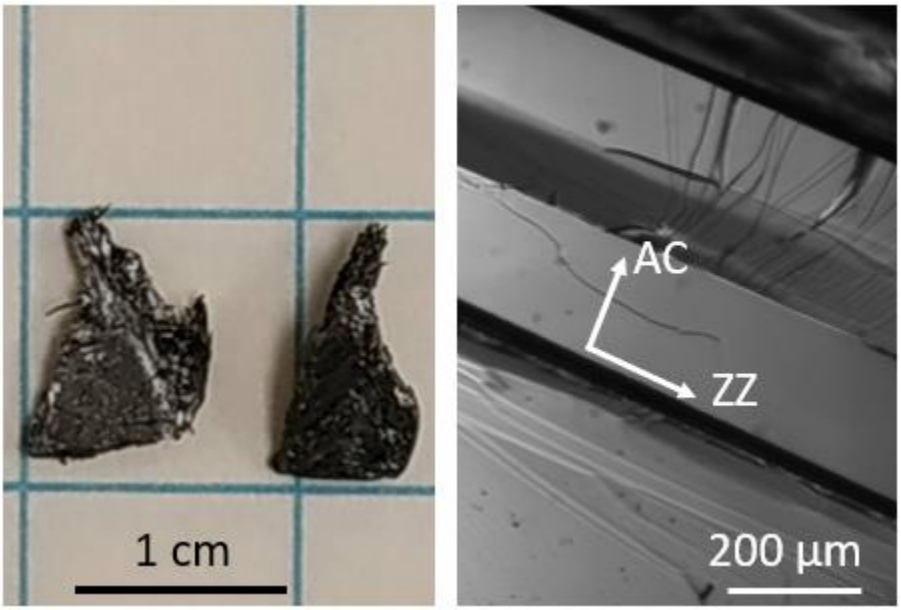

Figure 3.3 Optical images of BPh samples.

Here we report the first investigation on the crystal-orientation dependent thermal transport across metal-BPh interfaces and observe highly anisotropic TBRs stemmed from its intrinsic structures. High-quality BPh crystals were synthesized using the chemical vapor deposition method. Red phosphorus was used for starting material and SnI_4 and Sn as a mineralizer. 400 mg of red phosphorus with 20 mg of Sn and 10 mg of SnI_4 were grinded by using pestle and mortar. A quartz tube was pre-heated at 473 K under vacuum to remove possible moisture. After the red phosphorus, SnI_4, and Sn mixture was loaded, the quartz tube was evacuated and flame-sealed under high vacuum. The tube was then placed into the two-zone tube furnace, with temperature of 923K and 897K for hot zone and cold zone respectively. Furnace temperature was slowly heated from room temperature to reaction temperature for 4 hours and held for 24 hours and slowly cooled down to room temperature. We are able to obtain centimeter-size high-quality BPh as shown in Figure 3.3, indicating a clean surface after exfoliation. To prepare interfaces with different

orientations, the crystalline directions of BPh were identified first by angle-resolved, polarized Raman spectroscopy. When the incident laser beam was parallel to the cross-plane direction of BPh, three Raman peaks were observed: A_g^1 (~363 cm^{-1}), B_g^2 (~440 cm^{-1}) and A_g^2 (~467 cm^{-1})[37,121–123] (Figure. 3.4 (a)). The fact that the relative intensity of the three Raman peaks depends on the alignment of the angles between the polarization of the excitation laser and the crystal orientations is noteworthy. For example, the A_g^1, A_g^2 peaks are maximized when the polarization is along the AC direction, whereas B_g^2 achieves the highest intensity when the laser polarization forms a 45^o angle with the AC direction. Therefore, the angle dependent intensity of the three Raman peaks, plotted in Fig. 3.4 (b), were used to determine the crystal orientations. The BPh samples were cleaved along different orientations in parallel to ZZ, AC and CP directions, respectively. A thin layer of aluminum (Al) around 100 nm was deposited on the samples via e-beam evaporation to form a clean metal-semiconductor interface (Fig. 3.5). The crystal orientations of BPh were also verified by the AB-TDTR measurement of anisotropic thermal conductivity and show consistency with recent studies. Note that for all the thermal measurement in this work, the samples are kept in cryostat (Janis, ST-100H) under a high vacuum ~ 10^{-4} torr to avoid oxidation. We conducted Energy Dispersive X-ray Spectroscopy (EDS) at the cross-section interface of Al-BPh samples (Figure 3.6). Only Al and P peaks are detected and there is no observation of any impurity. The escape peak (P Si-ESC) at ~ 0.3 keV is generated from the EDS silicon detector crystal.

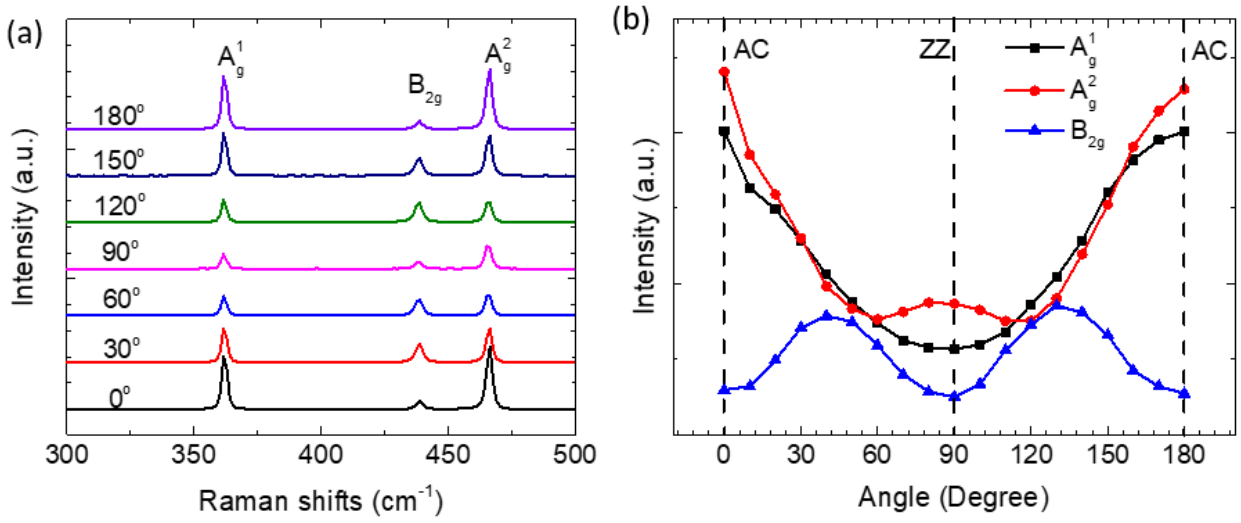

Figure 3.4 (a) Angle-dependent Raman spectroscopy of BPh. (b)The intensity plot of three Raman peaks with measurement angle dependence and used to determine the crystal orientations of BPh.

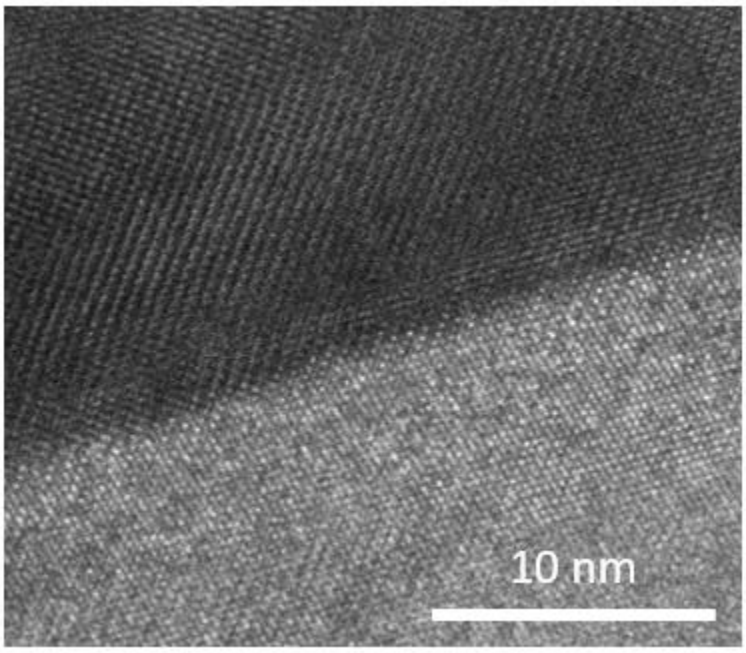

Figure 3.5 High-resolution transmission electron microscopy image of the interface between aluminum and black phosphorus**.**

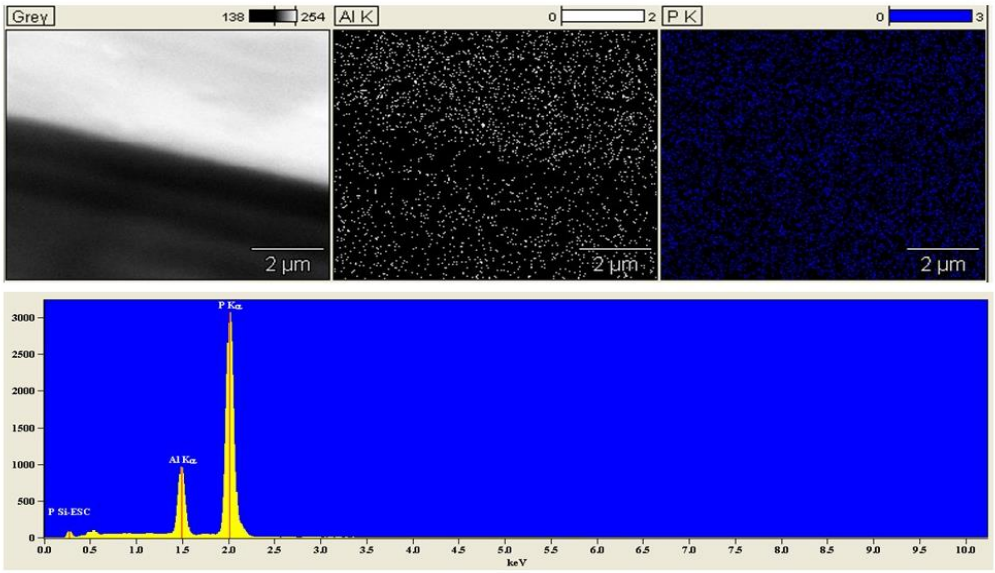

Figure 3.6 Energy dispersive x-ray spectroscopy (EDS) analysis near the Al-BPh interface**.**

TBR of metal-semiconductor interfaces along different crystal orientations of BPh was characterized using a time-domain thermoreflectance (TDTR) technique, illustrated in Figure 3.7 (a). TDTR is an ultrafast technique that has been widely applied for measuring thermal properties and TBRs of different materials[8,53,80,81,102,124,125] and has been used to develop novel experimental spectroscopy techniques to study phonon spectra[14,53,126]. In our setup, a femtosecond laser pulse is split into a pump beam and a probe beam. The pump beam, at the wavelength of 400 nm, thermally excites the sample surface, and the probe beam, at the wavelength of 800 nm, detects the sample temperature. The delay time between pump and probe beams can be precisely controlled by a mechanical delay stage with a sub-picosecond resolution. The transient TDTR signal is detected and fitted to a multilayer thermal model to extract TBR. The typical experimental data from our TDTR measurements and fittings[80], based on the phase signals for ZZ, AC, and CP directions, are shown in Figure 3.7 (b). Surprisingly, a significantly high ratio of anisotropic TBRs for BPh-Al

interfaces were measured for different BPh crystal orientations. TBR in the cross-plane direction (TBR_{CP}) is 1.62×10^{-8} m^2K/W, 2.41 times of that in the AC direction (6.71×10^{-9} m^2K/W) and 3.27 times of that in the ZZ direction (4.95×10^{-9} m^2K/W). To further investigate the phonon transport mechanism at the BPh-Al interface, we also measured the temperature dependent TBR in each direction from 80 K to 300 K. The anisotropy of TBR along different orientations remains remarkable for the full temperature range. Such a high ratio of anisotropic TBR has not been observed in other materials interfaces[24]. We attribute the observed substantial TBR anisotropy to the highly anisotropic crystal structures thus the anisotropic phonon band structures of BPh, and combine theory and experiment to perform detailed analysis in the following.

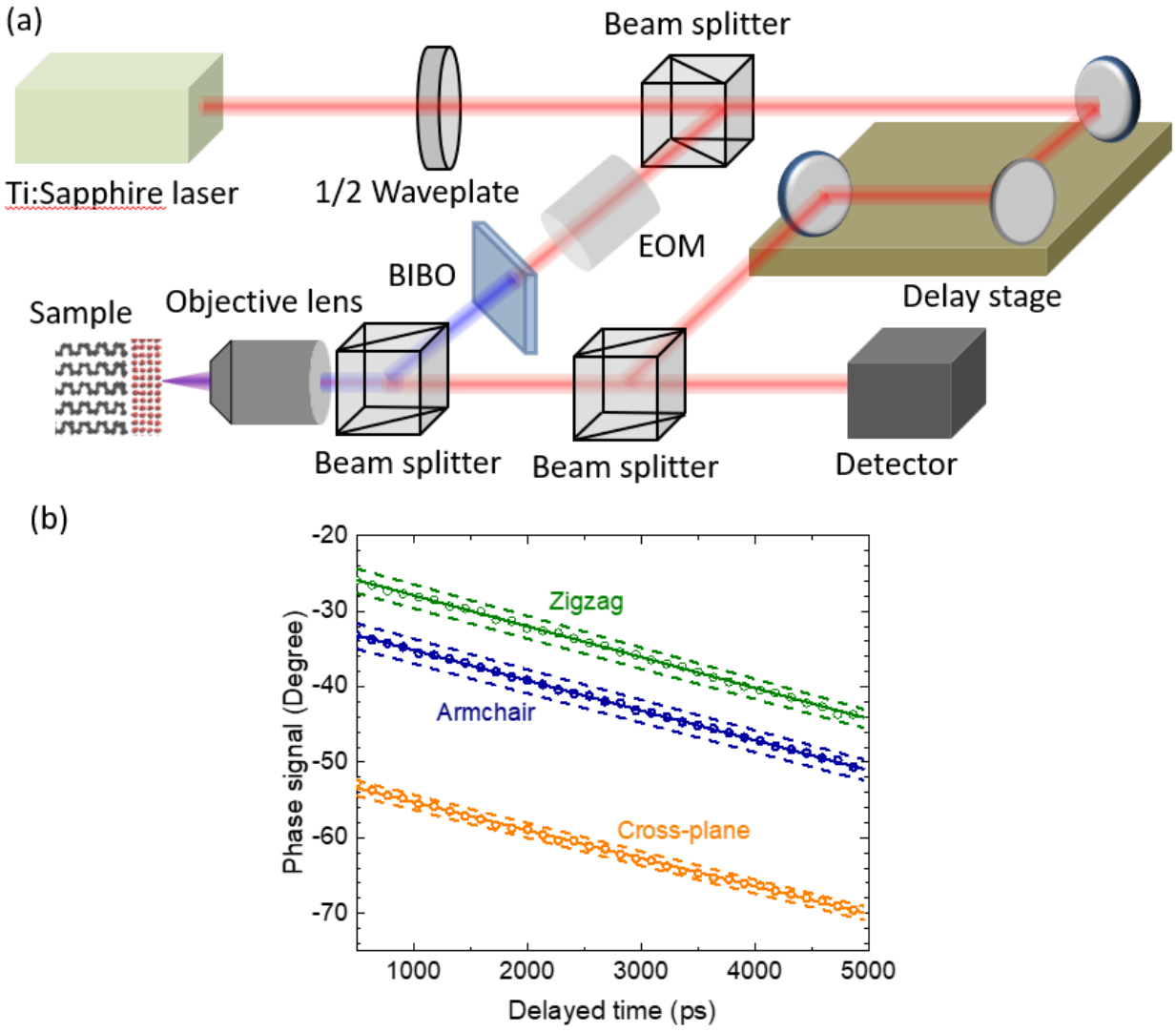

Figure 3.7 Experimental setup of the ultrafast pump-probe spectroscopy and the measurements of anisotropic TBR. (a) Schematic of the time-domain thermoreflectance (TDTR) method. Blue and red color represents the pump and probe beam, respectively. (b) Experimental data (circles) and the fits from the multilayer thermal transport model (solid lines) for the TDTR phase signal. Calculated curves (dashed lines) using the TBR varied by ±10% of best values are plotted to illustrate the measurement sensitivity.

3.3 Fundamental understanding of anisotropic TBR from ab initio calculations

and molecular dynamics simulations

To quantitatively analyze the crystal orientation and temperature dependent anisotropic TBR, we performed *ab-initio* calculations to capture phonon spectral contributions. From the phonon picture[127], TBR can be understood as phonon reflection by interface. By integrating all the energy carried by the transmitted phonons, TBR or its reciprocal value, i.e. thermal boundary conductance (G), can be calculated as:

$$\frac{1}{TBR} = G = \frac{1}{2(2\pi)^3}\sum_i \int_{\boldsymbol{k}} \tau_{AB}(\boldsymbol{k},i)\hbar\omega(\boldsymbol{k},i)|\boldsymbol{v}(\boldsymbol{k},i)\boldsymbol{n}|\frac{df}{dT}d\boldsymbol{k} \qquad (3\text{-}1)$$

where $\tau_{AB}(\boldsymbol{k},i)$, $\omega(\boldsymbol{k},i)$, $\boldsymbol{v}(\boldsymbol{k},i)$, $f = \frac{1}{\exp\left(\frac{\hbar\omega(\boldsymbol{k},i)}{k_B T}\right)-1}$ are the mode-dependent transmission coefficient, phonon frequency, group velocity and equilibrium Bose-Einstein distribution function corresponding to phonons with wavevector $\boldsymbol{k}$ and polarization i. $\boldsymbol{n}$ is the unit vector normal to interface. The calculation of TBR requires a detailed knowledge of the phonon dispersion relationship over the entire Brillouin zone. In literature, for simplicity, the dispersion relationship is usually approximated by a linear dispersion relationship (*i.e.*, the Debye approximation[128]). However, the Debye approximation oversimplifies the TBR calculation using a single phonon group velocity along each direction. Reddy and Majumdar[129] improved the Debye approximation by using the Born-von Karman model instead of the linear assumption in the Debye model. Dames *et al.*[130] proposed elliptical dispersion relations to account for the anisotropic phonon band structure.

Here we performed *ab-initio* calculations to obtain the full phonon dispersion relationship and construct the phonon-mode dependent modeling of the interfacial thermal transport. To obtain the full phonon dispersion relationship of BPh and Al, the second order interatomic force constants are needed for the construction of the dynamical matrix[128]. We applied the density functional

theory (DFT) calculations and finite displacement method to obtain the interatomic force constants corresponding to the equilibrium crystal structures[128,131,132]. For the DFT calculations, we used the open-source package, Quantum Espresso and XSEDE computational platform to construct a supercell with a 5×5×2 cubic unit cell for BPh and 3×3×3 cubic unit cell for Al with periodic condition and a wave pseudopotential with PBEsol functional was adopted. The kinetic-energy cut-off for the plane-wave basis set was 550 eV for Al and 960 eV for BPh. 10×10×10 and 4×4×4 Monkhorst-Pack meshes were used for the reciprocal space of Al and BPh, respectively. The interlayer van de Waals interaction was corrected by using the DFT-D functionals[133]. The lattice constants for the calculated equilibrium structure of Al and BPh were compared with the experimental values[134,135] and are in good agreements. Under the equilibrium structure, the phonon band structures can be calculated by extracting the second order force constants by displacing the atoms with a finite distance. Note that the TBR here is dominated by phonon transport across the Al-BPh interfaces[136,137] and we notice that electron-phonon coupling can show importance across some metal-dielectric interfaces[138,139]. To verify our calculation results, the calculated phonon dispersion relationships along different directions were compared to experimental data from neutron scattering experiments[140,141], showing good consistence (Figure 3.8).

Table 3.1 Lattice constants obtained from the DFT calculations and experiments**.**

Lattice constant (Å)	Aluminum	Black phosphorus
Our DFT calculation	4.013	3.294, 10.424, 4.329
Experiments	4.046	3.314, 10.478, 4.376

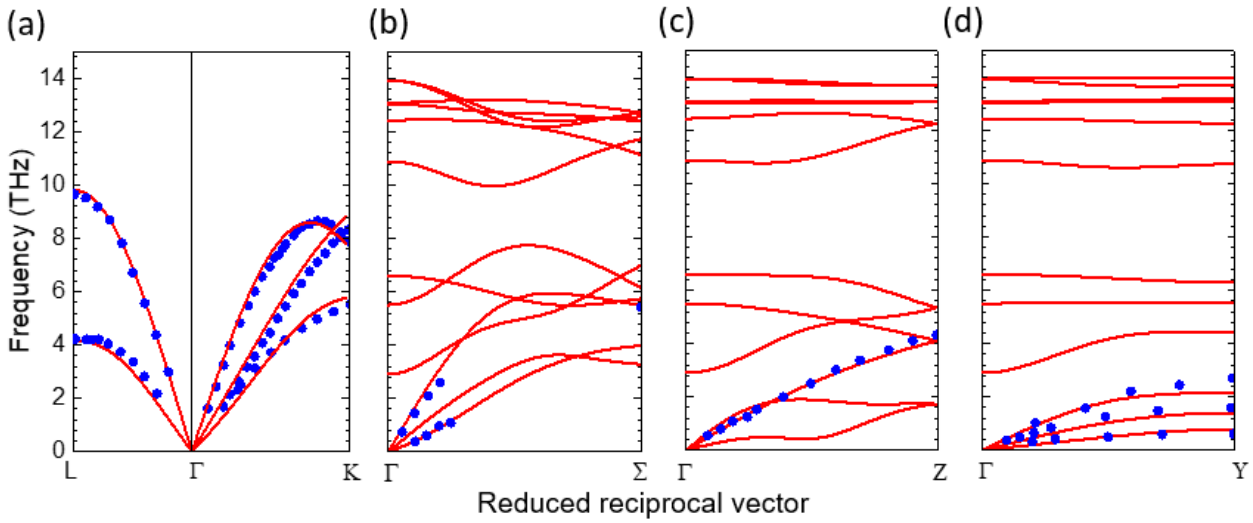

Figure 3.8 Phonon dispersion relations calculated from density functional theory (DFT) (red lines) in comparison with neutron scattering experiments (blue dots, Ref. 119, 120) for (a) Al and (c-d) BPh.

TBR is considered as how resistive it is when phonons from both sides participate in thermal transport across the interface. Here we compare the phonon band structures of BPh and Al. Al has three acoustic phonon branches with frequency up to 10 THz. By contrast, BPh has three acoustic branches from 0 to ~6 THz, nine optical branches, three of which are from ~2 to 8 THz, and the other six above 10 THz. Considering energy conservation during the interface transport and the low probability of scattering events involving multiple phonons, since there is no energy state with comparably high frequency available in Al, the high-frequency phonons inside BPh make negligible contributions to the interfacial phonon transport. The highest cutoff frequencies of acoustic phonons along ZZ, AC and CP direction will be determined by that of BPh,

i.e. 5.6 THz, 4.1 THz and 2 THz, respectively. The CP direction has the largest mismatch of highest cutoff frequencies between the two materials, AC direction the second, and ZZ direction the smallest, which qualitatively explains the formation of anisotropic TBRs. In addition, we also noticed that the variations in the phonon travelling velocity distributions along different directions (Figure 3.9 (a)) can further amplify the anisotropic TBRs: phonon velocity along the ZZ direction has a distribution for higher values than those along the AC and CP directions.

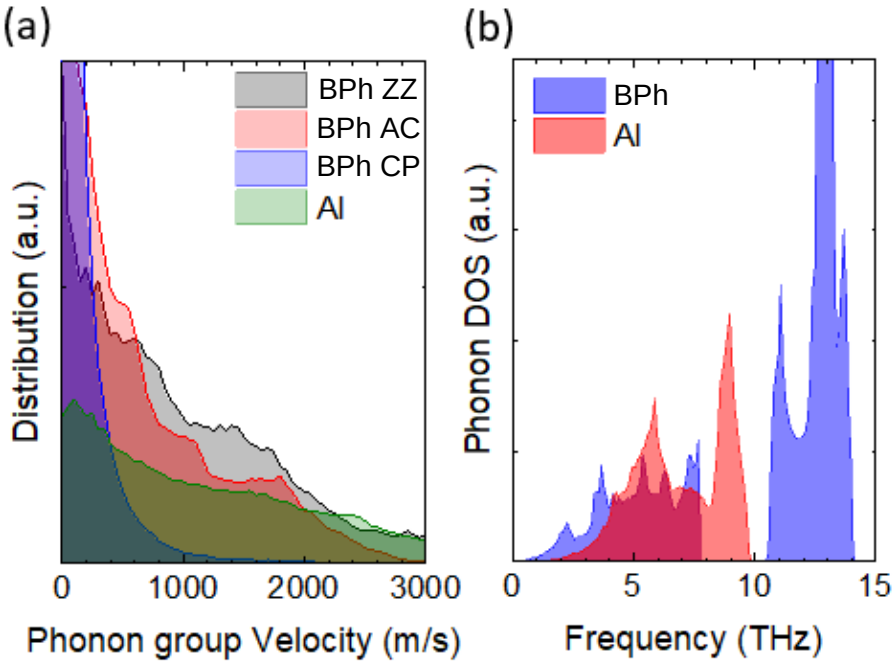

Figure 3.9 (a) Phonon spectral distribution of group velocity in the first Brillouin zone along different crystal directions. (b) Phonon spectral distribution of density of states (DOS).

More quantitatively, the TBRs along different directions are carefully calculated in the following. From the detailed balance, at equilibrium and under elastic scattering assumption, the heat flux carried by phonons with a certainty frequency ω_0 from side A to side B is equal to that from side B to side A[142]:

$$\sum_i \int_{\boldsymbol{k}} \tau_{AB}(\boldsymbol{k},i)\hbar\omega(\boldsymbol{k},i)|\boldsymbol{v}(\boldsymbol{k},i)\boldsymbol{n}|f\delta_{\omega_0,\omega(\boldsymbol{k},j)}d\boldsymbol{k} =$$

$$\sum_j \int_{\boldsymbol{k}} \tau_{BA}(\boldsymbol{k},j)\hbar\omega(\boldsymbol{k},i)|\boldsymbol{v}(\boldsymbol{k},j)\boldsymbol{n}|f\delta_{\omega_0,\omega(\boldsymbol{k},j)}d\boldsymbol{k} \qquad (3\text{-}2)$$

$$\tau_{AB}(\boldsymbol{k},i) = 1 - \tau_{BA}(\boldsymbol{k},i) \qquad (3\text{-}3)$$

Thus, the transmission coefficient can be calculated as follows:

$$\tau_{AB}(\boldsymbol{k},i) = \frac{\sum_i \int_{\boldsymbol{k}}^{SideB} |\boldsymbol{v}(\boldsymbol{k},j)\boldsymbol{n}|\delta_{\omega_0,\omega(\boldsymbol{k},j)}d\boldsymbol{k}}{\sum_i \int_{\boldsymbol{k}}^{SideA} |\boldsymbol{v}(\boldsymbol{k},i)\boldsymbol{n}|\delta_{\omega_0,\omega(\boldsymbol{k},i)}d\boldsymbol{k} + \sum_j \int_{\boldsymbol{k}}^{SideB} |\boldsymbol{v}(\boldsymbol{k},j)\boldsymbol{n}|\delta_{\omega_0,\omega(\boldsymbol{k},j)}d\boldsymbol{k}} \qquad (3\text{-}4)$$

where $\delta_{\omega_0,\omega(\boldsymbol{k},i)}$ is the Kronecker delta function. $\tau_{AB}(\boldsymbol{k},i)$ is a key parameter to quantify TBR, but remains challenging for state-of-the-art phonon theories. Note that one implicit assumption in most literature modeling is that all the phonons lose their memory of their polarization after diffusely scattered at the interface. However, phonons may not be able to hop across different branches freely. The determination of the probability of the phonons to jump between different branches is non-trivial. Although some recent work based on atomic Green's function investigated the modelling of the phonon mode conversion[143,144], these study are limited to ideal interfaces with atomic-level perfection. Therefore, we performed calculations for both extreme cases, *i.e.*, free branch conversion (FBC) and no branch conversion (NBC) based on diffuse mismatch model (DMM). In FBC-DMM, the phonons flux balance is calculated without specified to a certain polarization. In NBC-DMM, the transmission coefficient was calculated for longitudinal acoustic (LA) branches and transversely acoustic (TA) branches separately by using Eqn. (3-4).

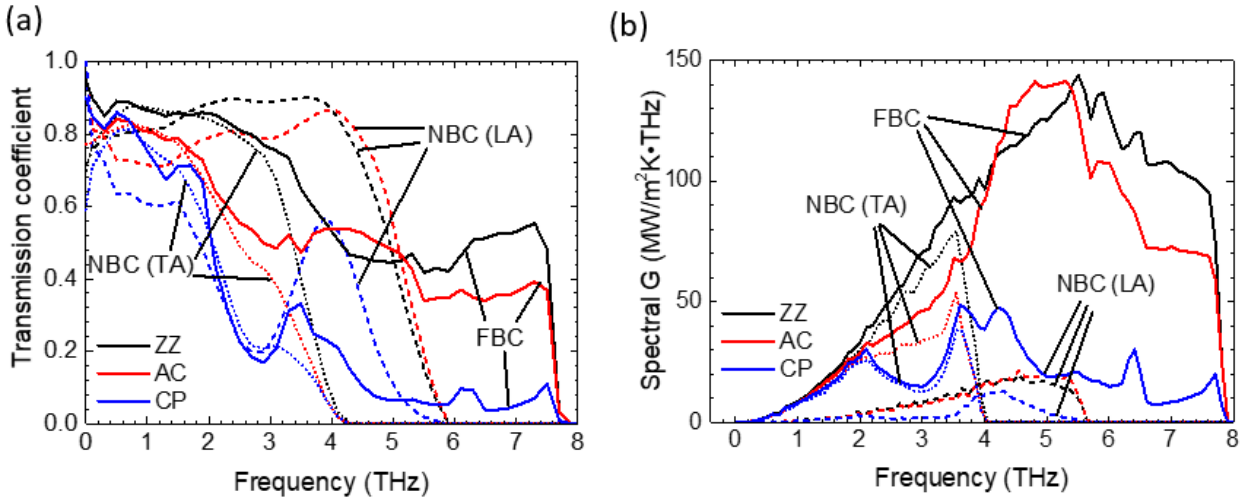

Figure 3.10 (a) Phonon mode dependent transmission coefficients at the Al-BPh interface calculated from the free branch conversion (FBC) and no branch conversion (NBC) diffuse mismatch models. (b) Spectral G as a function of phonon frequency calculated from FBC and NBC.

To analyze the phonon spectral transport at the interface, the phonon spectral interface transmission coefficients (τ_{AB}) for different orientations were calculated based on FBC-DMM and NBC-DMM and shown in Fig. 3.10 (a). The FBC-DMM transmission coefficients show a frequency with a nearly monotonically decreasing trend followed by a sharp drop to zero at 7.9 MHz. The sudden drop of transmissivities can be explained by the phonon density of states (PDOS) of Al and BP (Figure 3.9 (b)). The phonons with frequencies from 7.9 MHz to 9.8 MHz allowed on the Al side are not allowed on the BPh side, leading to no open channels for these phonons at the interface. Figure 3.9 (b) also shows that the PDOS ratio of BPh and Al is higher than 1 before ~ 4 THz, and decreases from 4 THz to 6 THz, thus following the same trend as the transmission coefficients. In addition, the reduced phonon group velocity near the Brillouin zone edge is also responsible for the decreasing transmission coefficients. In the NBC-DMM, the transmission coefficients can be decomposed into contributions from LA and TA phonons. The transmission

coefficients become zero when frequencies of LA phonons and TA phonons reach to their highest values.

The TBRs are calculated based on both FBC-DMM and NBC-DMM. These two models lead to different interface spectral transmissivities (Figure. 3.10 (a)) and thus different phonon spectral contribution to TBR. The spectral interface thermal conductance G (i.e. 1/TBR) for the Al-BPh interface is decomposed into relative contributions from different phonon modes and displayed in Figure. 3.10 (b). For almost the full frequency range, G along the cross-plane direction is lowest regardless of the model used, because of the smallest phonon energy and group velocity in the cross-plane direction. Despite the different absolute magnitudes, the most significant difference in spectral G between these two models lies in the contribution from high energy phonons (e.g., frequency > 4 THz, which is the cutoff frequency of TA phonons in BPh). According to the FBC-DMM prediction, the optical phonons with frequencies between 2.1 to 7.8 THz dominate the interfacial thermal transport, whereas the NBC-DMM ignores the contribution from optical phonons. In the FBC-DMM, peaks are around 4-6 THz, where both the optical phonons and LA phonons exist with relatively high group velocity. The maximum frequency of phonons contributing to G in the NBC-DMM are around 5.6 THz, up to which phonons are allowed on three acoustic bands.

Furthermore, this distinct phonon spectral contribution to interface thermal transport can be observed from its temperature dependence because the excitation of higher energy phonons is more temperature dependent. We calculated temperature-dependent G from 50 to 300 K using both FBC-DMM and NBC-DMM in Figure 3.11. We have also plotted our experimentally measured temperature-dependent G in the same figure for comparison. First, it is clear that the NBC-DMM prediction has a better agreement with the experimental measurement in terms of the magnitude

of TBR. On the other hand, it is interesting to notice that the FBC-DMM predicts a stronger temperature effect (i.e. a higher slope of temperature dependent G) than NBC-DMM, indicating that optical phonons partially participate in the interfacial thermal transport. To involve the optical phonons transport at interface, it requires the mode conversion from acoustic phonons in Al to optical phonons in BPh. The probability for phonon mode conversion across different branches is important for phonon theory but difficult to be determined. Recently, atomic Green's function (AGF) was combined with DFT calculations to treat the mode conversion[145,146], but it is challenging to include anharmonic effects into AGF. Molecular dynamics simulation, on the other hand, can be an alternative tool to study interfacial thermal transport by implicitly considering the phonon mode conversion and full order anharmonic effects[24,147].

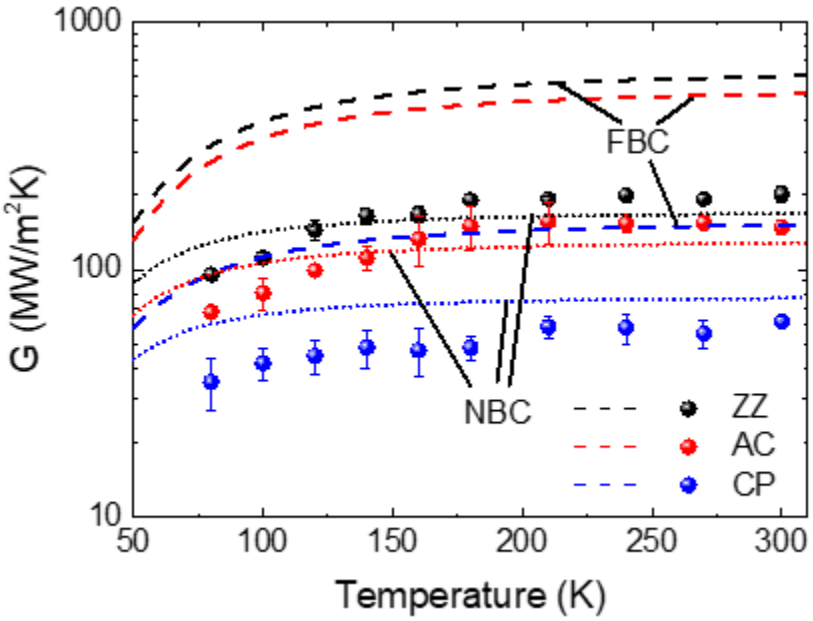

Figure 3.11 Experimentally measured TBRs (dots) of Al-BPh interfaces in comparison to calculations (lines), considering temperature dependence and different crystal orientations.

To further quantify TBR between Al and BPh along the different crystal directions and phonon mode conversion across branches, we performed the nonequilibrium molecular dynamics (MD) simulations. In the MD simulation domain illustrated in Figure. 3.12 (a), BPh is sandwiched by two Al blocks. A periodic boundary condition is applied to all the directions and the real structure can be interpreted as an Al/BPh superlattice, with heat source and hear sink layers lie in the center of BPh and Al. To minimize the lattice mismatch at the interface between BP and Al, the supercells were 60×5×12, 11×5×50 and 11×20×12 for BPh and 50×13×13, 9×13×50, 9×50×13 for Al respectively when the interface is normal to the ZZ, AC and c directions. The strain on these three interface systems is below 0.2%. Application of heat current through the heat source to the heat sink forms a temperature gradient along the direction normal to the interface. By monitoring the temperature drop (ΔT) across the interface, the thermal boundary conductance can be calculated from $G = \frac{Q}{\Delta T}$. In our simulation, the embedded-atom method empirical potential[148] was used for describing the interaction between Al atoms. The Stillinger–Weber potential and Lennard-Jones (LJ) potential were adopted for the intra- and inter-plane interactions in BPh, respectively[149–151]. The interfacial interaction between Al and BPh was simulated using LJ potential $V_{ij} = 4\varepsilon\left[\left(\frac{\sigma}{r_{ij}}\right)^{12} - \left(\frac{\sigma}{r_{ij}}\right)^{6}\right]$, where the ε is the interatomic energy and σ the distance corresponding to the zero potential energy [151,152]. The MD simulations were performed with the open-source package, Large-scale Atomic/Molecular Massively Parallel Simulator (LAMMPS). The time step was set at 0.5 fs. The systems were relaxed under canonical ensemble at 300 K for 3 ns after a first relaxation under the isothermal–isobaric ensemble (300 K and 0 Pa) for 3 ns. Then the microcanonical ensemble was applied to the system for 4 ns. To ensure a significant temperature drop at the interface and avoid the nonlinear effect, the heat flux was set as ~ 5, 3.5, and 3.3 GW/m^2

for the ZZ, AC, and CP respectively. The heat flux was applied through the system to induce a steady-state temperature gradient for 3 ns. The temperature data in the last 1 ns was sampling for TBR calculation.

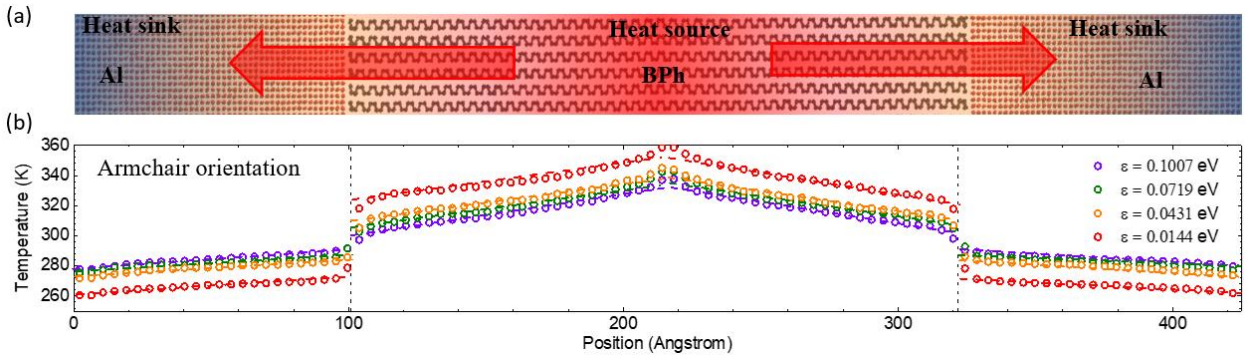

Figure 3.12 (a) Schematic of MD simulations for interfaces with different orientations. (b) Steady-state temperature profiles across the interfaces calculated using different interatomic energies (Ɛ) under a constant heat flux.

The steady-state temperature profiles of the BPh-Al system for different crystal directions are predicted by the MD simulation and shown in Figure. 3.12 (b). Here a key parameter, the interatomic energy ε, is varied to study the effects from the interfacial bonding between BPh and Al on the TBR. It's interesting to notice that the anisotropic TBR has a strong dependence on ε, and there is transition point around 0.03 eV (Figure 3.13 (a)). A larger ε stands for a stronger bonding between atoms across the interface and reduces TBR, and also potentially affect phonon conversion between different branches. When ε > 0.03 eV, MD simulation predicts $TBR_{ZZ} < TBR_{AC} < TBR_{CP}$, which is consistent with the experimental results and DMM calculations. Note that the value of ε for BPh-Al interface can be estimated following the Lorentz-Berthelot rules[153], to be around $\varepsilon_0 = 0.0719$ eV. Interestingly, at ε_0, the predicted TBRs for the interface with the ZZ and c orientations are almost similar to the values calculated with the FBC model (Figure 3.13 (b)) but deviate from NBC model (Figure 3.13 (c)). From the consistence between the MD simulation

and FBC model calculations, it can be inferred that phonon mode conversion is relatively strong at the interface along the ZZ and CP directions, but weak (although non-negligible) in the AC direction. Such an observation can be partially attributed to the cross of phonon dispersions of different branches along ZZ direction as illustrated in Fig. 3b, which opens the conversion channel between different branches. At a much lower ε, for example 0.03 eV in Figure 3.13 (c), the MD simulated TBRs decrease and approach the NBC prediction. Therefore, this study indicates the strength of interfacial bonding positively correlates with the phonon mode conversion at interface.

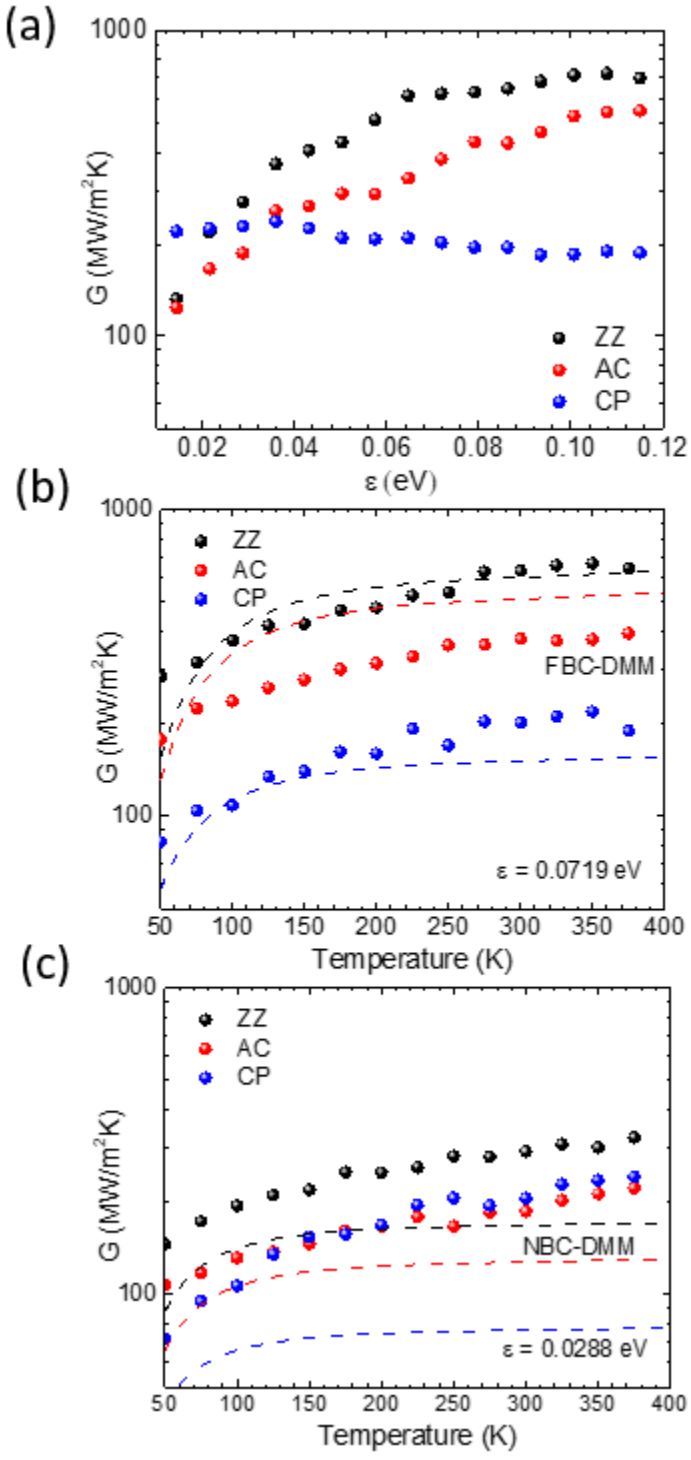

Figure 3.13 Molecular dynamic (MD) simulation of anisotropic TBRs. (a) Calculated anisotropic TBRs as a function of the Ɛ at 300 K. (b, c) Experimentally measured TBRs (dots) in comparison to MD simulations and DMM calculations for Ɛ = 0.0719 and 0.0288 eV respectively, considering three characteristic crystal orientations.

3.4 Conclusion

In summary, we report for the first time a systematic characterization of anisotropic interfacial phonon transport across metal-semiconductor materials interfaces. A record-high anisotropic ratio of TBR of 3.27 has been experimentally measured due to the strongly anisotropic phonon band structures of black phosphorus. The spectral transmissivity of phonon transport across interfaces with different orientations has been analyzed by using *ab-initio* calculated full phonon dispersions from DFT. The temperature dependent anisotropic TBR measurement and DMM calculations suggest the existence of phonon conversion between different branches under phonon gas theory. Moreover, molecular dynamic simulation was performed to implicitly include all the anharmonic effects and phonon mode conversion and show consistence with experimental results. Our experimental measurements and theoretical calculations of the thermal transport at the metal-semiconductor interface provide a detailed fundamental understanding of TBR-structure relationships. This knowledge provides important guidance for improving the thermal boundary resistance in nanoscale electronic devices, and may open up new opportunities in the rational design and control of novel interface materials for advanced thermal management technologies. Note that BPh serves as a concept-of-proof study in this work, but such anisotropic interface energy transport can be extended to more energy forms and wide range of systems such as layered materials, supper lattices, and any inhomogeneous structures. We also expect such anisotropic TBRs are becoming more important for scale-down device structures in 3D and at the nanoscale. In addition, how to take the advantage of interface anisotropy to design new device operation schemes, for example thermal switch or thermal diode for thermal management, could be other interesting research directions.

CHAPTER 4

Thermal Energy Across Molecular Junctions Enabled by Dipole Coupling

4.1 Introduction

Energy transport in molecular junction is critically important to the development of next generation atomic level electronic devices and had been a hot research area during the last three decades, however mainly focused on charge transport across molecular devices[154–158]. The experience that the high-power density and inefficient heat dissipation has become the major technology bottleneck of the current nanoscale semiconductor electronics, is warning us of the importance of thermal transport properties of future atomic or molecular electronics development[98,102,109,159–161]. On contrary with the mist of charge transport raised by numerous research results, thermal transport across molecular junction remains far less explored and is focused on modelling work[162,163]. So far, only several major factors such as molecule types, functional group of molecular head, binding chemistry at anchor atoms had been revealed as dominant factors for thermal transport across molecular junctions[164,165]. For example, the hydrophobicity of head group of self-assembled monolayer (SAM) significantly affects the thermal conductance across molecule-water interface[166]. Different binding energy between molecules and substrate, such as thiol-metal binding and silane-silicon binding is also a dominant factor[167]. Some other important factors are still wearing their mask had more investigation not been

conducted, like the extremely important coulomb forces in organic systems, including hydrogen bond and dipole-dipole effects.

Dipole-dipole interaction plays a critical role in organic molecules involved systems, including but not limited to molecular electronics, molecular biology, and pharmacy[168–170]. For example, the intermolecular between proteins and local environment and intramolecular between different functional parts of proteins determines their conformation and biology functionality[171]. On the other hand, the thermal transport across molecules determines the local temperature of cells, which could affect the efficient circulation of blood or the survival time of bacteria and virus[172,173]. Therefore, dipole-dipole effects on thermal transport across molecular junction is essentially important for future molecular devices, fundamental understanding of cell biology and novel thermotherapy development. Here, we show a comprehensive study on dipole-dipole effects on interfacial thermal transport across molecular junctions.

4.2 Experimental measurements across molecular junctions

To systematically study role of dipole moments on interfacial thermal transport across molecular junctions, we prepared self-assembled carboranethiol monolayer with different dipole moments on gold surface. The atomic geometries of carbonranethiol are illustrated in Figure 4.1. The carbonranethiol molecules have icosahedral geometry constructed with 10 boron atoms and 2 carbon atoms[174]. Carboranethiols are ideal molecules for the study of dipole effects because their dipole moment can be altered by only changing the relative positions of carbon and boron atoms without any modification of the molecular framework and they have extraordinarily chemically and thermally stability[175]. The carboranethiol molecules are named as ortho-, meta-, and para-carborane based on the zero, one or two atoms separation of two carbon atoms in the cage. Here,

five types of carboranethiol, i.e., P1, M1, M9, O1 and O9 with distinct dipole moments are used in this study. The dipole moments of P1, M1, M9, O1 and O9 ranges from near zero up to 4 Debye[176]. Since the chemical composition and molecular structure do not change, the difference of thermal transport across different molecules are attributed to the difference of dipole moments. The molecules are self-assembled on gold surface in ethanol solution till the formation of self-assembled monolayer (SAM). The uniformity of SAMs adsorption on gold substrate is verified by scanning tunneling microscope in Figure 4.2.

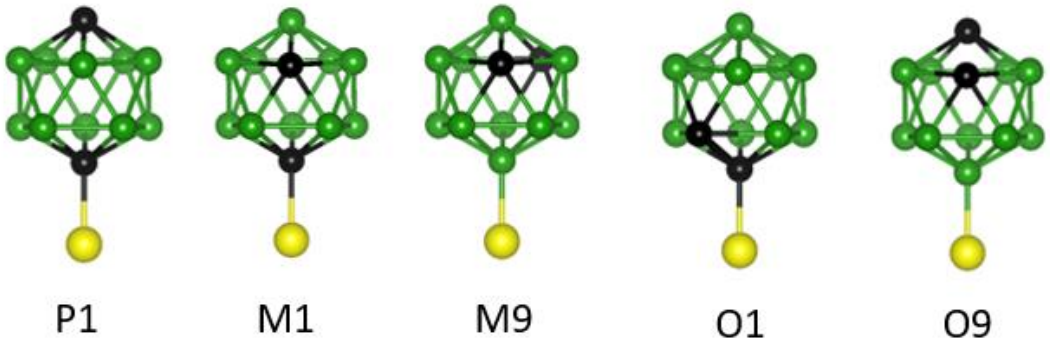

Figure 4.1. Atomic geometries of different carboranethiol molecules, i.e. P1, M1, M9, O1 and O9.

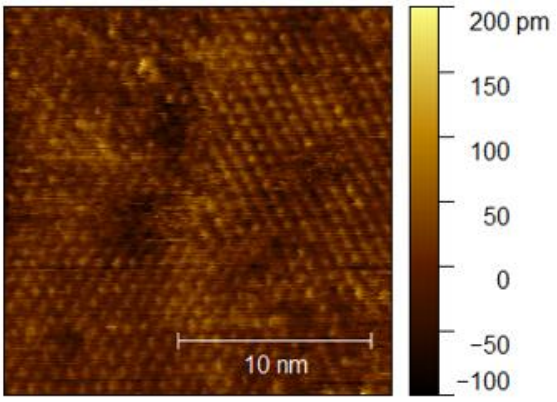

Figure 4.2 Scanning tunnelling microscopy image from M9 carboranethiol adsorbed on gold substrate

One of the most challenging part for studying thermal transport across molecular junctions is the thermal measurement at sub-nanometer scale. Here, we apply an ultrafast pump probe spectroscopy technique called time-domain thermoreflectance (TDTR) to capture the dynamic heat transport process across molecules[53,177,178]. The TDTR setup is as shown in Figure 4.3, where the femtosecond laser pulse is generated in Ti:Sapphire cavity and divided into pump and probe beams. The high energy photons in pump beam heat up the gold substrate instantaneously while the reflectance of probe beam is used to detect the temperature of the surface via thermoreflectance. The arrival time on gold of probe beam is delayed relative to the pump beam by the delay stage and thus the temperature evolution could be continuously sampled. To improve the signal to noise ratio, the pump beam is modulated by electric-optical modulator and the lock-in amplifier is used for signal detection. The temperature decay can be compared with the solution of heat conduction differential equation to extract the desired thermal properties, our focus of which is interfacial thermal conductance in this study. For example, the temperature decay curves across different interfaces are plotted in Figure 4.4, Au/water, where the Au/M9/water interface shows fastest temperature decay rate, Au/M1/water the second and Au/water the slowest. From the temperature decay rates, we can infer that the thermal conductance across Au/M9/water is highest, followed by Au/M1/water interface and Au/water.

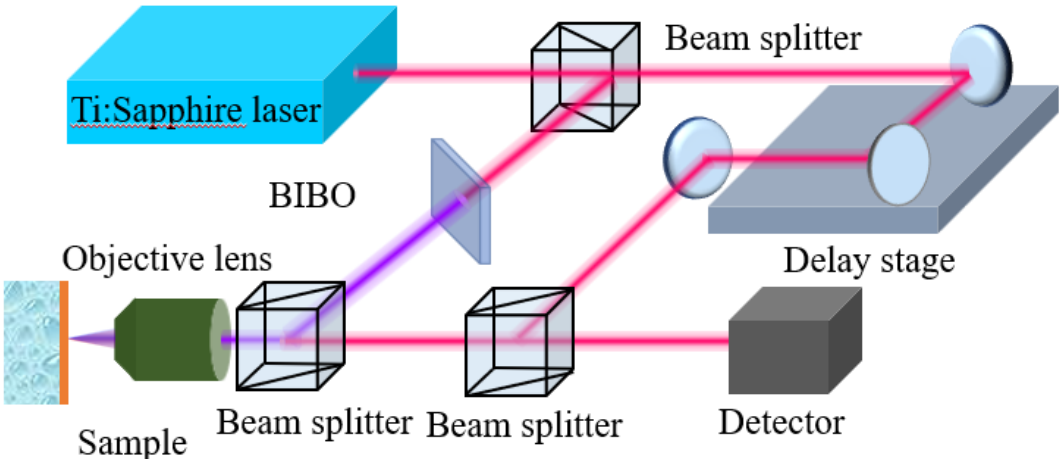

Figure 4.3 Experimental setup of ultrafast time-domain thermoreflectance measurement

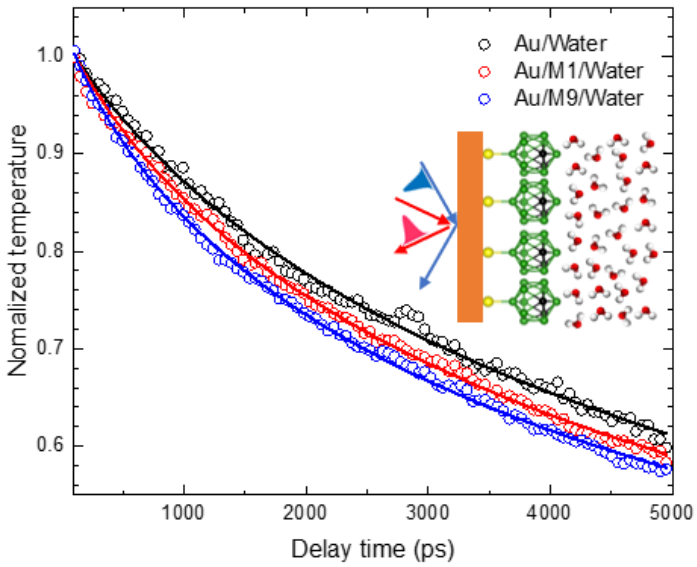

Figure 4.4 Temperature decay of gold at the molecular junction of Au/M1/Water and Au/M9/Water.

To investigate how the dipole-dipole interaction affects thermal transport across molecular junction, we measure the thermal conductance between different SAMs and liquids with significantly different dipole moments. First, the hexane is tested as a nearly zero dipole moment liquid. The thermal conductance across hexane and different carboranethiol molecules is measured

and plotted in Figure 4.5. The thermal conductance remains around 28±5 MW/m^{2}K regardless of the dipole moments of the SAMs, indicating that the different dipole moments of SAMs do not affect the thermal transport because there is no dipole-dipole interaction between SAMs and nonpolar hexane. On the other hand, the results also exclude other possible factors arising from the different SAMs, which might affect the thermal conductance. Therefore, the difference of thermal conductance across different SAMs and polar liquid would result from the dipole-dipole effects.

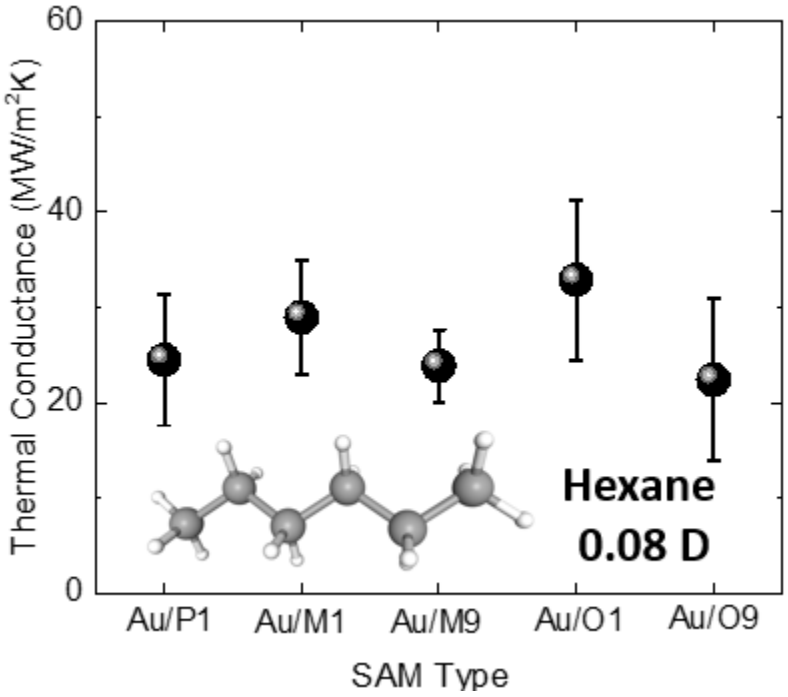

Figure 4.5 Thermal conductance across Au/SAMs/hexane interfaces

As the most common liquid, water is tested as a polar liquid with dipole moment of 1.85 D. The thermal conductance increases from 43 to 103 MW/m^{2}K with improved dipole moments of SAMs as shown in Figure 4.6. In another word, the dipole-dipole interaction between water and SAMs enhances up to 139% of the interfacial thermal conductance.

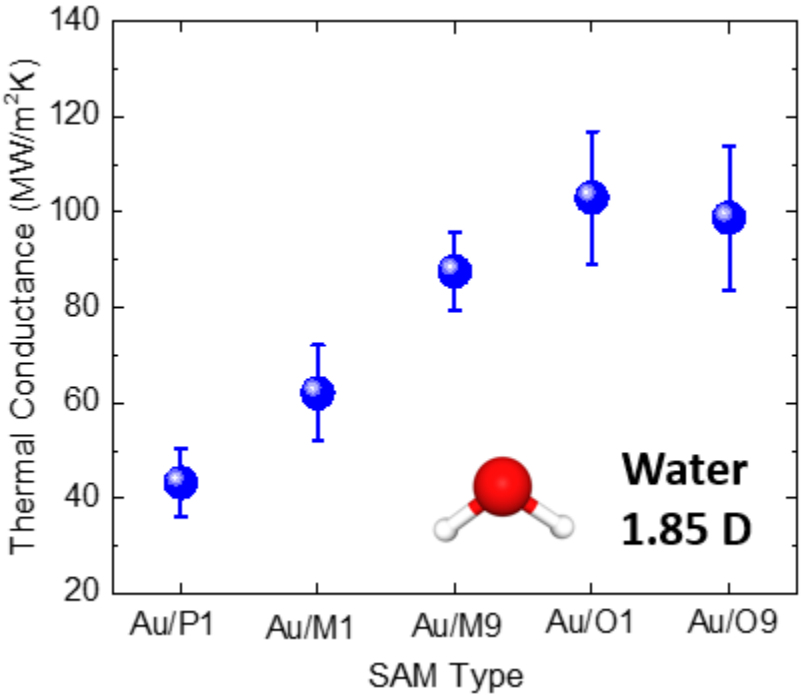

Figure 4. 6 Thermal conductance across Au/SAMs/water interfaces

Moreover, the contribution could be further improved by using liquid with even larger dipole moment. In Figure 4.7 (a-c), the thermal conductance across SAMs and polar liquids, i.e., ethylene glycol (EG) and dimethylformamide (DMF) with dipole moment of 2.36 D and 3.82 D are plotted. The thermal conductance increases from 48 to 132 MW/m^{2}K for Au/SAM/EG interfaces and from 10 to 42 MW/m^{2}K for Au/SAM/DMF interfaces. The enhancement of thermal conductance reaches up to 175% and 320% for EG and DMF involved junctions. It could be concluded from the experimental observation that molecular junction made with highly polarized molecules could significantly amplify the thermal transport efficiency. Moreover, the ionic liquid with separated positively and negatively charged ions is also tested in our study. 1-hexyl-3-methylimidazolium hexafluorophosphate is used in this study. The thermal conductance increases from 24 to 79 MW/m^{2}K. The thermal conductance enhancement is around 229%, slightly lower

than the DMF involved junctions. At atomic scale, the energy exchange rate is proportional to the product of interatomic forces and their velocities. Even though the coulomb force is only related to the interatomic distance and carried charges regardless of atom types, the vibrational velocity of ionic liquid is limited by the large molecular mass. As a result, the thermal conductance enhancement by dipole-dipole effects is not improved further by the larger polarity of ionic liquid.

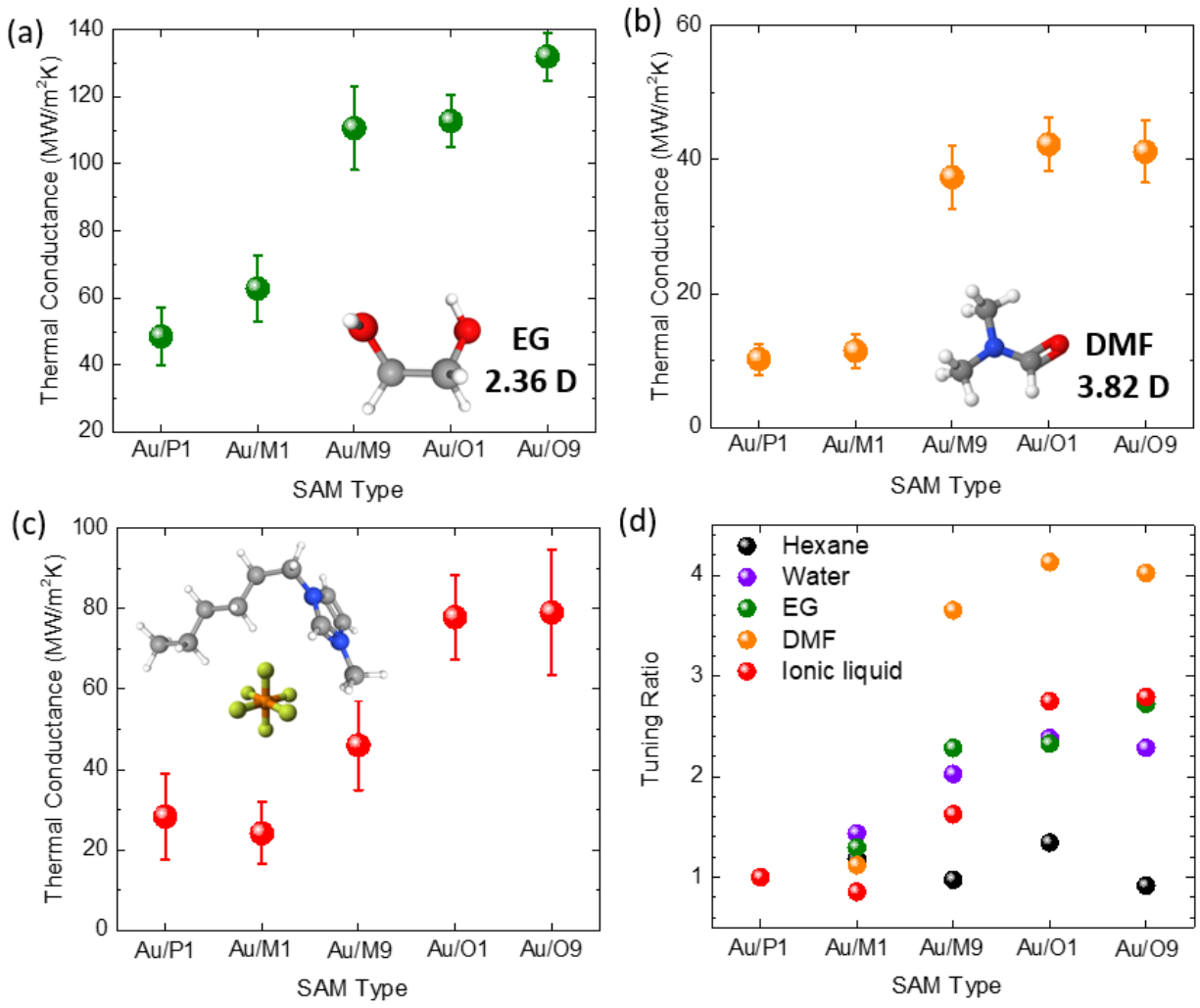

Figure 4.7 Dipole-Dipole effects on thermal conductance across Au/SAMs/Liquid interfaces. (a). Thermal conductance across Au/SAMs/ethylene glycol interfaces. (b). Thermal conductance across Au/SAMs/dimethylformamide interfaces. (c). Thermal conductance across Au/SAMs/ 1-hexyl-3-methylimidazolium hexafluorophosphate interfaces. (d). A summary of thermal conductance improvement by dipole-dipole interaction between different molecules and liquids.

4.3 Atomistic modelling of dipole-dipole effects on thermal transport

To reveal the fundamental mechanism of thermal transport contribution by dipole-dipole interaction, molecular dynamics simulation is performed. In the simulation, SAMs are embedded between gold and different liquid as illustrated in Figure 4.8 A. Two ends of the sandwich structure serve as heat source and heat sink. The interatomic interaction for gold, SAMs and liquid are described by embedded atom method, MM3, SPC and OPLS potentials, respectively[179–183]. The charges with atoms in carboranethiols are taken from the Mulliken charge calculated from density functional theories (DFT)[175]. The van der Waals interactions between different materials is described with Lennard-Jones function and parameterized from the modified universal force field and the Lorentz–Berthelot rule. The thiol-gold covalent bond is described with Morse potential with binding energy calculated from DFT. To minimize the mismatch at interface, the carboranethiols is adsorbed on gold with a supercell of (5×5) R30^{o}. The total simulations size of gold and liquid are 50×43.5×270 nm and 50×43.5×200 nm. The whole systems are first relaxed under isothermal–isobaric ensemble at 300 K and 1 atm for 2.5 ns and then relaxed under canonical ensemble for 2.5 ns and microcanonical ensemble for 2 ns. All the MD simulations are performed with Large-scale Atomic/Molecular Massively Parallel Simulator (LAMMPS)[184]. Finally, the thermal conductance can be calculated from the given heat flux and temperature difference at the interface as shown in Figure 4.8 A using equation $G = \dot{Q}/\Delta T$.

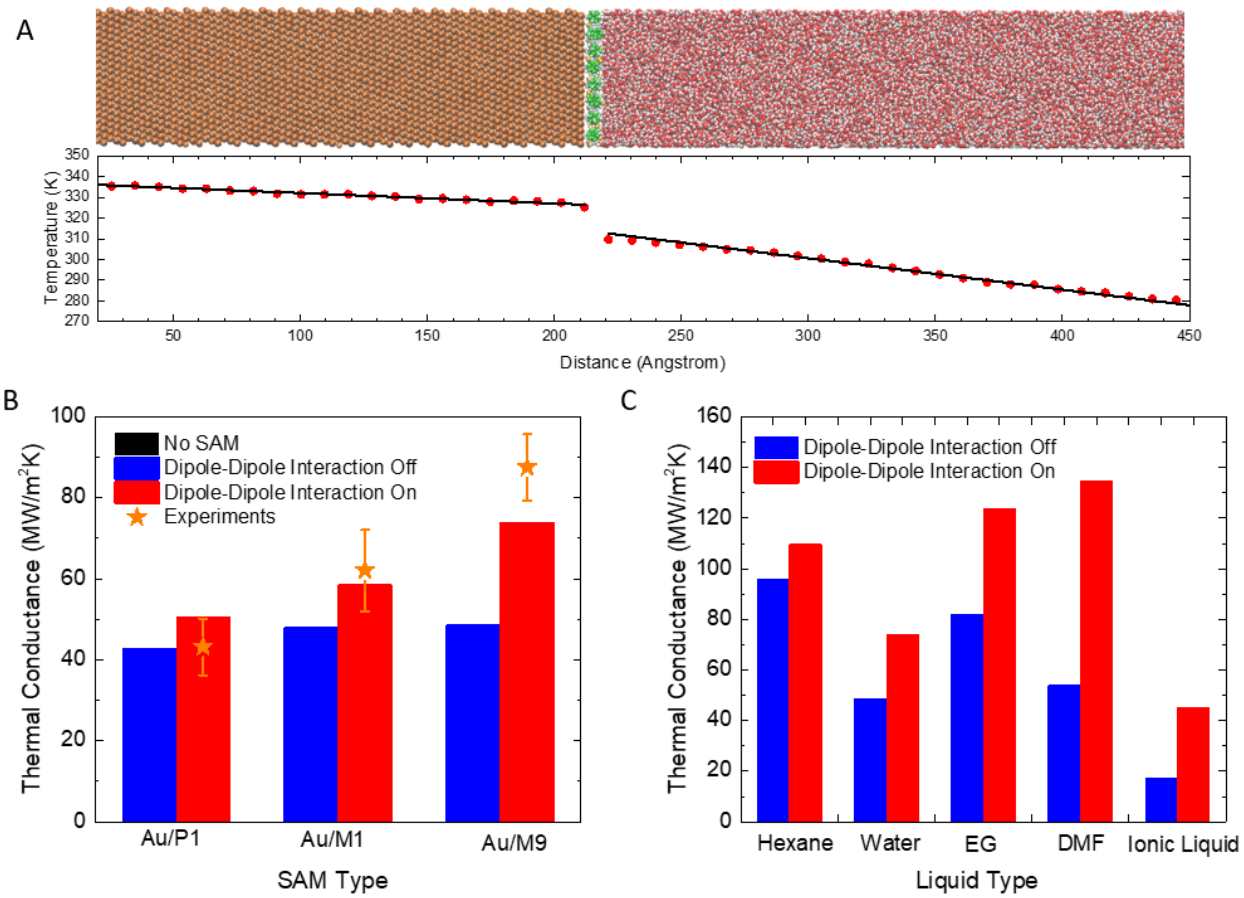

Figure 4. 8 Atomistic modelling of thermal transport across molecular junctions. A. Schematic of the molecular dynamic simulation of Au/SAM/Liquid interfaces and the steady-state temperature distribution under fixed heat current along the system. B. Simulated thermal conductance across Au/water, Au/P1/water, Au/M1/water, and Au/M9/water interfaces with dipole-dipole interaction turned on and off. C. Simulated thermal conductance across Au/M9/Liquids, including hexane, water, ethylene glycol, dimethylformamide and 1-hexyl-3-methylimidazolium hexafluorophosphate with dipole-dipole interaction turned on and off.

Figure 4.8 B compares the simulated thermal conductance across Au/SAMs/water junctions made with P1, M1, M9 as representatives of molecules with weak, intermediate, and strong dipole moments. Consistent with our experimental results, the junction made with M9 has higher thermal conductance than junction made with M1 and P1 shown by the red columns in Figure 4.8 B. One of the advantages of atomistic modelling is to freely control dipole-dipole interaction directly. To further confirm that the enhancement of thermal conductance is truly from

dipole effects, we artificially tune off the coulomb interaction between SAMs and water. The results are shown by the blue columns. The thermal conductance values for P1, M1 and M9 involved interfaces are 43, 48, 48 MW/m^{2}K with dipole-dipole interaction, and 50, 58 and 74 MW/m^{2}K without dipole-dipole interaction. First, no observable difference of thermal conductance between different molecule can be found after the dipole-dipole interaction turned off, which means the thermal conductance by van der Waals interaction does not vary with molecules since they share the same molecular skeleton. Second, the enhancement of thermal conductance indicated by red columns over those without dipole-dipole interaction increase with the dipole moments of SAMs. Both observations agree with our experimental observations and support our hypothesis that dipole-dipole interaction is significant to interfacial thermal transport across molecules and this significance increases with the dipole moments of the molecules.

Furthermore, the simulations are also performed for the molecule junctions between M9 and different liquid. The results are plotted in Figure 4.8 C. When the dipole-dipole interaction is on, the thermal conductance across interface between M9 and hexane, water, EG and DMF is 95, 48, 82, 54, 17 MW/m^{2}K, which are enhanced up to 109, 74, 124, 134, 45 MW/m^{2}K respectively while dipole-dipole interaction is on. The enhancement percentage is around 15%, 54%, 51%, 148% and 164%. Similar with the dipole effects from SAMs, the thermal conductance enhancement percentage represented by red columns over those without dipole-dipole interaction increase with the dipole moments of the liquids, which is also consistent with the experimental measurements.

4.4 Conclusion

In conclusion, the thermal transport across molecular junctions made with materials with different dipole moments were measured with ultrafast pump probe spectroscopy. Strong enhancement of thermal conductance up to 320% were observed for the junctions with large dipole moments SAMs and liquids. Our observations are further confirmed by the atomistic modelling. By artificially switching the dipole-dipole interaction in the simulations, the thermal conductance contributed by the van der Waals interaction and coulomb interaction were separated. The large contribution from dipole-dipole interaction to the thermal conductance from our simulation results explained the experimental measurements. This study will establish our knowledge of thermal transport by dipole-dipole interaction and open up new opportunities in molecular engineering for thermal, electronic, energy conversion and medical system.

CHAPTER 5

Heat Dissipation through the Interface Integration of Boron Arsenide

5.1 Introduction

Thermal management has been a serious technology hurdle in semiconductor industry for decades. The continuous size reduction of modern electronic devices has expanded the heat dissipation issue down to the nanoscale, calling for the development of new materials with high thermal conductivity (HTC)[185–188]. Recently, building on ab initio theoretical calculations[189–196], a new class of boron compound semiconductors, including boron arsenide (BAs)[197–199] and boron phosphide (BP)[200], has been experimentally realized and verified with record-high thermal conductivity . In particular, our recent study[197,201] has measured an isotropic thermal conductivity of 1300 W/mK in BAs, beyond that of most known heat conductors, and over three times that of the industrial HTC standards such as copper and SiC (both around 400 W/mK). With high application promise, the design and integration of these new HTC materials with other materials layers is critically important towards their future device implementation, however, has remained to be explored. Here, we report the first systematic study of interfacial integration and nanoscale energy transport across these new HTC semiconductors with prototype metal and semiconductor materials. As demonstrated through ultrafast spectroscopy experiments and atomistic to multi-scale modeling, BAs and BP, with their intrinsic semiconducting nature and phonon band structures, provide a significant improvement of the thermal boundary conductance and thermal management performance.

With the continuous emergence of novel nanomaterials and nanoelectronic devices, nanoscale thermal management has to take into consideration that heat dissipation across integrated devices (Figure 5.1a) depends on not only the materials' thermal conductivity, but also the interfacial thermal transport between different working layers[202,203]. The key metric to quantify the interfacial thermal transport is the thermal boundary resistance (TBR): $TBR = \Delta T/Q$, where ΔT and Q are the temperature drop and heat flux across the interface, respectively[204]. A small TBR together with a high thermal conductivity are desirable to achieve efficient heat dissipation. Fundamentally, TBR arises from the mismatch across the interface of atomistic vibrations, the quantum mechanical modes of which are defined as phonons[205]. Despite decades of efforts, understanding and improving TBR still remains challenging. Under the classical Debye model, vibrational properties of materials is approximated as the linear phonon dispersion, and the maximum temperature of the highest phonon frequency is defined as the Debye temperature (Θ_D)[206]. Therefore, in the literature a simplified evaluation metric, which qualitatively estimates the overlap between phonon spectra, is to compare the Debye temperatures[204]. Based on that, a smaller difference in Debye temperature between materials across the interface expects a smaller TBR. Figure 5.1b shows the Debye temperatures for typical semiconductors, metals, and HTC materials. Most semiconductors (Si, Ge, GaAs, GaN) and metals (Al, Au, Ni, Pd, Pt, Ti) usually have a low Θ_D (e.g., below 700 K). However, the traditional prototype HTC materials, i.e. diamond and cubic BN, as a result of their large phonon group velocity, have a much higher Θ_D (over 2000 K). Indeed, literature studies reveal a high TBR for integrated diamond or BN, despite their HTC. For example, the interface between diamond and GaN, has a mismatch in Θ_D over 1500 K, leading to TBRs usually of ~ 30 m^2K/GW[207–209]. In comparison, the Θ_D of BAs and BP is much lower; for example, BAs has a Θ_D of ~ 700 K. According to this estimation, the new HTC materials BAs and BP hold high

promise for TBR improvement upon integration with typical metals and semiconductors for electronics cooling applications.

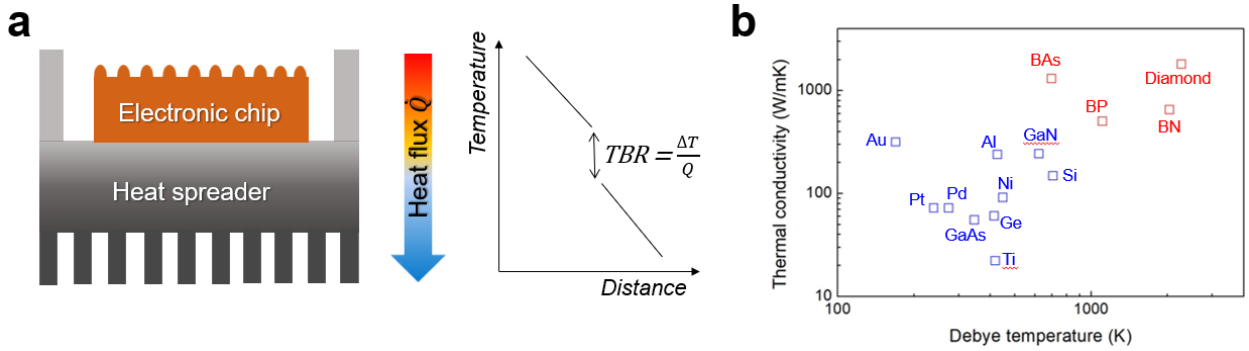

Figure 5.1 Nanoscale thermal management using integrated HTC materials as cooling substrate to improve heat dissipation. a. Schematic illustrating heat dissipation and thermal boundary resistance at the interfaces in microchip packaging. b. Room-temperature thermal conductivities and Debye temperatures of representative metals, semiconductors, and HTC materials.

5.2 Thermal transport across boron compounds and metals

First we measured the thermal transport across the interfaces of the HTC materials with various metals. Metal films, including Al, Au, Ni, Pd, Pt, Ti, and Ni, are deposited on top of BAs and BP thin films (~80nm) using an electron beam evaporation technique to form a clean metal-HTC interface, as verified by cross-section scanning electron microscopy (SEM) (Figure 5.2a). The TBR was measured using ultrafast pump-probe spectroscopy, the time domain thermoreflectance (TDTR) technique, illustrated in Figure 5.2b. TDTR is an ultrafast technique that is widely used for measuring thermal properties and TBR of different materials[195,197,200,202,210]. In our setup, a femtosecond pulse laser with 80 MHz repetition rate is generated by a Ti:Sapphire optical cavity and divided into pump and probe beam. The pump beam doubles its frequency (i.e.,

at the wavelength of 400 nm) after passing through a second harmonic generator, and is used to thermally excite the sample surface. The probe beam, at the wavelength of 800 nm, is used to detect the sample temperature. The time delay between pump and probe beams is precisely controlled by a mechanical delay stage with a sub-picosecond resolution. To determine TBR, the transient TDTR signal is detected and fitted to a multilayer thermal model (Figure 5.2c). More details regarding TDTR and TBR measurements can be found in our other recent studies[202,211]. We used 10 μm ($1/e^2$) beam radius with 9.8MHz modulation frequency to obtain accurate TBR values. We do not observe any frequency dependent TBR changes in measurement. It is also noticed that steady-state heating from pump and probe laser is less than 2K for both materials during measurement.

Figure 5.2(d, e) shows measurement results of the temperature dependent thermal boundary conductance (G), i.e. the reciprocal value of TBR. In general, metal interfaces with BAs and BP show high thermal conductance. The value of G varies for each metal but has a similar trend between BAs and BP: For example, Au and Ti have the lowest and highest G values, respectively. The measured thermal boundary conductance values at room temperature between BAs and Au, Pt, Al, Pd, Ni, and Ti are 85, 133, 250, 290, 309, 310 MW/m^2K, respectively. These values are slightly higher than that obtained with BP, as expected from the difference in Θ_D. From 300K to 600K, no significant temperature dependence is observed for G, indicating that a complete phonon excitation and a saturated phonon population are involved in the interface transport. It should be noted that the thermal boundary conductance of BAs and BP with metals are typically over 4× and 2.5× higher, respectively, than that of a metal-diamond interface[212], which supports a high heat dissipation efficiency.

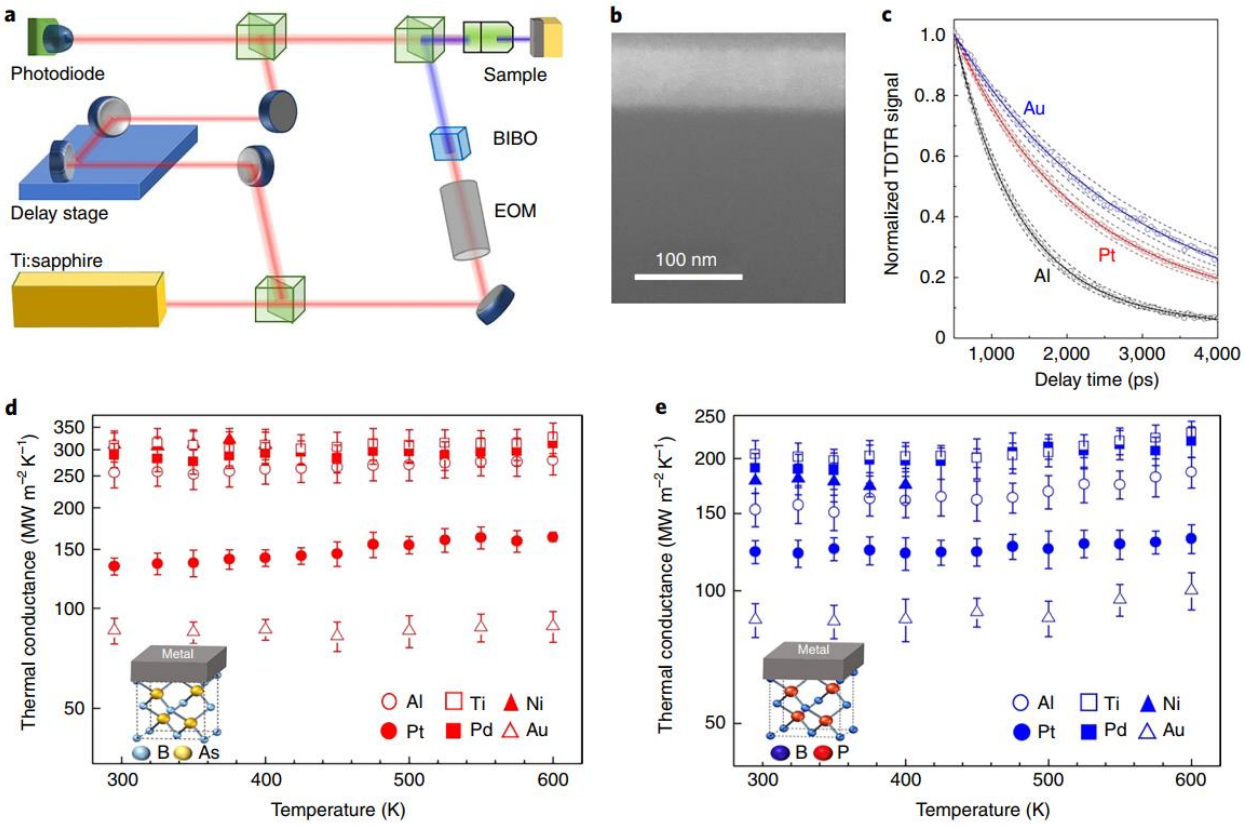

Figure 5.2 Metal-HTC interfaces and ultrafast optical spectroscopy measurements of temperature-dependent thermal boundary conductance. a. BAs and BP as cooling substrate for metal films; cross-section SEM image of a typical sample: Top layer is aluminum film and the bottom layer is BAs. b. Schematic of the time-domain thermoreflectance (TDTR) measurement set-up. Blue and orange routes represent pump and probe laser beams. c. Typical TDTR experimental data versus time (circles), fitted to the thermal transport model (solid lines). Calculated curves (dashed lines) with the thermal boundary conductance changed by ±10% of the best values to illustrate measurement accuracy. d and e. Experimental results for the temperature-dependent thermal boundary conductance between varied metals with BAs and BP, respectively.

To better understand our experimental results, we performed atomistic calculations to capture the phonon spectral contributions to the interfacial energy transport. Under the phonon picture, TBR can be understood as resulting from the breakdown of coherence of the mode-dependent phonon transport across the interfaces[204]. As illustrated in Figure 5.3a, when the incident phonons encounter the interface, partial transmission (i.e., partial reflection back) could

happen, but with different probabilities for each phonon mode. Understanding this mode-dependent transmission probability (τ) is challenging, particularly in that the actual phonon spectra has mode-dependent properties including group velocity, specific heat, relaxation time, and anharmonic interactions[213]. To develop an atomistic understanding of the interface phonon transport, we first performed *ab initio* calculations[196,202,210] based on density functional theory (DFT) to obtain the detailed phonon band structures of the different materials (Figure 5.3b). The second-order interatomic force constants were calculated using the finite displacement method. For all the materials considered here, the projector augmented wave pseudopotential with the local density approximation was used. For each structure, a supercell with a 3×3×3 cubic unit cell with periodic condition was constructed for DFT calculations using Quantum Espresso package[214]. A 12×12×12 Monkhorst-Pack mesh was used for the reciprocal space and the kinetic-energy cut-off for the plane-wave basis set was 600 eV. By displacing the atoms with a finite distance of 0.03 Å, the second order force constants were extracted with the Phono3py package. Our calculated phonon band structures were compared with neutron scattering and Raman scattering experiments[197,215–218] and show good consistency (Figure 5.3b). The phonon density of states (PDOS) were also calculated and plotted on the right side of Figure 5.3b. Note that PDOS defines the number of available quantum states for each phonon energy. The PDOS overlap across the interface dictates TBR as it determines the probability to prepare phonons before incident on the interface and to accommodate phonons after transmission from the interface. Therefore, a larger PDOS overlap qualitatively indicates a lower TBR. The results in Figure 5.3b show that the dominant range of PDOS spans from 15 to 40 THz for diamond, and from 0 to 20 THz for BAs or BP. In comparison, the PDOS is mainly distributed between 0 and 10 THz for most metals. In particular, the cutoff acoustic frequencies are 32.0 THz in diamond, 16.1 THz in BP, 9.6 THz in

BAs, 9.5 THz in Al, 6.1 THz in Pt, and 4.9 THz in Au. These PDOS spectra show that BAs overlaps best with most metals, followed by BP, and with diamond as the worst option. The comparison of PDOS further explains the improved TBR with BAs/BP versus diamond, as well as the variation between different metals, which is consistent with the experimental results shown in Figure 5.2d, e.

We developed more quantitative calculations of the TBR by taking advantage of our *ab initio* derived phonon band structures. Under the Landauer-Buttiker formulation[219,220], the TBR can be calculated based on the mode-dependent properties as:

$$\frac{1}{TBR} = G = \frac{1}{2(2\pi)^3}\sum_i \int_{\boldsymbol{k}}^{whole\ k\ space} \tau_{12}(\boldsymbol{k},i)\hbar\omega(\boldsymbol{k},i)|\boldsymbol{V}(\boldsymbol{k},i)\boldsymbol{n}|\frac{df}{dT}d\boldsymbol{k} \qquad (5\text{-}1)$$

where $\tau_{AB}(\boldsymbol{k},i)$, $\omega(\boldsymbol{k},i)$, $\boldsymbol{V}(\boldsymbol{k},i)$, $f = \frac{1}{\exp\left(\frac{\hbar\omega(\boldsymbol{k},i)}{k_B T}\right)-1}$ are the transmission coefficient, frequency, group velocity and equilibrium Bose-Einstein distribution function of phonons with wavevector $\boldsymbol{k}$ and polarization i. $\boldsymbol{n}$ is the unit vector normal to interface. The subscript indicates the material on side 1 or side 2 across the interface. The transmission coefficient term ($\tau_{12}(\boldsymbol{k},i)$) is a key parameter to quantify how many phonons are reflected or allowed to transmit through the interface, as illustrated in Figure 5.3a. The exact determination of $\tau_{12}(\boldsymbol{k},i)$ remains challenging for state-of-the-art phonon theories, however, the lower limit of TBR can be considered when the transmission of all overlapping phonon modes reaches 100%, i.e., the Radiation limit[221]. Under this Radiation limit, the phonon transport is similar to radiation heat transfer between blackbodies, so that all the emitted phonons from the one side of the interface would be accepted by the absorption side once the state of phonons are allowed into the absorption side. Mathematically, the transmission coefficient would be unitary, i.e., $\tau_{12}(\boldsymbol{k},i) = 1$ if the frequency of the emitted phonon from side 1 is lower than the maximum phonon frequency in side 1. The maximum G values based on the

Radiation limit, plotted as dotted lines in Figure 5.3c, are 953 MW/m^{2}K for an Al-BAs interface, 652 MW/m^{2}K for an Al-BP interface, and 232 MW/m^{2}K for an Al-diamond interface. As expected, the experimental results for the different interfaces follow the order predicted by the Radiation limit, but the experimental values are far below this maximum limit, as a full transmission cannot be achieved for practical interfaces. Alternatively, the interface transmission $\tau_{12}(\boldsymbol{k}, i)$ was calculated by considering the diffuse mismatch model (DMM) between phonon spectra across the interfaces. Under this consideration, all the phonons are assumed to be diffusely scattered by the interface, i.e., phonons lose their memory after scattering at the interface. In other words, the phonons re-emitted from the interface can originally be from either side of the interface, i.e., $\tau_{12}(\boldsymbol{k}, i) = 1 - \tau_{21}(\boldsymbol{k}, i)$. By applying this physical constraint and considering the detailed balance of heat flux[222], the transmission coefficient can be calculated as:

$$\tau_{12}(\boldsymbol{k}, i) = \frac{\sum_i \int_{\boldsymbol{k}}^{Side2} |\boldsymbol{V}(\boldsymbol{k}, j)\boldsymbol{n}| \delta_{\omega,\omega(\boldsymbol{k},j)} d\boldsymbol{k}}{\sum_i \int_{\boldsymbol{k}}^{Side1} |\boldsymbol{V}(\boldsymbol{k}, i)\boldsymbol{n}| \delta_{\omega,\omega(\boldsymbol{k},i)} d\boldsymbol{k} + \sum_j \int_{\boldsymbol{k}}^{Side2} |\boldsymbol{V}(\boldsymbol{k}, j)\boldsymbol{n}| \delta_{\omega,\omega(\boldsymbol{k},j)} d\boldsymbol{k}} \qquad (5\text{-}2)$$

where $\delta_{\omega,\omega(\boldsymbol{k},i)}$ is the Kronecker delta function. Note that the *ab initio* derived full phonon band structure from DFT calculations were used for the calculation. The DMM calculated results for the interfaces between Al and BAs, BP and diamond are plotted as dashed lines in Figure 5.3c. Both the Radiation limit and the DMM calculation results show a consistent trend with the experimental measurements, i.e., $G_{\text{Al-BAs}} > G_{\text{Al-BP}} > G_{\text{Al-diamond}}$ over a wide (77 K to 600 K) temperature range. The G values between BAs and metals are much larger than that between diamond and metals, due to the better match in PDOS and the phonon group velocities. Note that the DMM predictions are higher than experimental results -- This is because DMM assumes unrealistic fully diffusive scattering at interface and results in overestimated phonon transmission coefficient.

To simulate the phonon scattering at interface more realistically, we performed molecular dynamics (MD) simulation to calculate the TBRs. We first developed the interatomic potentials for the new materials, i.e. BAs and BP directly from quantum mechanical calculations based on ab initio MD determined atomic forces using potfit package[223]. In the ab initio MD, Quantum Espresso was used to construct a supercell with a 4×4×4 cubic unit cell for BAs and BP with norm-conserving pseudopotentials in the local-density approximation. The kinetic-energy cut-off for the plane-wave basis set was 1360 eV. The Tersoff and embedded atom method potential are used for diamond and Al[224,225]. The interfacial interaction between Al and HTC materials were described using Lennard-Jones potential and the parameters were derived from the Lorentz–Berthelot rules[226,227]. To minimize the mismatch at interface, the supercell size is 10×10×80 (Al) and 11×11×80 (diamond) for Al-diamond interface, 14×14×80 (Al) and 12×12×80 (BP) for Al-BP interface, 13×13×80 (Al) and 11×11×80 (BAs) for Al-BAs interface. The whole systems were relaxed under isothermal–isobaric ensemble at desired temperature and pressure for 5 ns, followed with relaxation under canonical ensemble for 3 ns and microcanonical ensemble for 2 ns with a time step of 0.5 fs. The MD simulations were performed with Large-scale Atomic/Molecular Massively Parallel Simulator (LAMMPS)[228]. By setting anchor layers and thermal reservoirs at the two ends of the system, the steady-state temperature profile across the system under a constant heat flux can be obtained after 10 ns. The TBR values are determined from the heat flux and temperature drop at interface. The MD predicted TBRs for the interface with BAs, BP, and diamond are plotted in comparison with experimental results in Figure 5.3c. Interestingly, the MD predictions are in close to the experimental measurements; the better agreement by the MD predictions indicate a realistic interatomic interaction can better describe all the phonons behaviors at interface, including the elastic phonon scattering, high-order anharmonicity and phonon mode

conversion that such atomistic interactions dictate the macroscopic TBRs. More importantly, from the consistent trend between the Radiation limit, DMM calculation, and MD simulation, it can be concluded that the band structure of BAs facilitates efficient phonon transport across the interface and ensures its TBR to be intrinsically low.

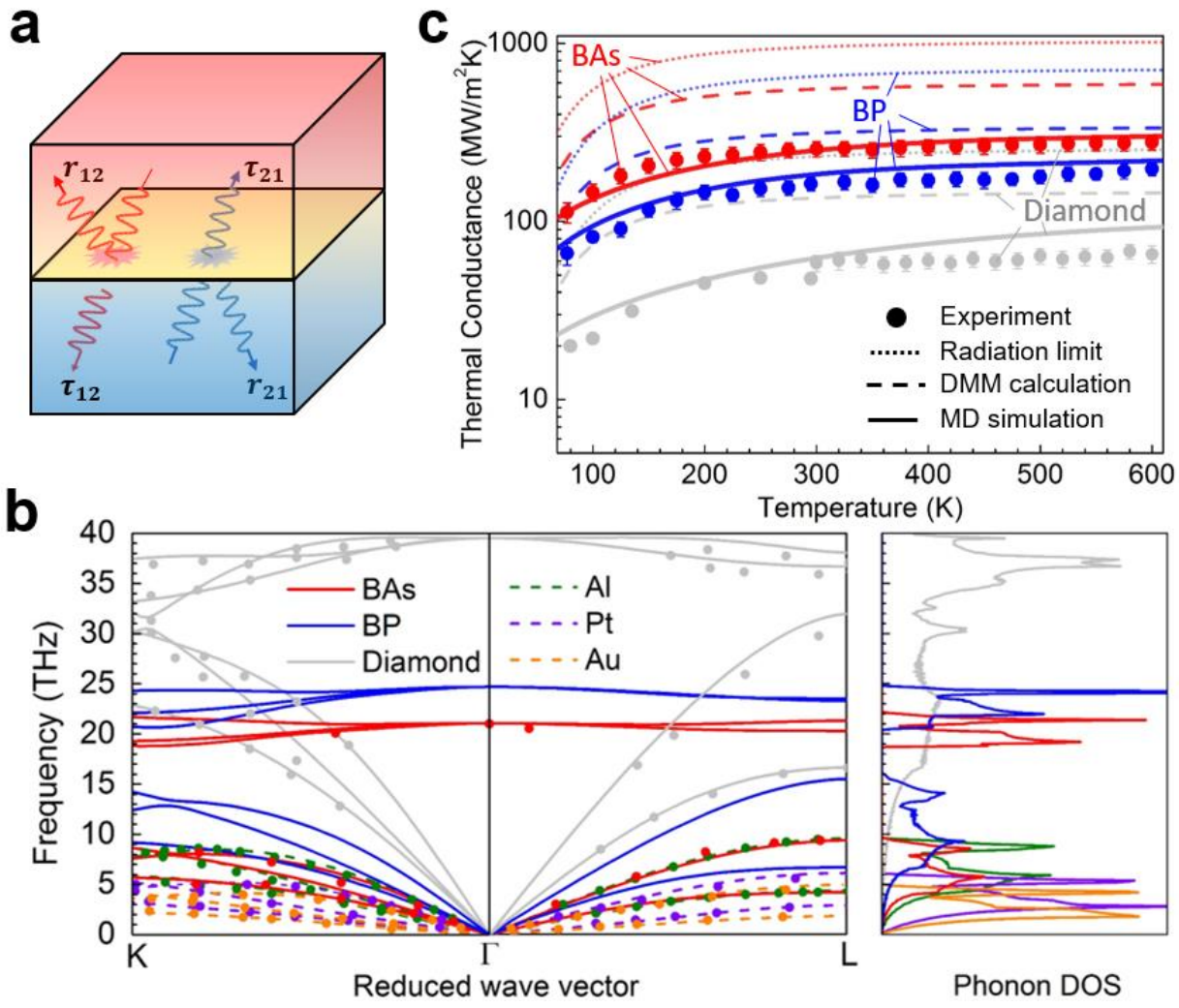

Figure 5.3 ***Ab initio*** **calculation of phonon band structures and atomistic modelling of phonon spectral contribution to the thermal boundary conductance.** a. Schematic of phonon transport with mode specific transmission (τ) and reflection probability (r) at the interface. b. Phonon dispersion relationships (left) and density of states (right) of BAs, BP, Diamond, Al, Pt, Au calculated from DFT (lines) in comparison with neutron scattering and Raman scattering experiments (dots[197,215–218]). c. Experimentally measured thermal boundary conductance (dots) of aluminum–HTC interfaces in comparison to calculations (lines), considering temperature dependence and different modeling methods.

5.3 Integration of boron arsenide cooling substrates into gallium nitride devices

As a step further, we also demonstrated for the first time the experimental integration of BAs with a prototype high-power semiconductor, i.e., GaN, and investigated their interfacial thermal transport. Recent progress has been made in integrating GaN with classical HTC materials (in particular diamond) for power cooling[19]. However, integrating GaN with BAs is challenging because crystal structures of BAs (zinc blende cubic) and GaN (wurtzite) are different, making it difficult to form epitaxial interfaces with minimum disorders. Also, BAs decomposes at about 1200K, so low temperature crystal growth is required. Here, in order to get a high quality interface between BAs and GaN, we applied metamorphic heteroepitaxy method to relax the strain[229]: We introduced a thin layer of oxide as the adhesion layer in between, using atomic layer deposition technique[230]. A follow-up treatment using oxygen plasma was used to activate interface bonds and the sample was annealed at 773K for 24 hours in vacuum. The heterogeneous interface was carefully verified by SEM and high-resolution transmission electron microscopy (HR-TEM): Figure 5.4a shows an atomically clean and uniform GaN-BAs interface with a 2 nm interlayer aluminum oxide. To measure thermal boundary conductance of BAs-GaN, we deposit ~80 nm of Al film on top of BAs. We first measured thermal conductivity of our GaN substrate by using TDTR which is 170 W/mK. Thermal conductivity of GaN and TBR of Al-BAs are input parameters of our multilayer thermal model to decide thermal boundary conductance of BAs-GaN. The thermal boundary conductance of the high quality BAs-GaN interface was measured using TDTR to be ~ 250 MW/m^2K -- Note that this conductance value is already over 8 times higher than that of the typical GaN-diamond interfaces[207–209]. Moreover, considering the thermal

resistance of oxide layer around 1 m^2K/GW 25% of our measured values and the possible blocked phonon transmission across the oxide layer, the TBR of GaN-BAs interface could be subject to further enhancement through the optimization of the resistance contribution from the oxide interlayer.

To evaluate the device-level heat dissipation performance of BAs as a cooling substrate, we performed a multiscale simulation of the hot spot temperature across a GaN-BAs interface as a function of various heating sizes that used experimental data as the input and consisted of solving the heat conduction equation and the Boltzmann transport equation (BTE). We considered an exemplary device geometry involving GaN device layer on the top of BAs cooling substrate (Figure 5.4b). A boundary line heat source with a fixed power (e.g., 10 W/mm) was placed on top of the GaN layer to serve as the hot spot, and the bottom of the substrate was fixed at room temperature. To study the size-dependent effect of the hot spot temperature, the width of the heat source was varied. Experimental data of TBR and thermal conductivity were used for these simulations. We first simulated a hot spot temperature by solving the heat conduction equation using the finite element method. In this case, thermal transport is considered as a diffusive process, where the heat flux is proportional to the temperature gradient following the Fourier's heat conduction law. The classical diffusion theory describes the thermal transport process well when the characteristic length is far larger than the phonon mean free path, and is commonly used for engineering macroscopic devices. Figure 5.4b show the hot spot temperature calculated with the heat conduction equation. The hot spot temperature increases when the heater width decreases, due to the larger heating power density. To evaluate the effect from TBR, upon intentionally removing TBR in the simulation (dotted lines), we found that, as expected due to its high thermal conductivity, diamond shows slightly advantage. However, TBR ubiquitously exists in practical

devices. When TBR was included in the simulation (dashed lines), BAs clearly has a reduced hot spot temperature than diamond, supporting its superior performance in heat dissipation through a combination of HTC and low TBR. Importantly, we also evaluated the device performance under conditions where the ballistic thermal transport takes place and the classical diffusion theory fails for nanoscale devices[195]. With the shrinking of device sizes down below the phonon mean free paths, phonon transport would not experience scattering. In this case, the practical heat dissipation behaves more like radiation rather than diffusion, so the actual hot spot temperature will deviate from the prediction by the Fourier's law. Such ballistic thermal transport and phonon mean free path spectra of GaN, diamond, BAs and BP have all been experimentally measured and analyzed in our recent studies[195,197,200]. Here, to capture the physics of thermal transport from the diffusive regime to the ballistic regime, we solved the spectral-dependent Boltzmann transport equation considering mode-dependent phonon properties for the same device structure. The three-dimensional spectral-dependent BTE is given by:

$$\frac{\partial f}{\partial t} + \boldsymbol{v}(\omega, p) \cdot \nabla f = -\frac{f - f_0}{\tau(\omega, p)} \tag{5-3}$$

where f is the phonon distribution function, and f_0 is the equilibrium Bose-Einstein distribution at the local temperature. $\boldsymbol{v}(\omega, p)$ and $\tau(\omega, p)$ are respectively the phonon group velocity and the phonon relaxation time at a certain angular frequency ω and polarization p. $\Lambda = v\tau$ is the phonon mean free path. However, it should be noted that it is challenging to solve the three-dimensional (3D) spectral dependent BTE, especially using deterministic methods. Here, to solve the BTE for the 3D experimental geometry, we calculated the spectral-dependent phonon BTE using variance-reduced Monte Carlo (VRMC) method[200]. In VRMC method, phonon bundles are initialized in the computational domain, and then proceeded following "advection – sampling – scattering" procedures[231]. In the advection procedure, the phonon bundles are moved under group velocity. In

the sampling procedure, the energy carried by the phonon bundles are sampled. In the scattering procedure, the frequencies of the phonon bundles are redistributed based on the spectral distribution of the specific heat. To determine the hot spot temperature, we calculate the temperature response to a heat pulse and integrate the response from t = 0 to infinity. All the material's spectral properties for the input into the BTE simulation come from ab initio calculations and experiments.

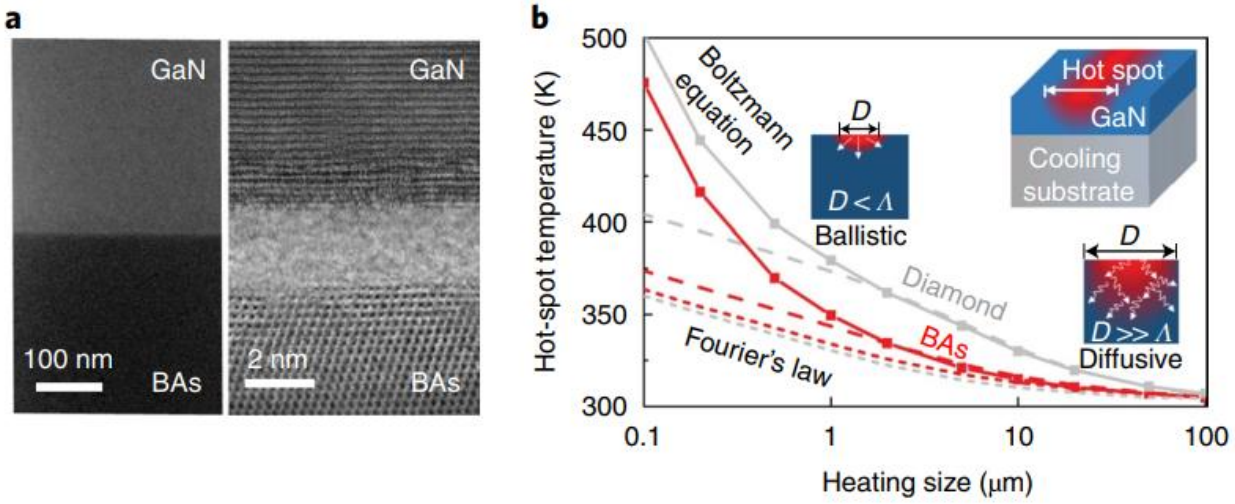

Figure 5.4 Interface integration of GaN and BAs, and device-level thermal management. a. Cross-section SEM (left) and high-resolution TEM (right) images of a typical sample, showing atomically resolved interface. b. The hot spot temperatures for the two best thermal conductors (BAs and diamond), as a function of heating sizes from 100 μm to 100 nm for the inset simulation domain, including a 0.8 μm thick GaN layer on the top of a 100 μm thick BAs substrate. All simulations inputs are from experimental measurements and ab initio calculations. The comparison from Fourier's heat conduction law (dashed lines) and spectral-dependent Boltzmann transport equation (solid lines), quantifies the transition from diffusive to ballistic thermal transport (insets). The size-dependent hot spot temperature results, indicate that BAs has a superior performance for nanoscale thermal management, owing to its both high thermal conductivity and thermal boundary conductance.

Figure 5.4b shows the hot spot temperature as a function of the heating sizes (solid line). As

expected, with reducing the heating width from 100 μm to 10 nm, the hot spot temperature increases dramatically due to the increased packing density. We also noticed that the ballistic heat transfer becomes substantial for heat spots of small sizes, so that Fourier's law result deviates significantly from the BTE calculation, i.e., representing the practical heating prediction. When the heating width is large, the result of Fourier's law is consistent with the BTE. But when heating source width is smaller than 1 μm, the hot spot temperature by the BTE is much higher compared with Fourier's law, and such difference between the BTE and Fourier's law increases dramatically with the width decrease of the heating source. Fundamentally, the ballistic transport takes place when the heated spot size is smaller than the mean free paths, and here it occurs for a heating source width on the order of ~ 1 μm, which is consistent with our previous study of phonon mean free paths[195,197,200]. This clearly shows that at the nanoscale, the ballistic transport will significantly increase the overheating issue over classical theory prediction. In addition, the hot spot temperatures are compared between using BAs and diamond as cooling substrates (Figure 5.4b): For the whole range of heating sizes, BAs is superior to diamond for heat dissipation. For example, with a 1 μm heating width, the hot spot temperature increase for BAs is 38% lower than that of diamond. These results demonstrate that the high G value between GaN and BAs (250 MW/m^2K), together with its high thermal conductivity (1300 W/mK), significantly improves heat dissipation, and underscore the promise of using BAs for thermal management in nanoscale electronic devices.

Finally, we carried out device integration with HEMTs and experimentally measured the operating HEMT devices for a comparison of the performances of the BAs, diamond and SiC cooling substrates. To make a fair comparison, the HEMTs were fabricated using the same AlGaN/GaN epitaxial layers and device layout. Figure 5.5a presents an SEM image of our fabricated HEMTs device integrated on top of a BAs substrate. In Fig. 5.5b, we show the hot-spot

temperature rise, while operating the AlGaN/GaN HEMTs, as a function of power density for the different cooling substrates. With the same device layout and operating conditions, the device cooling performance for BAs exceeds that for diamond and SiC, verifying the modelling predictions. For example, at a transistor power density of ~15 W mm−1, the hot-spot temperature rise is ~60 K for GaN–BAs, substantially lower than the temperature rise for GaN– diamond (~110 K) and GaN–SiC (~140 K) devices.

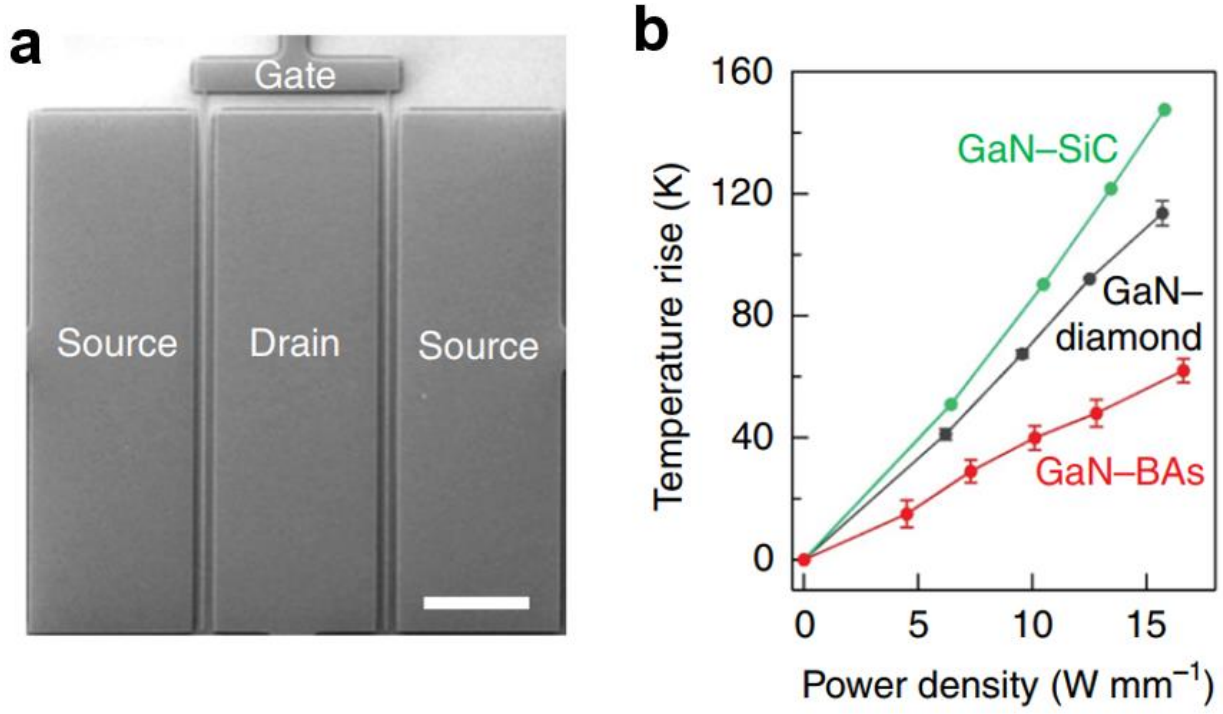

Figure 5.5 Experimental measurements of the hot-spot temperature rise in operating AlGaN/GaN HEMTs as a function of transistor power density, with different cooling substrates (BAs, diamond and SiC). All devices shared the same geometry: two fingers, with a width of 100 μm and gate pitch of 34 μm. An SEM image of the fabricated HEMT device is shown in c (scale bar, 20 μm) and a plot of GaN temperature as a function of power density is shown in d, measured using Raman spectroscopy on the drain side at a lateral distance of 0.5 μm from the T-gate edge, for transistors on a GaN-on-BAs wafer, as well as a reference GaN-on-diamond wafer and GaN-on-SiC wafer. Data for diamond and SiC substrates are adapted from ref. 188.

5.4 Conclusion

In summary, we report the systematic energy transport study across the interface of the emerging HTC materials. We experimentally demonstrated that TBR is significantly improved with BAs and BP in comparison to the state-of-the-art HTC prototype materials. Replacing diamond with BAs, we developed interface integration using metamorphic heteroepitaxy and measured TBR by over 8 times improvement with a typical GaN-interface. In addition, we performed atomistic calculations based on ab initio derived phonon band structures and verified the intrinsic enhancement in interface heat dissipation under varied conditions including Radiation limit, DMM calculation, and MD simulations. Our study revealed that the enhanced TBR with BAs is due to the fundamental semiconducting band structure with a large overlap of phonon density of states and efficient interface phonon transmission. As a further step, through experiments and multiscale modeling, hot spot temperatures of GaN devices integrated with different cooling substrates are examined for both diffusive and ballistic regimes, confirming the high cooling performance of BAs. Together with the ultra-high thermal conductivities and low TBR, these new materials could revolutionize the current technological paradigm of nanoscale thermal management of high-power electronics and possibly extend their roadmap.

CHAPTER 6

Ultralight and Flexible Monolithic Polymer Aerogel

6.1 Introduction

High performance thermal insulation materials are desired for a wide range of applications in cryogenics, space, subsea systems, buildings, and civil, biomedicines, energy and environments[6,110,232,233]. Traditional insulation materials include porous structures such as fiberglass, mineral wool, cellulose, polyurethane and polystyrene foams[234]. Aerogel, most commonly based on silica, is an extremely porous structure artificially formed through the careful drying out of the liquid component inside a gel and leaving a solid filled up almost entirely by air[235]. Despite of its record-low thermal conductivity, the fragility and brittleness of silica aerogel needs to be improved for applications where mechanical strengths are important. Recent progress has been made in developing aerogels involving organic or nanostructured components[236–245] to improve the mechanical properties. However, most synthesis methods usually involve chemical reactions in gel preparation and are limited to specific materials. In addition, the manufacturing cost introduced by delicate processes such as supercritical drying in preparing high-quality aerogels requires high pressure equipment and consumes large amount of liquid carbon diode can pose challenge for large scale deployment.

Here, we report the first systematic study of interfacial integration and nanoscale energy transport across these new HTC semiconductors with prototype metal and semiconductor materials. As demonstrated through ultrafast spectroscopy experiments and atomistic to multi-scale modeling, BAs and BP, with their intrinsic semiconducting nature and phonon band structures, provide a

significant improvement of the thermal boundary conductance and thermal management performance.

6.2 A facile way to synthesize polymer aerogel – using PVC as an example

We developed an ambient synthesis process of PVC aerogel mainly consisting of three steps: gelation, solvent exchange and drying (Figure 6.1a). First, the reaction sources, i.e. PVC powder (389293, Sigma-Aldrich, USA) is mixed with dimethylformamide (DMF) (DX1727, EMD Millipore, Germany) with ratio from 0.2 g/10 mL to 1 g/10 mL at temperature of 60 ^{o}C. The porosity of aerogel is controlled by tuning the concentrations of PVC solutions. Second, the solution is sonicated for an hour and exposed to air for 12 hours, from which the water vapor is absorbed into DMF/PVC solution. Consequently, the solubility of PVC decreases gradually resulting in the precipitation of polymer particles. Finally, a white and jelly-liked PVC solid was formed. To remove the liquid from the PVC gel while avoiding shrinkage of the porous structure, the solvent is exchanged with ethanol, which has a small surface tension. The solvent exchange process includes five steps each with a time interval of 6 hours to gradually increase the volume percentage of ethanol in the solvent from 0%, 25%, 50%, 75%, 87.5% to 93.8%. Following aged for twelve hours, the gel is exposed to ambient environment. After the solvent is completely evaporated, a solid backbone is formed s shown in the optical image (Figure. 6.1b). The volume of aerogel can expand by more than ten times larger than that of the original PVC powder indicating a high porosity is formed and filled with air. Note that this ambient processing approach allows readily preparation of inch-size PVC aerogel samples and further scaling up (Figure. 6.1b).

The microscopic structures of PVC aerogel samples were examined using scanning electron microscope (SEM) as shown in Figure 6.1c. It can be observed that there are enormous PVC particles with diameter from 0.5 to 5 μm connected with each other with necks at the microscale. These PVC particles are initially precipitated during diffusion of water vapor into DMF solvent. While the growth of distributed PVC particles, the dangling polymer chains can entangle with the chains from other particles. Finally, different particles are connected and form a porous network. It was observed that when a small droplet of water was added into the solution, a lot of white PVC particles precipitated but not connected, which proved the critical importance of a natural slow absorption process. It should be noted here this dynamical process of generation of polymer network can happen to other polymers in principle only if the polymers are well dissolved in a certain solvent and precipitated gradually with absorption of insoluble solvent. The effective density ρ_{eff} can be measured based on Archimedes principle, from which the porosity can be directly derived from the comparison with the density of bulk form PVC ($\rho_{PVC} = 1.38\ g/cm^3$) according to the following equation

$$\emptyset = 1 - \frac{\rho_{eff}}{\rho_{PVC}} \qquad (6\text{-}1)$$

As summarized in Figure 6.1d, when the ratio of PVC/DMF varies from 0.02 to 0.10 /mL, the porosity can change from 60.4% to 95.4% continually, with density decreasing from 0.546 to 0.063 g/cm^3. In comparison, such a low mass density of 0.063 g/cm^3 corresponds to a porosity of 97% for silica aerogel, which however usually requires delicate synthesis methods such as supercritical drying or multiple surface modifications[246]. The lightness and flexibility of the synthesized PVC aerogel are further illustrated in Figure 6.1e. As an example, a 3.5 cubic centimeter of the PVC aerogel weighs just 230 miligrams and is so light that it can be balanced on a flower and a blade of foxtail grass (see Figure 6.1e. In addition, the as-synthesized PVC aerogel

can be highly twisted to a rope but without leading to a mechanical breakdown (Figure 6.1f), which is impossible for standard silica-based aerogels. To further explore the potential application in flexible devices, we have performed a compression test and the PVC aerogel shows high robustness and reversibility for bending at large angles of 90 to 180 degree (Figure 6.1g). Such an ultraflexibility remains challenging for other aerogels.

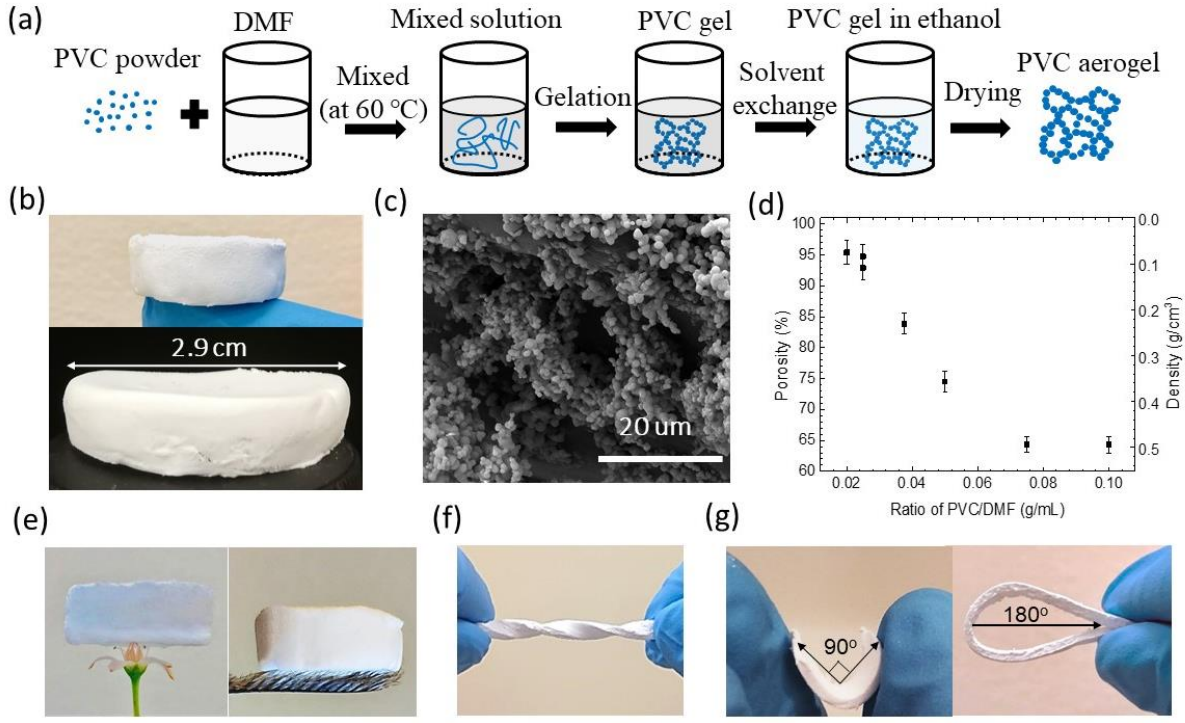

Figure 6.1 Ambient synthesis and characterizations of polyvinyl chloride (PVC) aerogels. (a) Schematic illustrating the ambient synthesis process. (b) Optical image of a typical PVC aerogel sample. (c) Scanning electron microscope (SEM) image of PVC aerogel showing a porous network consisting of PVC particles. (d) The relationship between the porosity of aerogel and the mass ratio of chemical precursors. (e) Ultralight aerogel sample balanced on a flower and a foxtail, (f) the twisting test and (g) bending test of the flexible PVC aerogel.

6.3 Ultralow thermal conductivity of PVC aerogel

Thermal conductivity of PVC aerogels is measured using the hot-wire method[247]. The hot-wire method is a standard technique for measuring a wide range of materials[248–253]. In this method, an electrically resistive metal wire is embedded in the sample, serving as both a line heat source and a temperature sensor, as depicted schematically in Figure 6.2a[254]. A constant current is applied and uniform joule heating is generated along the wire, and the local temperature of the wire is sampled instantly by taking advantage of the linear relationship between temperature and resistance of metal wire. More specifically, in our measurement, a platinum wire with a diameter of 23 μm was placed in the PVC/DMF solution. The platinum wire would be well embedded in the sample while the formation of aerogel. By solving the transient heat conduction model, the temperature rise is found linear with the logarithm value of time and the thermal conductivity can be related with the temperature rise rate by

$$\kappa = \frac{\bar{U}I}{4\pi L}\frac{\Delta \ln(t)}{\Delta T} \qquad (6\text{-}2)$$

where $\bar{U}$, I and L are the average voltage drop, current across the wire and the length of the wire. Figure 6.2b displays two temperature rise curves versus logarithm time of two typical samples prepared with 0.25 g/10mL and 0.5 g/10 mL PVC mass to DMF volume ratio. The applied current is 89 mA and the wire length of 1.56 cm. For a fixed heating power, a larger slope of the measurement curve would indicate a smaller thermal conductivity. By comparing the temperature rise curve versus time with a transient heat conduction model, the thermal conductivity of sample can be precisely derived.

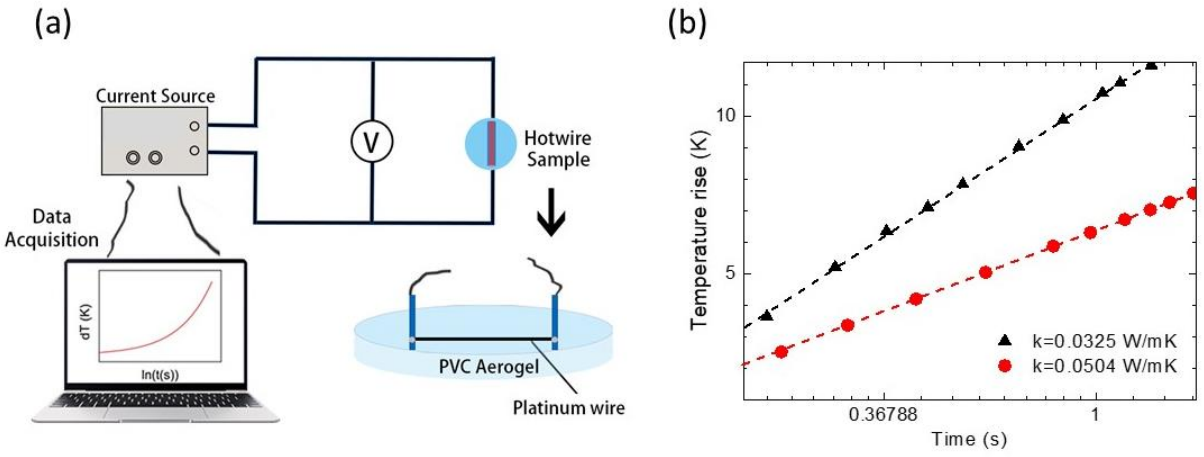

Figure 6.2 Thermal conductivity measurement of PVC aerogels. (a) Schematic of hot-wire thermal conductivity measurement. (b) Typical experimental data (symbols) fitted to the transient heat conduction model (dash lines). Black and red color represents samples prepared with different initial PVC mass to DMF volume ratios, i.e. here respectively 0.025 g/mL and 0.05 g/mL

With such a high porosity and low intrinsic thermal conductivity of bulk PVC around 0.16 W/mK[255], thermal conductivity of the PVC aerogel with a porosity of 95.4% was measured to be as low as 0.028 W/mK, approaching the thermal conductivity of air (~0.026 W/mK)[256], which means our PVC aerogel can act as air-like thermal insulation material. Moreover, evacuation to a mild vacuum of ~ 0.01 atm is sufficient to further suppress the gaseous heat transfer and to achieve a thermal conductivity as low as to 0.0077 W/mK. From the comparison of thermal conductivity in air and under evacuation, we can find the air molecules have dominant effects on thermal transport in PVC aerogel and the heat conduction through the PVC backbone is negligible. Note that there are three different thermal transport pathways inside aerogel as illustrated in Figure.6.3a: heat conduction through the solid backbone, heat conduction via the gas molecules filled in the pores, and thermal radiation from the surface of the backbone. Thus, the total thermal conductivity

of aerogel (κ) can be decomposed into three components: solid thermal conductivity (κ_s), gaseous thermal conductivity (κ_g), and radiative thermal conductivity (κ_r), which can be mathematically expresses as[257]

$$\kappa = \kappa_s + \kappa_g + \kappa_r \qquad (6\text{-}3)$$

From the heat transfer estimation, the radiative thermal conductivity κ_r is less than 0.002 W/mK when porosity is below 95%[257], which is much smaller than the other components. Therefore, the two main contributions to thermal transport in the PVC aerogels are κ_s and κ_g, which are affected mostly by the porosity and pore size. Porosity dependent κ of PVC aerogels were measured and plotted in Figure 6.3b. When samples are measured in air, κ decreases monotonically from 0.0618 to 0.0283 W/mK with porosity from 60.4% to 95.4%, indicating that κ_s contributes to the heat conduction following the volumetric fractions of the solid PVC backbone.

To make a comparison, literature data of silica aerogel from supercritical drying and ambient drying processes[246,258] are also plotted in Figure 6.3b. For the same porosity, the PVC aerogel demonstrates remarkably lower thermal conductivity than silica aerogels prepared from both methods. The PVC samples were also measured in mild vacuum at a pressure around 0.001 atm, and shows a thermal conductivity from 0.0356 to 0.0077 W/mK for the same porosity range. For the sample with porosity of 95.4%, the gaseous contribution κ_g can be calculated from the subtraction of the thermal conductivity value in vacuum from that in air. This calculation gives κ_g to be around 0.0206 W/mK. On the other hand, from the calculation using the porosity and the thermal conductivity of air, κ_g is 0.0245 W/mK, which is 20% higher than the former value. We attribute such a difference in κ_g to the Knudsen effect[236,257,259,260] of air molecules in confined space, i.e. small pores inside the PVC aerogels. This Knudsen effect indicates that if the pore size

is smaller than or comparable with the traveling mean free path of the gas molecules in free space, the gas molecules would collide with the solid framework before their interactive scattering. Such additional scattering with solid framework can effectively lower the mean free path of gas molecules than its intrinsic values in free paths, and thereby reduce thermal conductivity. Further reduction in pore size will lead to stronger Knudsen effect, and thus lower thermal conductivity.

Here, we use the Knudsen effect to analyze the pore size of the PVC aerogel by measuring their pressure dependent thermal conductivity. The pressure dependent thermal conductivity of high porosity aerogel samples is measured from 100 Pa to ambient pressure (Figure 6.3c). Note that among the three heat transfer contributions, κ_r and κ_s are pressure independent, and the decrease of κ with reduced pressure represents the reduction of κ_g. From the kinetic theory, the thermal conductivity of air can be calculated as[261]

$$\kappa_g = A\rho c_V \bar{v} \Lambda \qquad (6\text{-}4)$$

where A is a constant, and $\rho, C_V, \bar{v}$ and Λ are the air density, specific heat, average velocity, and mean free path of molecules respectively. ρ is proportional to the pressure, and Λ is inversely proportional to pressure. Thus, in principle, κ_g in free space should be pressure independent. Contrary from the simplification, κ_g of PVC aerogel from measurement (Figure 6.3c) strongly depends on the ambient pressure because the porous structure limits the air molecules diffusion and breaks the inverse relationship between Λ and the pressure. The Λ of air molecules in a porous structure can be calculated based on Matthiessen's rule[261]

$$\Lambda = \frac{D}{D+\Lambda_0}\Lambda_0 \qquad (6\text{-}5)$$

D is pore size in diameter. Λ_0 is the mean free path of air molecules in free space and is calculated using $\Lambda_0 = \frac{B}{P}$, where P is the pressure in the unit of Pa. Since Λ_0 equals to 66 nm at 1 atm[261], B equals to 0.00663 for air. So the total thermal conductivity at different pressures can be calculated as

$$\kappa = \kappa_s + \kappa_{g,0} \frac{PD}{B+PD} \qquad (6\text{-}6)$$

where $\kappa_{g,0}$ is the gaseous thermal conductivity at 1 atm. κ_s represents the solid state contribution and can be measured at a high pressure (e.g. 100 Pa). From Eqn. (7-6), we can find that when the pore size is smaller, κ_g would be smaller at a fixed pressure. The experimental data with best fitting using Equation (6-6) is shown in Figure 6.3 (c). For a fixed pore diameter, It is clear that κ increases for high pressure since κ_g is increasing. The average pore size was extracted from the modeling fitting with experiment and ranges from 800 nm to 1300 nm. Note that the distribution of pore sizes provides the substantial confinement to the travelling of molecules despite that the average pore size is larger than the mean free path Λ of air molecules at atmosphere pressure,

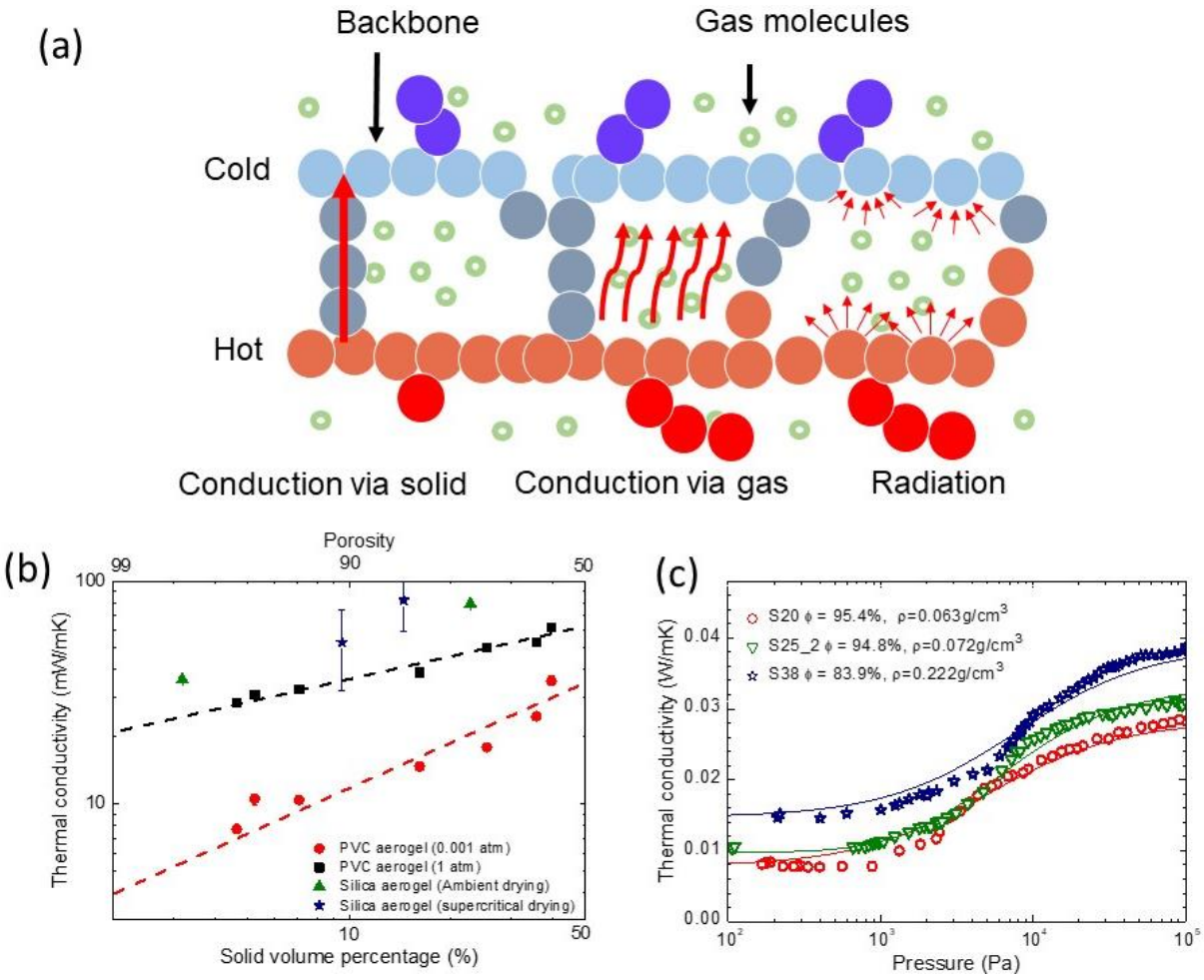

Figure 6.3 Thermal transport analysis in PVC aerogel. (a) Thermal transport pathways inside PVC aerogel, consisting of heat conduction through solid backbone, heat conduction via gas molecules, and thermal radiation from surface of backbone. (b) Porosity dependent thermal conductivity of PVC aerogel in air and at 0.01 atm. Literature data [18, 30] on thermal conductivity of silica aerogel obtained from supercritical drying and ambient drying are included for comparison. The guidelines are power law fitting of experimental data to illustrate the porosity-thermal conductivity relationship. (c) Pressure dependent thermal conductivity of PVC aerogel with different porosities and mass densities. The red, green and blue color represents the PVC aerogel with a porosity of 95.4%, 94.8 and 83.9%, respectively. The symbols are for experimental data and the lines are for best fittings.

6.4 Superhydrophobicity of PVC aerogel

Next, we explore the superhydrophobicity of the PVC aerogel. The hydrophobic property of a material is determined by the wettability of surface (i.e., the interaction with water). When the Young contact angle on a surface is over 150°, they are defined as superhydrophobic materials[262–265]. Superhydrophobicity can be extremely beneficial for various potential applications[266]. For instance, in building materials involving water-resistance or absorption of hydrophobic substances such as oil[267]. However, classic materials such as silica tend to shrink and cloud in humid environments, and therefore destroy its transparency and integrity. Superphydrophobic surfaces are intensively investigated and specially formulated to repel water and not absorb moisture from the air[268,269]. Here, we performed contact angle measurement and reveals that supershydrophobic PVC aerogels can be achieved at a high porosity. The contact angle of PVC aerogel samples with water are summarized in Table. 1 with the other properties. In comparison, the contact angel of bulk PVC with water of is ~ 87º, which indicates a slightly hydrophilic material. Notably, the aerogels samples with porosity higher than 85% have the contact angle over 150º. The tested contact angle is as high as to 160.2º when the porosity increases to 95%, implying a superhydrophobic material. To evaluate the structural stability, these samples were re-measured after being kept in ambient environment for more than a month and still sustain the superhydrophobicity.

Table 6. 1. Properties of PVC aerogels prepared with different porosities**.**

Sample	PVC (g)	DMF (ml)	Porosity	Mass density (g/cm^3)	Thermal conductivity in air (mW/m·K)	Thermal conductivity at 0.01 atm (mW/m·K)	Contact angle with water (deg)
S20	0.20	10	95.4%	0.063	28.3	7.7	160.2
S25_1	0.25	10	92.9%	0.098	32.6	10.4	158.1
S25_2	0.25	10	94.8%	0.071	30.9	10.5	158.0
S38	0.38	10	83.9%	0.222	38.9	14.7	147.3
S50	0.50	10	74.5%	0.352	50.4	17.9	131.1
S75	0.75	10	64.3%	0.493	53.1	24.7	101.4
S100	1.00	10	60.4%	0.546	61.8	35.6	97.7

We attribute the micro-pores near the PVC aerogel surface as the main reason for the observed superhydrophobicity, as illustrated in Figure 6.4a. These surface porosity can serve as roughness on a flat surface and create hydrophobic materials[270]. Cassie and Baxter put forward an analytical model for porous solid surface in which no water is filled[270]

$$\cos\theta_c = f \cdot \left(\cos\theta_{c,0} + 1\right) - 1 \qquad (6\text{-}7)$$

where θ_c, $\theta_{c,0}$, f are respectively the contact angle between porous surface and water, the contact angle between dense surface and water, and the fraction of solid on the surface. Since the PVC itself is weakly hydrophilic, some space of the pores near the surface would be filled. The wetting status would be a mixed state of Wenzel state and Cassie-Baxter models. For the mixed state, the contact angle can be calculated by combining Eqn. (6-7) and Wenzel model[271]

$$\cos\theta_c = f \cdot \left(r \cdot \cos\theta_{c,0} + 1\right) - 1 \quad (6\text{-}8)$$

where r is the roughness factor, defined as the ratio of the actual wetted area to the projected area on the surface[272]. In Figure 6.4b, the predicted contact angles for aerogel with different porosities are plotted together with the experimental data, where the porosities was obtained from the pressure-dependent measurement in Figure 6.3 and taken to determine the solid fraction near the surface. The experimental measurement of contact angles are plotted together with the calculation in Figure 6.4b, and shows good agreement, indicating that the high porosity of PVC aerogel increases gas-solid interface areas and enhances the surface roughness, which together leads to the superhydrophobicity. The observed superhydrophobicity in the PVC aerogels synthesized by this facile ambient process can enable new opportunities in designing water-repelling building blocks, surface engineering, and drug delivery platforms[273–276].

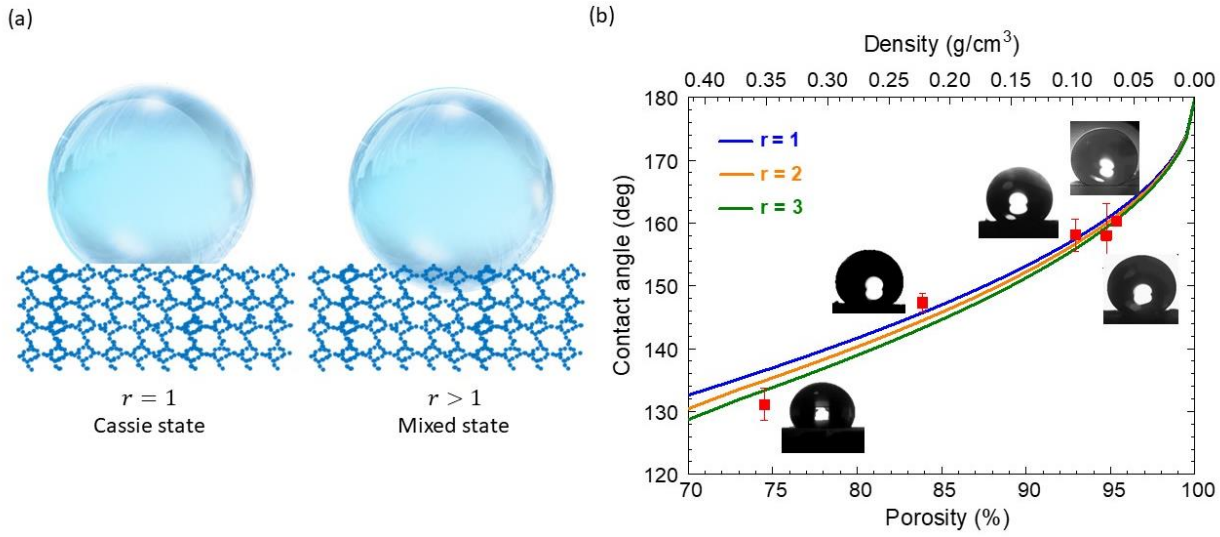

Figure 6.4 Contact angel measurement and superhydrophobicity of PVC aerogels. (a) Schematic illustrating the mechanism how the surface porosity improves the surface area and the contact angle with water. (b) The porosity dependent contact angle of PVC aerogel, following the prediction based on Cassie-Baxter model (blue) and Wenzel model (Orange and Green). r is the r oughness factor, defined as the ratio of the actual wetted area to the projected area on the surface.

6.5 Conclusion

In summary, we develop a facile method to synthesize ultralight and flexible polymer aerogel with low thermal conductivity without supercritical drying. We successfully prepared PVC aerogels with the porosities ranging from 60% to 95% and measured the thermal conductivity of the PVC aerogel as 28 mW/mK in air and 7.7 mW/mK under mild evacuation. The contribution from air conduction dominates the thermal transport in PVC aerogel. Our modeling analysis indicates that the lower boundary of thermal conductivity can be pushed by further reducing the pore size and increase the porosity. In addition, we measured the contact angle of PVC aerogel with water and found that the PVC aerogels with porosity larger than 85% are superhydrophobic. The porosity-dependent contact angles from experimental measurement are in good consistence with theory prediction by mixed Cassie-Baxter and Wenzel models. The low thermal conductivity, mechanical flexibility and superhydrophobicity show high promise in engineering the PVC aerogel for thermal insulation applications under different working environments.

CHAPTER 7

Flexible Tin Selenide Nanosheet Films for Thermoelectric Energy Conversion

7.1 Introduction

The growing demand for energy continues to represent a dichotomy in the struggle against increasing greenhouse gas emissions. In this endeavor, research has shown that over 15 quadrillion Joules of this energy is lost as waste heat, and among which, 80% of the waste heat is lower grade, i.e. below 400 K. Despite that various approaches including traditional steam cycles, Kalina cycles, and organic Rankine cycles have already been implemented in various industries for mid- to high-grade waste heat recovery, resulting in millions of saved dollars over long-term operation, such efforts are not yet economical for lower grade waste heat[277]. In addition, most current approaches are limited to recovering waste heat from hot-water based systems, while the opportunities and requirements for wide-spread recovery of lower grade waste heat can be highly specific based on the industry of interest. Despite that a variety of novel solutions rooted in nanotechnology have been emerging in literature, such efforts continue to be primarily limited in applicability due to low efficiencies far below the thermodynamic limit.

On the other hand, thermoelectrics, a solid-state technology that directly converts between heat and electricity attracted decades of investigations and has been matured for applications in radioisotope thermoelectric generators and Peltier coolers. The benefits of using thermoelectric materials manifest in their reliability, low-maintenance, and no moving parts, but have thus far been limited from lower grade waste heat recovery applications due primarily to their low energy efficiency[278]. Recent efforts have focused on and succeeded in improving thermoelectric energy

efficiency and identifying new records of thermoelectric materials. However, the peak performance and associated temperature range of operation for most thermoelectric materials such as SiGe[279], PbTe[280], Clathrates[281], skutterudites[282], CuSe[283], and Cu_2S are currently focused on high temperature applications[284], and retain limited efficiency at low temperatures, below 400 K. The efficiency of these materials indeed benefits with increased temperature, as defined through the thermoelectric material figure of merit, $ZT = \frac{\sigma S^2}{\kappa} T$, where σ is the electrical conductivity, S is the Seebeck coefficient, κ is the thermal conductivity, and T is the average absolute temperature. The state of the art room temperature thermoelectric materials remain to be alloys of expensive bismuth telluride[284] ($Bi_{0.5}Sb_{1.5}Te_3$ with $ZT = 1.86 \pm 0.15$ at 320 K), which continue to benefit from and improve in performance with the development of new techniques to modify and enhance the properties of the compound as needed, such as through solid-solution alloying, porosity control, band engineering, topological states, resonance states, and hierarchical micro- and nano-structuring[285]. While commercialization of thermoelectric materials and devices in the waste heat recovery market is expected to rapidly expand with a material *ZT* around 2 – 3 (~10 – 15 % Carnot efficiency) at room temperature, these values have previously only been accessible in lab-environments or at high temperatures. New materials and geometries have emerged that may rival these compounds in terms of both cost and performance, including tin selenide (SnSe) with a record high *ZT* of 2.6 at 923 K in the *Cmcm* structural phase[286].

This record thermoelectric performance has excited the field to try to understand its origin, and has led to a vast number of investigations that document its synthesis, characteristics, and applications. Moreover, SnSe has the highest reported device *ZT* from 300 to 773 K at ~ 1.34[287]. Extensive efforts have begun to explore ways to tune doping to modulate and improve the performance of SnSe, including via the carrier concentration, and boundary scattering phenomena

(nanostructuring), that can lower the thermal conductivity and maintain sufficient electrical conductivity. Structural control of SnSe has led to dramatic performance improvement and record-high efficiency, however, exploration of this new material for lower grade temperatures still lacks study.

7.2 Material synthesis and characterizations

Here, we report high performance solution-processable flexible SnSe nanosheet stacks in a packed bed structure for lower grade waste heat recovery. The nanostructured SnSe in the morphology of two-dimensional sheets are prepared using a readily scalable hydrothermal synthesis temperature difference method. A record-high energy efficiency with ZT ~ 2.2 was measured at room temperature. The significant improvement over its bulk form is attributed to the largely reduced thermal conductivity due to interface phonon scattering. Furthermore, to evaluate the functional flexibility, SnSe samples are coated as a thin film on a flexible polyethylene terephthalate substrate with a bending test performed over 1000 cycles, showing highly stable performance for flexible energy harvesting devices.

We synthesized SnSe to achieve the structural form of two-dimensional nanosheets using a surfactant-free hydrothermal synthesis method. In this method, nutrients in a sealed, hydrothermal autoclave reactor are dissolved in water-miscible solvents that are heated for reaction. As detailed in Figure 7.1a, $SnCl_2 \cdot 2H_2O$ and NaOH are successively dissolved via sonication in a 50 mL beaker filled with DI water using 10 minute sonication increments. By placing the reaction mixture on a preheated hot plate at 473 K for 5 hours at 400 RPM, the high temperature and pressure thermodynamic conditions create a slurry of ions conducive for the reduction of the Se to Se^{-2} and oxidation of some of Sn^{+2} to Sn^{4+}, from which SnSe nanosheet crystals can begin to

nucleate and grow in a process (Figure 7.1a). Note that the growth condition is designed to achieve a 2D surface morphology. Considering the Law of Bravais, the morphology of the grown SnSe can be controlled by carefully selecting precursors and their concentrations to avoid suppression of the {001} and {010} higher surface energy planes in SnSe. In comparison, by utilizing a reaction pathway incorporating oleylamine surfactant, the [100] direction is only weakly suppressed to allow for growth of nanoflowers, versus in this paper where the growth along the [100] direction is strongly suppressed. Here, a 2D morphology of SnSe enhances surface contact areas and provides strong interfacial scattering events, from which a significant effect on the energy transport properties is expected. In the final reaction steps, the mixture is allowed to slowly return to ambient conditions under continued stirring to ensure limited particle aggregation as the newly synthesized particles precipitate out of the solution. The products are washed and collected using a decanting and gravitational sedimentation process that can capture the crystalline SnSe nanosheets. Finally, the nanosheets are re-dispersed into a suspension using DI water, sonication, and vortex mixing before drop casting solutions; further details on the reaction and sample preparation are presented in the supporting information. Single SnSe nanosheets are carefully characterized using atomic force microscopy (AFM) (Figure 7.1b), showing a lateral dimension of about 3 μm and a thickness of about 150 nm.

Next, thin film of SnSe samples are prepared via drop casting for further characterizations. The crystalline structure of SnSe is determined by X-ray diffraction (XRD) shown in Figure 7.1c and confirmed to be orthorhombic *Pmna* space group 62 phase, whose crystal structure is illustrated in the inset of Figure 7.1c. Note that the solution processing method allows scaling nanomaterials for macroscopic device applications. As demonstrated in Figure 7.1d, a thin film of SnSe nanosheets was uniformly deposited using drop casting onto a copper tape substrate over an

area of 1 cm^2. A cross section SEM of the sample details the high density of this packed bed structure, which is critical for thermoelectric transport.

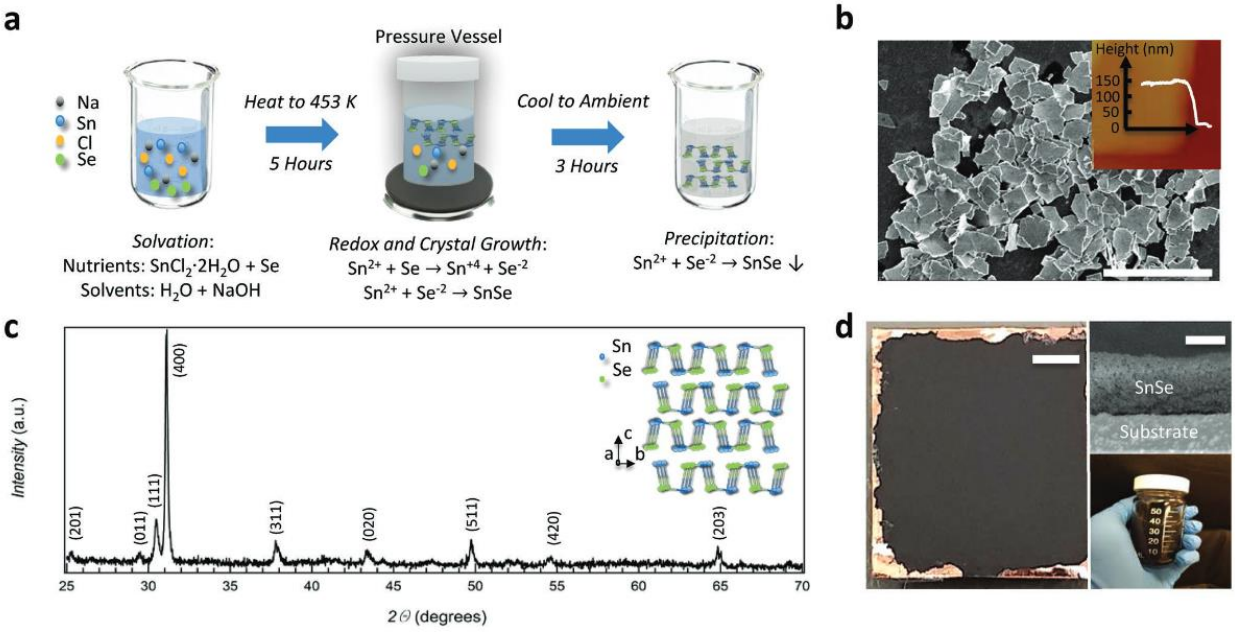

Figure 7.1 Chemical synthesis and structural characterization of tin selenide nanosheet stacks. (a) Hydrothermal synthesis of tin selenide (SnSe) nanosheets using the hydrothermal method. (b) Scanning electron microscopy (SEM) of as-synthesized SnSe nanomaterials, verifying it's in the form of nanosheets. The scale bar is 10 μm. Inset, atomic force microscopy (AFM) image showing the thickness of single SnSe nanosheet of about 100 nm. (c) Powder X-ray diffraction (XRD) for SnSe with inset indicates its van der Waals crystal structure. (d) Optical image of scaling up SnSe thin film, with the scale bar of 5 mm. The packed bed structure of the SnSe film is obtained from the scalable solution process (bottom right) and its cross-section is studied by SEM (top right with the scale bar of 50 μm).

7.3 Thermoelectric properties measurement

To evaluate the potential for lower grade waste heat harvesting, the thermoelectric properties of the SnSe thin film were measured near room temperature. The temperature gradient versus voltage gradient data are plotted in Figure 7.2a, indicating a p-type behavior of the SnSe film. Seebeck coefficient are measured for 300 – 400 K shown in Figure 7.2b, with room temperature value S = 1625 $\pm$ 94 μV/K. As a control experiment, we also simultaneously measured bulk SnSe single crystal samples synthesized by chemical vapor deposition and obtained a Seebeck coefficient of $809 \pm 55\ \mu V/K$, consistent with literature[32]. Note that the measured near-room temperature Seebeck of SnSe nanosheet films represents twice improvement over bulk single crystal SnSe, which was attributed to a possible carrier filtering effect from the high density of interfaces and low electrical conductivity as previously reported in SnSe nanostructures[32]. Next, standard electrical transport measurements performed across the SnSe nanosheet thin film. A linear I-V curve is measured in Figure 7.2c, indicating the Ohmic contact and an electrical conductivity of ~2.4 S/cm at 300 K. Figure 7.2d plots the temperature-dependent electrical conductivity, which exhibits semiconductor transport behavior: the conductivity decreases as temperature increases due to increased phonon scattering, and is consistent with undoped bulk SnSe[28]. Note that the measured electrical conductivity of our SnSe nanosheet film is about 4.5 times lower than the single-crystal form[26]. This reduced electrical conductivity is verified and expected as a compromise from the boundary scattering of electrons at the grain interfaces between the stacked nanosheets.

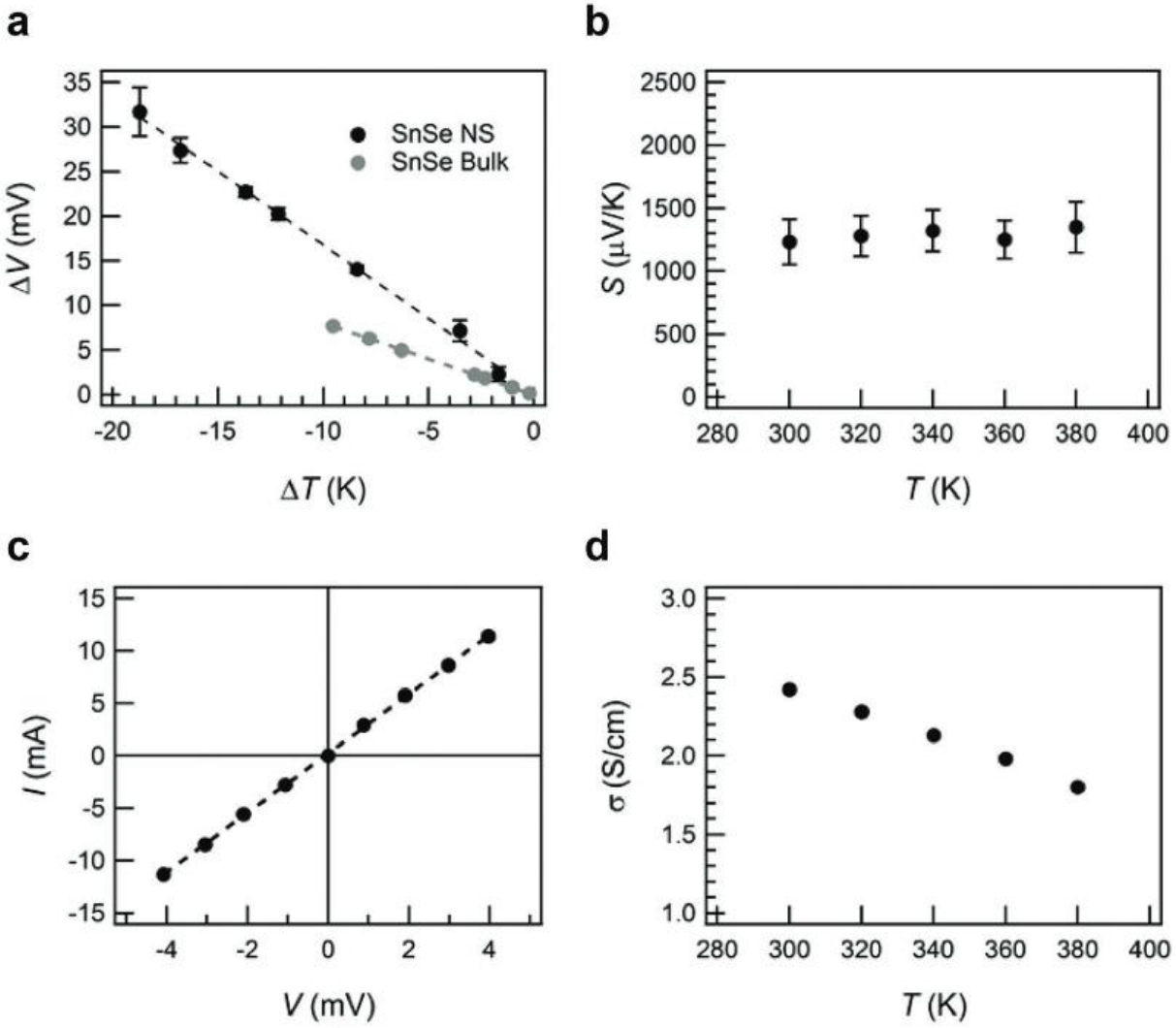

Figure 7.2 Seebeck and electrical characterization of the tin selenide thin film. (a) Seebeck coefficient determination of tin selenide (SnSe) from 300 to 400 K, including nanosheets (NS, black) and bulk SnSe (gray) for comparison. (b) Temperature-dependent Seebeck coefficient. (c) Current-voltae transport curve. (d) Temperature-dependent electrical conductivity

The thermal conductivity of SnSe thin film is measured using the hot-wire method[288]. The hot-wire method is a standard technique for measuring a wide range of materials[289,290]. In this method, a platinum wire is embedded in the SnSe powder, serving as both a line heat source and a temperature sensor, as depicted schematically in Figure 3a. After applying a constant current, uniform joule heating is generated along the wire. Using an infinitely large boundary condition and line heat source, the following heat conduction differential equation can be solved:[253]

$$\mathrm{T(r,t)} = \frac{P}{4\pi kL}\left[\ln\left(\frac{4\alpha t}{r^2}\right) - \gamma\right] \qquad (7\text{-}1)$$

where P is the Joule heating power, κ thermal conductivity, L length of the hot wire, α thermal diffusivity, t time, r the distance between wire center and interested point, and γ higher order terms regarding t and r, which can be neglected in our experiment. Thus, the thermal conductivity of the sample can be calculated from the slope of temperature rise versus the logarithmic value of time:

$$\kappa = \frac{P}{4\pi L \cdot slope} \qquad (7\text{-}2)$$

In our experiment, the temperature rise versus the logarithmic value of time is plotted in Figure 7.3b, and the temperature-dependent thermal conductivity is plotted in Figure 7.3c. While the thermal conductivity of single crystals is expected to decrease with an increase in temperature around room temperature, the thermal conductivity of SnSe films shows slight increase and indicates that the interface boundary thermal conductance dominates the phonon transport in the nanostructures. Indeed, our experiment measures a very low cross-plane thermal conductivity $\kappa = 0.088 \pm 0.004\ \mathrm{W/mK}$ for piled SnSe nanosheets at room temperature (Figure 7.3c), which is approximately seven times smaller than the intrinsic bulk thermal conductivity of single crystal SnSe.

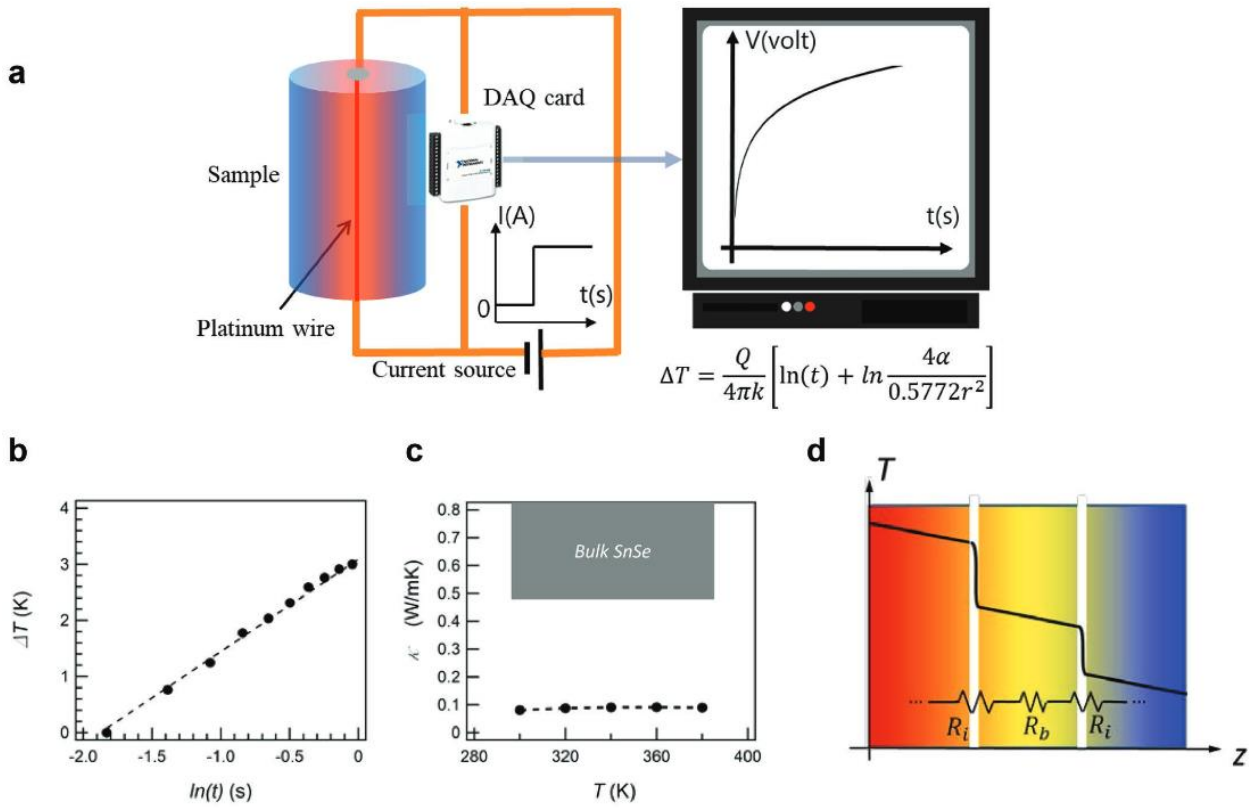

Figure 7.3 Thermal transport measurement and modeling of the tin selenide thin film. (a) Schematic for hot-wire measurement. (b) Typical measurement data and model fitting that determines the thermal conductivity. (c) Temperature-dependent thermal conductivity, in comparison with bulk SnSe crystals. (d) Schematic illustrating thermal boundary resistance and reduced effective thermal conductivity due to strong phonon scattering at the interfaces of SnSe nanosheets.

We attribute such an ultralow thermal conductivity to the thermally resistive interfaces between nanosheets. In the thin film samples, individual SnSe nanosheets are piled together and form multiple interfaces which are expected to dominate the thermal resistance. To verify this expectation, a simplified multi-layer model is built to estimate the interface thermal resistance R_i. The total thermal resistance through the entire material consists of two components: one is resistance due to the interface, and the other is resistance due to the intrinsic SnSe inside each

individual nanosheet, i.e. the bulk crystal resistance. For *n* layers of SnSe nanosheets with thickness at *t* for each layer, then the total thermal resistance R_{tot} through the whole material should be:

$$R_{tot} = n\frac{t}{\kappa_{exp}} = n\frac{t}{\kappa_{bulk}} + nR_i \qquad (7\text{-}3)$$

where κ_{bulk} and κ_{exp} are the thermal conductivity of the bulk single-crystal SnSe and the thermal conductivity of SnSe nanosheet measured by our experiment, respectively. The thickness of our SnSe nanosheet is estimated to be 100 nm for this calculation. Based on Eqn. [7-3], the interface thermal resistance $R_i = 1.1 \times 10^{-6}\, m^2K/W$. In comparison, the bulk thermal resistance is $3.3\times10^{-7}\, m^2K/W$, more than 3 times smaller than R_i.

Hence, this large thermal boundary resistance dominates the overall contribution to the thermal conductivity of SnSe thin films. As illustrated in Figure 7.3d, the large thermal boundary resistance in the system leads to a large temperature drop at the interfaces and strong energy filter effects as expected. As a result of the largely reduced thermal conductivity, the SnSe nanosheet film provides a record-high *ZT* = 2.2 near 300 K. Such a high room-temperature *ZT* has only been observed previously in quantum confinement structures such atomically thin Bi_2Te_3[291] and interface engineered bulk p-type $Bi_{0.5}Sb_{1.5}Te_3$ alloy[292].

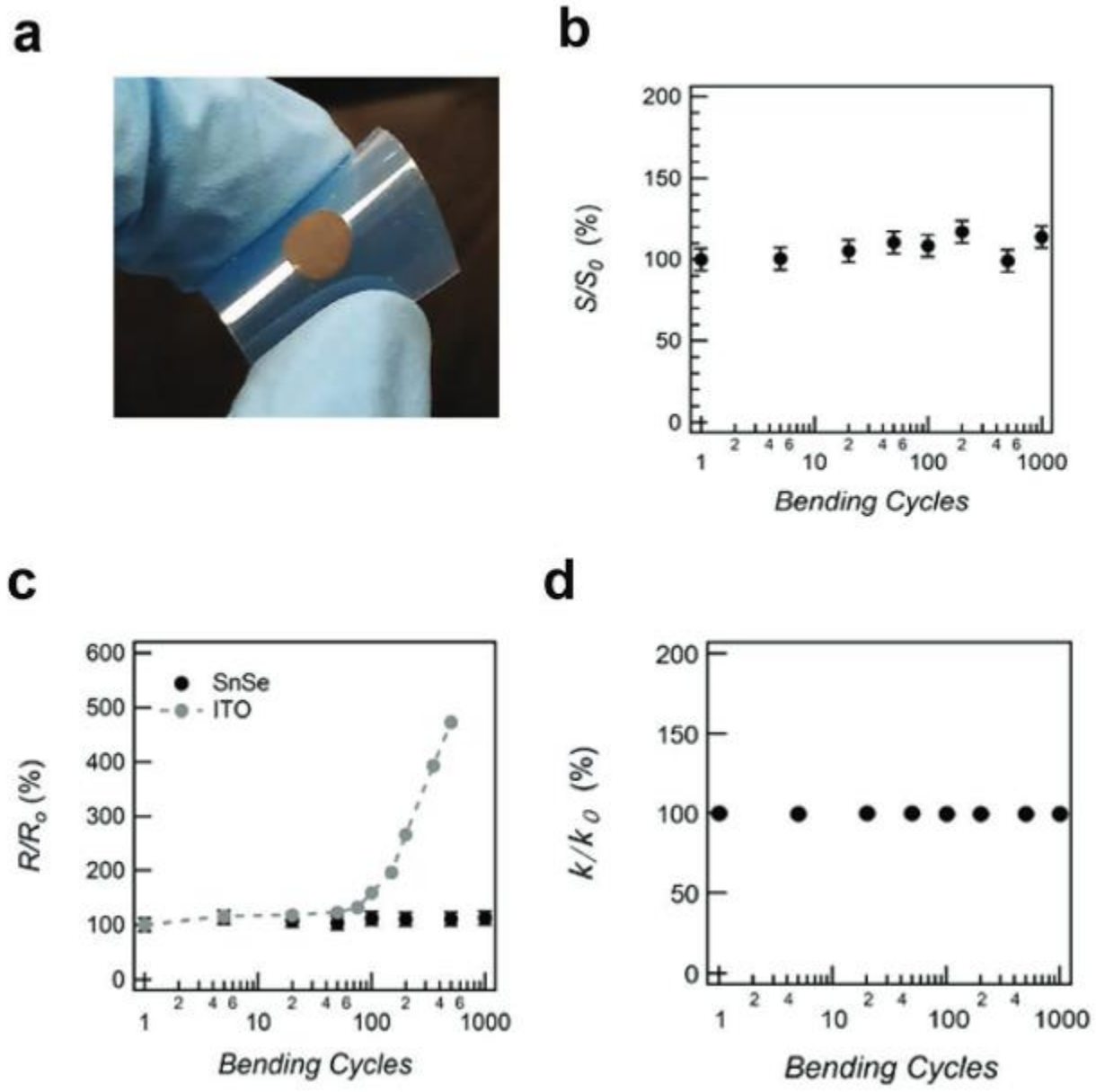

Figure 7.4 Thermoelectric performance of SnSe thin film on flexible substrate. (a) Photograhy of the SnSe fhin film coated on a polyethylene terephthalate substrate under mechanical bending. (b) Room-temperature Relative change of the Seebeck coefficient S, (c) electrical resistance R, and (d) thermal conductivity κ of the thin film in response to the cyclic bending. (e) The thermoelectric figure of merit (*ZT*) in response to bending cycles.

As a further step, we fabricated the SnSe film on a flexible substrate and evaluated its promise as a building block for flexible energy harvesting devices. In Figure 7.4a, the SnSe is deposited on a polyethylene terephthalate substrate to demonstrate preserved functional material properties after being subjected to cyclic mechanical bending of the sample around a 4.5 mm radius of curvature surface. The bending cycle dependent Seebeck coefficient, electrical resistance, and thermal conductivity are plotted respectively in Figure 7.4b-d. As a control in Figure 7.4c, and to better reference the severity of the prescribed bending regime, an ITO film was bending in the same configuration and its cycle dependent electrical resistance is measured for comparison. The ITO film begins to degrade dramatically between 100 to 1000 bending cycles, resulting in a five times increase in resistance. In contrast, the Seebeck coefficient, electrical resistance, and thermal conductivity of our SnSe sample maintain stable over 1000 bending cycles with a maximum fluctuation within 7%, 6%, and 5% respectively. Finally, the bending cycle dependent *ZT* remains around 2.2 for over 1000 cycles, as plotted in Figure 7.4e. The retention of the high performance thermoelectric performance after mechanical bending underscore the promise of using SnSe nanostructures for powering flexible electronics and sensors on curved heating surfaces.

7.4 Conclusion

In summary, we have reported a high-performance thermoelectric thin film fabricated from a low-cost and scalable solution process for lower grade waste heat harvesting. The resulted SnSe nanosheet stacks introduces strong interface phonon scattering and exhibits an ultralow thermal conductivity of 0.09 W/mK at room temperature, which are significantly lower than values of other polycrystalline forms reported in literature. The resulting figure of merit $ZT \sim 2.2$ represents the highest for room-temperature thermoelectric materials reported to date. Moreover,

the SnSe thin film coated on plastic substrate shows a superior flexibility and stability for integration with flexible electronics applications. The low-cost and scalable fabrication routes, together with the demonstrated high thermoelectric performance achieved in relatively earth-abundant materials, represents an important step in harvesting low-grader waste heat and powering flexible electronic devices.

CHAPTER 8

Structurally Tunable Thermal Conductivity in Mesoporous Silica

8.1 Introduction

Manipulating thermal properties of materials through dedicated design of their nanoscale architecture has been successfully demonstrated in various materials for different applications.[293–295] During the last two decades, thanks to the improved synthesis controllability of the structure and hence the tunability of properties, mesoporous silica has attracted intense attention in various fields, including but not limited to drug delivery systems, manipulation of ions and fluid transport in nanochannels, low dielectric constant medium in electronics and nanofluidic energy harvesting system.[296–299] For most of these applications, thermal property is a significant metric to evaluate the material eligibility to achieve the desired system performance. For instance, a sensitive temperature-based stimuli-responsive drug delivery system and electronic systems with efficient heat dissipation requires high thermal conductivity.[30,300,301] On the other hand, low thermal conductivity is of paramount importance for thermal insulation and energy harvesting purpose.[302] Therefore, a good understanding of the relationship between thermal transport property and nanostructure of mesoporous silica, i.e. the porosity, pore size, and/or pore shape could enable dedicated design of these materials toward desired thermal conductivity and application.

However, thermal transport in porous media has never been a trivial problem, not only because of the complicated porous structures but also due to the unclear heat carrier transport process, especially in amorphous solid. There exist numerous models designed for predicting the effective thermal conductivity of porous materials. Most of them are based on effective medium

approximations (EMAs), which estimate the effective thermal conductivity as some functions of the volume fractions and thermal conductivities of the solid and fluid phases ranging from the simple series model, parallel model, dilute particle model and dilute fluid model to the more complicated Maxwell-Garnett model and Bruggeman model.[30,303–305] However, most of the models do not consider the specific porous structures, i.e., the porosity is the only factor considered. Although some attempts were made to include more structural effects into certain fitting parameters, it is challenging to relate them with some measurable physical observables.[303,306] In addition, when only one solid phase and vacuum void phase are present, most of the models show an unreasonably simple linear relationship between effective thermal conductivity and volume fraction of solid phase. From a microscopic perspective, none of these models takes into account the structural effects on the vibrational modes although it has been recognized that micropores have significant effects on those of crystalline materials, e.g. silicon[307–309]. One of the reasons is the severe lack of knowledge about vibrational modes properties in amorphous media. For a long time, mean free path of vibrational modes in amorphous solid was believed to be on the order of interatomic distance.[310,311] Recently, some numerical and experimental studies have revealed much longer mean free path in amorphous silicon and silica, on the order of nanometers.[312–314] This suggests ballistic transport of heat carriers may exist in mesoporous silica. All these findings highlight the need for (i) a careful study of the heat transport in nanostructured silica and (ii) revised thermal conductivity models that consider more details of the porous structure and the effects of domain confinement on vibrational modes.

In this paper, mesoporous silica with different nanoarchitectures, porosities, and pore sizes are synthesized and characterized and their effective thermal conductivity was measured to investigate the structurally modulated thermal properties. Three distinct thermal models were constructed

based on the structural characterization of the three types of materials. Vibrational modes confinement due to the nanoscale pores were discovered to be partially responsible for the unique porosity-dependent thermal conductivity observed. The consistence among the thermal models, Boltzmann transport equation (BTE) calculations, and the experimental observations of the effects of pore size on effective thermal conductivity further confirmed our understanding of thermal transport in mesoporous amorphous solid.

8.2 Material synthesis and characterizations

Here, the nanostructures of mesoporous silica was controlled by using previously reported synthesis approaches.[315–318] As shown in Figure 8.1(a), three different nanoarchitectures were achieved through (i) sol-gel derived mesoporous silica monoliths (silica ambigels or AM), sol-gel evaporation induced self-assembly of block-copolymers - used as structure directing agents - (ii) in silica precursors (SG) or (iii) in a colloidal suspension of silica nanoparticles (NP). More details regarding the synthesis can be found elsewhere and need not be repeated.[317]

In brief, the AM samples were prepared by mixing TEOS, EtOH, deionized water, formamide, and HCl (37 wt% in water, Sigma-Aldrich, St. Louis, MO, USA) with variable molar ratio to control the final porosity. The resulting solution was transferred into a plastic mold for gelation, followed by aging at room temperature. The aqueous solution was exchanged with acetone six times, and then acetone was exchanged with cyclohexane six times at room temperature and atmospheric pressure. The gel was then dried in a cyclohexane-rich atmosphere at room temperature for a week. Finally, the gel was calcined in a box furnace in static air at 500 ^{o}C to remove all traces of solvents and organic phase.

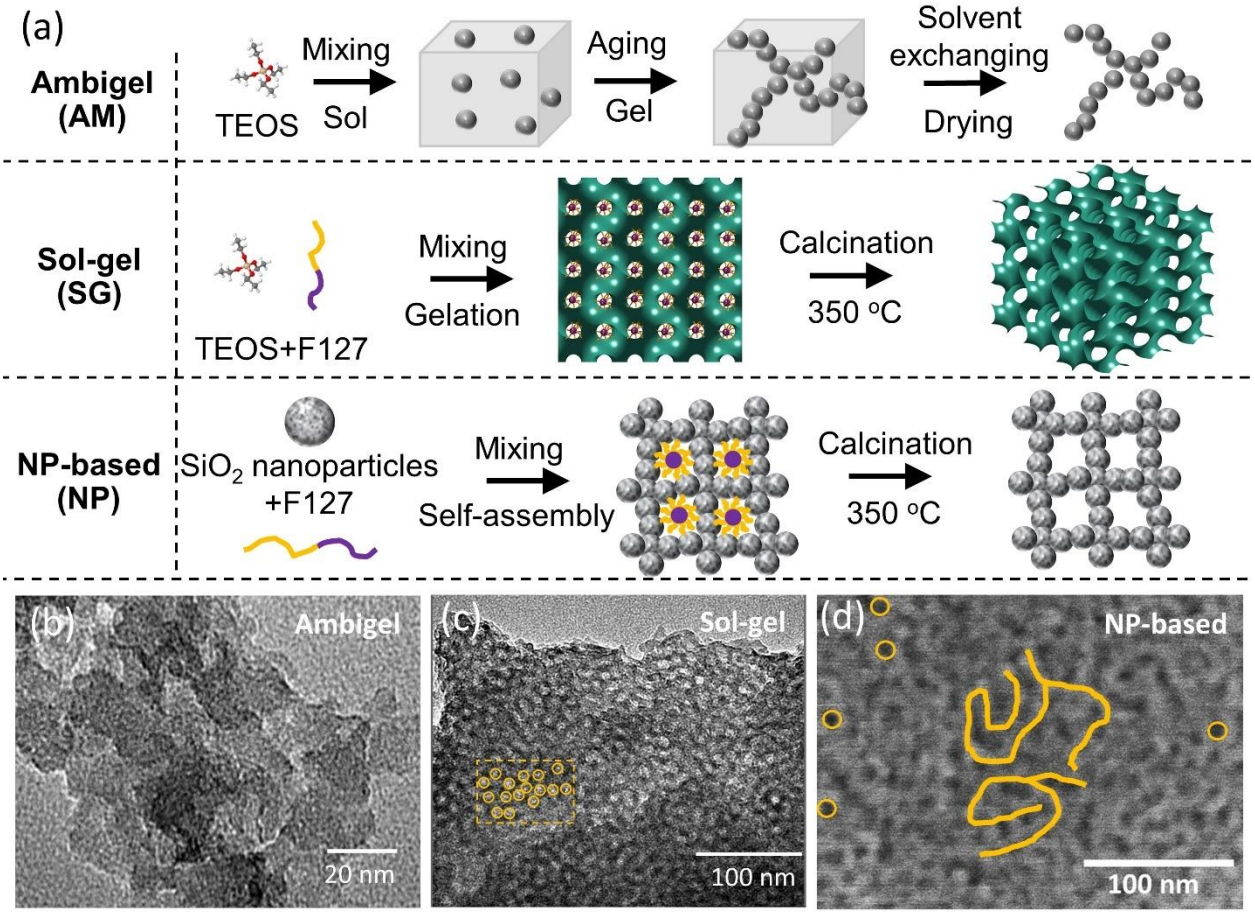

Figure 8.1 Schematic of synthesis and structural characterization of mesoporous SiO_2 film. a). The synthesis processes of mesoporous SiO_2 ambigel (AM), sol-gel-based mesoporous SiO_2 (SG), and nanoparticle-based mesoporous SiO_2 (NP). (b) and (c) Two typical TEM images of the AM sample with nanosized building blocks and the SG with ordered pores. (d) A typical SEM image of the NP sample with chain-like network and spherical pores.

For the synthesis of SG samples, a silica sol-gel solution was made using a mixture of triblock copolymer Pluronic F127 ($EO_{100}PO_{65}EO_{100}$, Mw = 12600, BASF), EtOH, 0.05 M HCl and silica precursor tetraethyl orthosilicate (TEOS). A solution was prepared by dissolving 25 mg F127 in 0.6 mL EtOH, 0.16 mL 0.05 M HCl and a certain amount of TEOS. The final porosity was tuned by controlling the polymer to silica (mass) ratio in the range of 0.1 to 3. Then, the films were spin-coated onto Si substrate and calcined at 350 °C in air for 30 minutes to remove the polymer.

For the synthesis of NP samples, a stock solution of polymer was made by mixing 0.678 g Pluronic F127 with 3 mL DI water. The final porosity was also controlled by tuning the mass ratio of polymer to silica nanoparticle solution (15 wt%, Nalco 2326, ammonia-stabilized colloidal silica, d = 5 nm, Nalco Chemical Company) in the range of 0.1 to 3. Then, the films were spin-coated onto Si substrates. Dried films were calcined at 350 °C in air for 30 minutes to remove the polymer.

Different nanoarchitectures resulted from the synthesis control are verified by structural characterization. First, Figure 8.1(b) shows the transmission electron microscope (TEM) image of the porous structure of a typical AM sample. The solid framework consisted of silica nanoparticles with irregular shape and diameter around 10 nm as building blocks. This silica particle network structure was also confirmed with supercritical-drying leading to silica aerogel.[319,320] Figure 8.1(c) shows TEM image of the porous structure of a typical SG sample. The spherical pores were orderly arranged in the silica matrix, due to the removal of the uniformly distributed and monodisperse polymer templates upon calcination. After measuring the low-temperature nitrogen adsorption-desorption isotherms at –196 °C using a surface area and porosity analyzers ASAP 2010 and

TriStar II 3020 (Micromeritics Instrument Corp., Norcross, GA, USA), the average pore diameter was calculated based on the pore size distribution determined using the Kruk–Jaroniec–Sayari (KJS) method[321] based on the Barrett–Joyner–Halenda (BJH) method[322]. The pore diameter of SG samples varied from 4 nm to 18 nm and average value is 10 nm.

The porous structure of NP is more complicated than both AM and SG samples. On the one hand, like AM samples, the NP samples were built with silica nanoparticles. On the other hand, the templating polymers created additional spherical void space in the particulate system. Figure 8.1(d) shows a typical scanning electron microscope (SEM) image of an NP sample featuring spherical pores with diameter around 10 nm together with the branched-polymer-like structure jointed by each silica nanoparticles, indicating it inherits the most important features of SG and AM.

8.3 Thermal properties measurement of pristine black phosphorus

The thermal conductivity measurements of mesoporous silica were performed using time-domain thermoreflectance (TDTR) method, a well-established thermal characterization technique based on ultrafast femtosecond laser pump-probe technique. Our experimental setup is shown as Figure 8.2(a) and details about TDTR method can be found in literature.[37,80,81,124] Briefly speaking, a thin aluminum film (80 nm) is deposited on the top surface of the samples, serving as both transducer to convert laser energy to thermal energy and temperature sensor. The absorbed energy from pump beam with wavelength of 400 nm leads to an instantaneous temperature rise. The probe beam at wavelength of 800 nm is used to continuously detect temperature decay. The delay time between pump pulse and probe pulse can be controlled with sub-picosecond temporal resolution. The full transient decay curve from 100 ps to 5000 ps can be fitted based on a layered thermal

diffusion model to obtain the effective thermal conductivity of the mesoporous film. The validity of the model is justified by (i) the clear interface between Al and sample, (ii) negligible diffusion of Al into pores, and (iii) smooth surface, as illustrated by the cross-section SEM image shown in Figure 8.2(b). In addition, Figure 8.2(c) shows the atomic force microscope image of the sample surface and establishes that the surface roughness of the Al-coated sample was around 2.2 nm, thus fulfilling the flat surface assumption. Lock-in technique is utilized here to improve the signal to noise ratio and the modulation frequency used here was 9.8 MHz. To accommodate for the potential inhomogeneity in the local thermal conductivity induced by random network of silica, large laser spot size with diameter of 20 μm was used to average the local structural difference effects during measurements. Moreover, for each sample, the thermal conductivity was measured at ten different spots on the mesoporous sample and averaged. The measurements were performed in a cryostat with pressure less than 1 Pa at room temperature after dehydrating samples at 150 ^{o}C for more than 12 hours. Figure 8.2(d) shows three typical smooth experimental raw datasets with the best fit curve, confirming the validity of our heat conduction model.

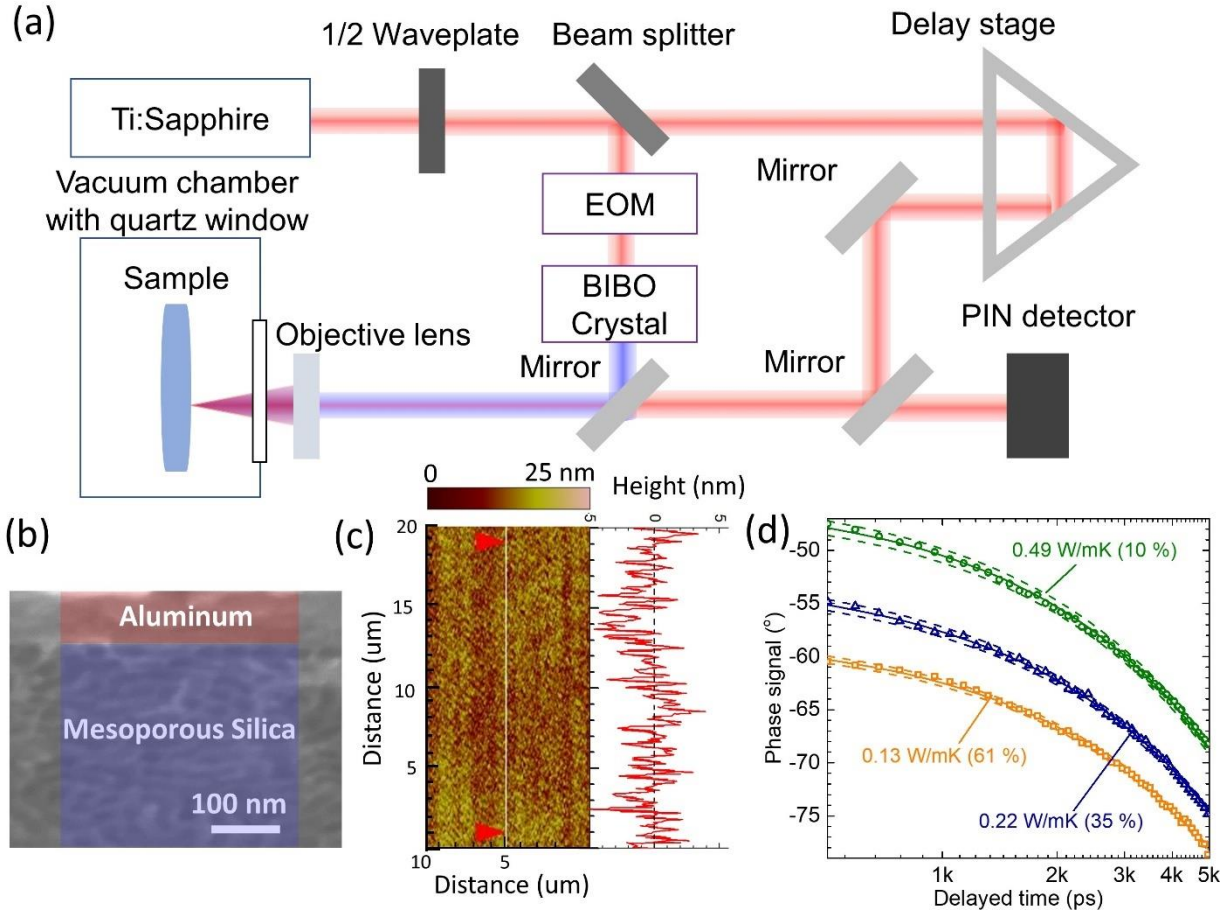

Figure 8.2 Thermal conductivity characterization of mesoporous SiO_2. a) Schematic of time-domain thermoreflectance setup; b) A typical cross-sectional SEM image shows the clear layered structure of Al/SiO_2 structure, required by the layered heat conduction model of TDTR; c) A typical AFM image demonstrates the flatness and uniformity of surface of the sample with roughness 2.2 nm; d) Three typical TDTR data sets from mesoporous samples with different porosities accompanied with their best fitting curve.

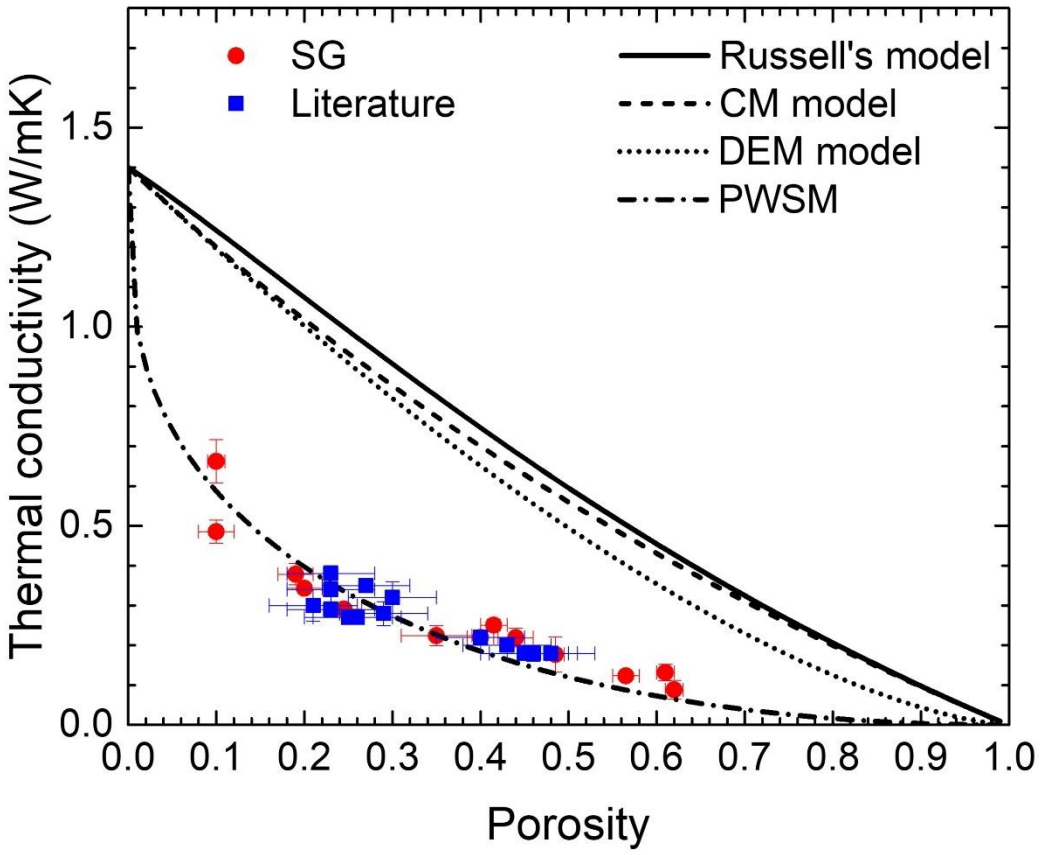

Figure 8.3 The measured thermal conductivity of SG samples compared with literature values[30] and predicted effective thermal conductivity using different thermal models. The theoretical curves given by several classic models for porous medium show their failure to predict thermal conductivity of mesoporous SiO_2.

8.4 Thermal modelling of mesoporous silica considering carriers' scattering

In the literature, porosity and pore size are usually key parameters used to evaluate the effective thermal conductivity of mesoporous materials. In particular, for porous amorphous materials, such as porous silica, porosity is believed to be the dominant factor that determines the thermal conductivity.[30,323] Here, the samples of different pore size and porosity were synthesized through the use of different block-copolymers and different polymer to TEOS ratios. Ellipsometric porosimetry measurements were performed with a PS-1100 instrument from Semilab using toluene as the adsorbate to measure the porosity and pore size distribution of all samples. The porosity of AM samples ranged from ~35% to ~70%. For SG, the porosity was successfully varied from ~10% to ~70%. For NPS, the upper bound was also ~70% while the lower bound was around ~35%, corresponding to the porosity of close random packing of nanoparticles spheres[20].

Figure 8.3 reports the thermal conductivity measured for SG samples with different porosities together with data for SGS obtained from the literature[30]. Several classical models were used to calculate the effective thermal conductivity. The thermal conductivity measurements of our SG samples were consistent with those collected from the literature. In addition, the results show much stronger dependence on porosity than simple linear relationship. At porosity around 50%, the thermal conductivity reduces to around 0.3 W/mK, corresponding to about 20% of the thermal conductivity of dense silica (1.4 W/mK)[305]. This was much lower than the effective thermal conductivity of mesoporous silica predicted from the classical models based on Clausius-Mossotti (CM) approximation and differential effective medium (DEM) approximation. Although CM and DEM models were initially designed for predicting the dielectric constant of composites, both have also been used for calculating the effective thermal conductivity of porous solid by considering the spherical cavities in the matrix.[323–325] However, these two models significantly overestimate

the thermal conductivity of mesoporous silica. The Russell's model[307,326] is another effective thermal conductivity model based on Fourier's law and developed for porous medium with periodic spherical pores. It is expressed as,

$$(\kappa_{eff}/\kappa_m) = \frac{1-\phi^{2/3}}{1-\phi^{2/3}+\phi} \tag{8-1}$$

where ϕ is the porosity and κ_{eff}/κ_m is the ratio of effective thermal conductivity of porous medium to the matrix. However, the predicted values are also significantly higher than the measurements, suggesting that non-Fourier heat conduction could happen even in mesoporous silica. The porosity weighted simple model (PWSM)[30] can achieve good agreement with the experimental results. However, the PWSM is a simple combination of series model and parallel model with a weighing factor, accounting for all the structural factors. This weighing factor can only be fitted from experimental values and do not have a clear physical explanation. Therefore, to provide better fundamental insight into thermal transport in mesoporous silica, a more detailed model that can capture the effects of nanoarchitecture and transport mechanisms needs to be developed.

Fundamentally, thermal transport in mesoporous silica (e.g., aerogel) can be divided into three parts: solid heat conduction, gaseous heat conduction, and heat convection, and thermal radiation as illustrated in Figure 8.4 (a)[306,327]. In our mesoporous silica samples, heat conduction through the entrapped air should be negligible due to the high vacuum and strong confinement of gas molecules in mesopores. The contribution from thermal radiation can also be neglected, based on our knowledge about silica aerogel, for which the contributions of radiation transport to the effective thermal conductivity becomes important only if the porosity exceeds 90%[327]. Thus, thermal transport through the solid phases dominates and will be considered in the rest of the manuscript.

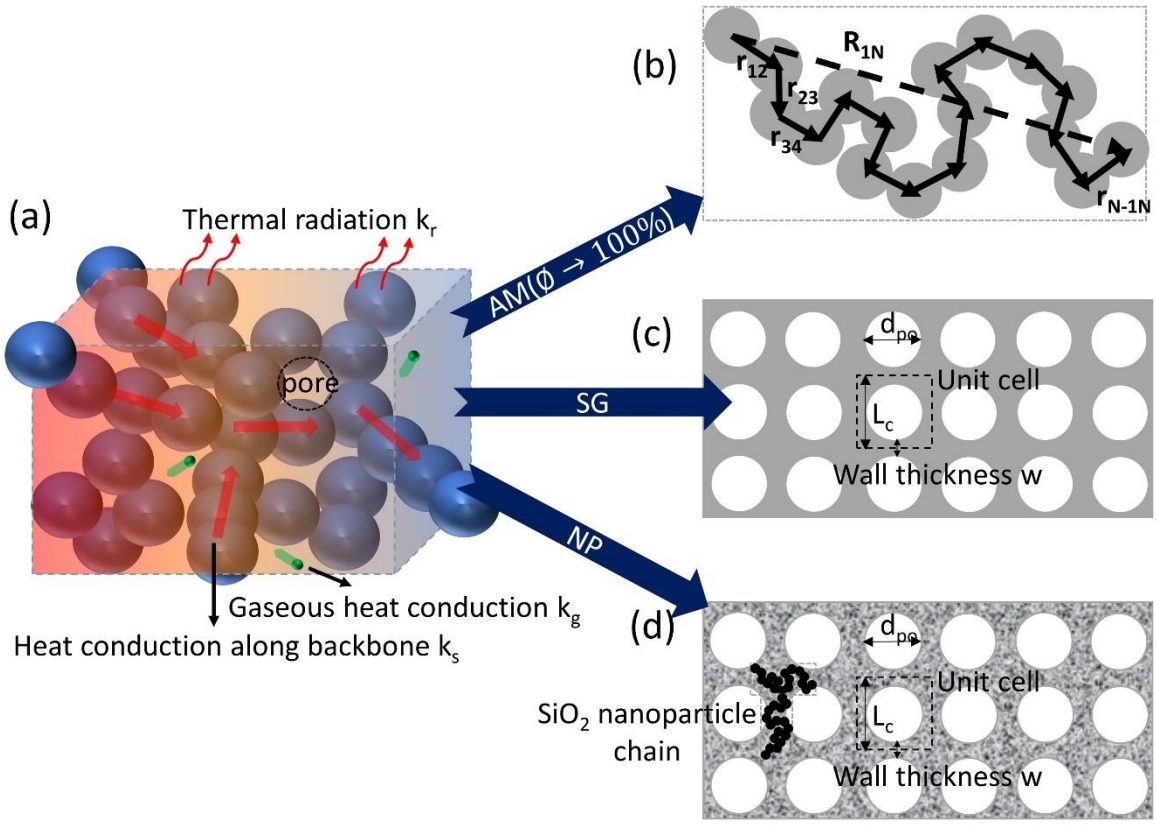

Figure 8.4 Schematic for thermal modelling of mesoporous SiO_2. a) Thermal transport pathways in porous mediums; b). The schematic for AM with extremely high porosity, reflecting the branched-polymer-like structure elongates heat conduction path by random bonding between different nanoparticles; c) The schematic for SG film, representing the ordered spherical porous structure; d) The schematic for NP film, demonstrating both the spherical pores and pseudo-matrix made of nanoparticles.

Here, we consider the ballistic thermal transport due to specific nanoarchitectures. Although nanoscale thermal transport has been intensely studied during the last several decades[7,8], the study on non-Fourier transport in amorphous materials is far behind that in crystalline materials. From the early study of temperature dependence of thermal conductivity, heat carriers mean free path in amorphous silica was considered to be less than 1 nm.[9,328] But observations of decreasing thermal conductivity with decreasing film thickness of amorphous silica thin films when thickness is less

than 30 nm disagreed with such claim[329]. In addition, the most recent experimental study on ballistic vibrational modes transport across silica/Si/silica heterostructures revealed that the mean free path of vibrational modes in silica was around 4 nm.[330] Since the transport of vibrational modes in amorphous solid is not completely diffusive,[312,331,332] thermal transport in mesoporous silica is determined not only by the complex heat conduction network due to the porosity but also by the confinement of heat carriers in nanostructures. Then, the effective thermal conductivity of mesoporous silica can be expressed, by analogy with crystals, as[14]

$$\kappa_{eff} = \kappa_D S_B \tag{8-2}$$

where κ_D is the thermal conductivity calculated from Fourier theory and structural factors (e.g., porosity) assuming completely diffusive thermal transport and S_B is a correction factor accounting for the ballistic effects, i.e. the suppression of thermal transport due to vibrational modes scattering with nanostructures.

For AM samples, the structure of AM samples is illustrated by the TEM image of Figure 8.1 (b). The silica nanoparticles join with each other to form a rigid network. To make the modelling mathematical tractable, the following assumptions were made: (1) the nanoparticles were treated as spherical and monodisperse with diameter d_{pa} = 10 nm. (2) The porous structure was represented by that shown in Figure 8.4 (b), which should be valid at high porosity[333]. (3) Each silica nanoparticle can bind with two neighbor nanoparticles. (4) the orientation of each nanoparticle is random relative to its neighboring nanoparticles. The heat conduction analysis can be performed based on single chain. For a single chain of N monodisperse nanoparticles with diameter d_{pa}, the real heat conduction length is given Nd_{pa}. The nominal heat conduction length can be calculated as

$$|< \boldsymbol{R_{1N}} >| = \sqrt{|\boldsymbol{r_{12}}|^2 + |\boldsymbol{r_{23}}|^2 + \cdots + |\boldsymbol{r_{N-1N}}|^2 + 2\sum_{i\neq j}^{N}|< \boldsymbol{r_{ii+1}}\boldsymbol{r_{jj+1}} >|} = \sqrt{N}d_{pa} \quad (8\text{-}3)$$

where $\boldsymbol{r_{i+1}}$ is the vector pointing to the (i+1)th particle from ith particle and <…> is the ensemble average on all the possible configurations of the single chain. The particle number *N* and porosity ϕ can be related with each other by

$$1 - \emptyset = \frac{N\pi d_{pa}^3/6}{(\sqrt{N/3}d_{pa})^3} = \frac{\sqrt{3}\pi}{2\sqrt{N}}. \quad (8\text{-}4)$$

According to Fourier's law, $\mathrm{Q} = \kappa A\frac{\Delta T}{L}$, where *Q* is the heat transfer rate (in W), *A* is the cross-sectional area through which heat is conducted, while ΔT is the temperature difference across a distance *L*. For porous medium, the cross-section area and heat conduction pathlength for heat conduction are reduced and increased respectively compared with the dense and homogeneous matrix. Thus, the κ_D can be expressed as

$$\kappa_D = \kappa_M \frac{|<\boldsymbol{R_{1N}}>|/\sqrt{3}}{Nd_{pa}} \frac{\pi {d_{pa}}^2/4}{|<\boldsymbol{R_{1N}}>|^2/3} = \frac{2}{3\pi^2}\kappa_M(1-\emptyset)^3. \quad (8\text{-}5)$$

For the lower porosity limit (35%)[334], the structure of the AM samples is a close packed spherical nanoparticles bed. From the TEM image in Figure 8.1(b), the nanoparticles appear to be fused with each other and interfacial thermal resistance is negligible compare with the thermal resistance of individual nanoparticle. By ignoring the contact resistance between individual nanoparticles, the parallel heat conduction model was applied to this system[335],

$$\kappa_D = \kappa_M(1-\emptyset). \quad (8\text{-}6)$$

Between the limits of porosity of 35% to 100%, the power factors and the scale factors in Eqn. (8-5) and (6) were assumed to change linearly from 1 to 3 and from 1 to $\frac{2}{3\pi^2}$. Therefore, the thermal conductivity for the whole porosity range can be derived as

$$\kappa_D = (1.50 - 1.43\emptyset)\kappa_M(1-\emptyset)^{3.08\emptyset-0.08}. \quad (8\text{-}7)$$

Moreover, the boundary of each nanoparticle is an important source of scattering that affect the vibrational modes of heat carriers in AM samples. Thus, the average mean free path of vibrational modes can be calculated according to Chen's model[306,336]

$$\Lambda_t = \Lambda_M \frac{3d_{pa}}{3d_{pa}+8\Lambda_M} \quad (8\text{-}8)$$

where Λ_M is the intrinsic mean free path of heat carriers in dense silica. And the effective thermal conductivity for ambigel samples can be estimated from

$$\kappa_{eff,AM} = (1.50 - 1.43\emptyset)\kappa_{dense}(1-\emptyset)^{3.08\emptyset-0.08}\frac{3d_{pa}}{3d_{pa}+8\Lambda_M} \quad (8\text{-}9)$$

For SG samples, since the spherical pores are arranged orderly in the medium as illustrated in Figure 8.4(c), the κ_D of SG sample can be described by Russell's model,

$$\kappa_D = \kappa_M \frac{1-\phi^{2/3}}{1-\phi^{2/3}+\phi}. \quad (8\text{-}10)$$

For the ballistic correction factor, the nanopores' wall introduces scattering in addition to scattering among heat carriers also occurring in the bulk material. According to Majumdar's model, the average mean free path of vibrational modes can be expressed as[337]

$$\Lambda_t = \Lambda_M \frac{3w}{3w+4\Lambda_M} \quad (8\text{-}11)$$

where w is the wall thickness of the nanopores. The wall thickness can be estimated based on each unit cubic cell containing one spherical pore. The porosity of the sample is related with the length of each cube L_c and pore diameter d_{po} by

$$\emptyset \propto \frac{d_{po}^3}{L_c^3}. \quad (8\text{-}12)$$

At high porosity, the pores will deviate from a perfectly spherical shape to maintain the structural robustness and $\emptyset = 100\%$ when d_{po} approaches to L_c. Thus, it is assumed that $\emptyset = \frac{d_{po}^3}{L_c^3}$. Thus, the wall thickness can be estimated from porosity ϕ and pore diameter d_{po} by

$$w = (\emptyset^{-\frac{1}{3}} - 1)d_{po}. \tag{8-13}$$

The correction factor due to ballistic transport would be

$$S_B = \frac{\Lambda_t}{\Lambda_M} = \frac{3w}{3w+4\Lambda_M}. \tag{8-14}$$

Combining Eqn. (8-2), (8-10), and (8-14), the effective thermal conductivity of SG samples can be written as

$$\kappa_{eff,SG} = \kappa_M \frac{1-\phi^{2/3}}{1-\phi^{2/3}+\phi} \frac{3(\emptyset^{-\frac{1}{3}}-1)d_{po}}{3(\emptyset^{-\frac{1}{3}}-1)d_{po}+4\Lambda_M}. \tag{8-15}$$

Nanoparticle-based mesoporous silica samples possess both features of AM and SG samples. Based on observation of the SEM image of Figure 8.2 (d), both spherical pores and silica nanoparticle chains exist in NP samples. An ideal schematic of NP sample is illustrated in Figure 8.4(d). The NP sample can be analogue with SG sample with pores left by polymer template. However, the matrix is not dense silica but an aggregation of nanoparticles, similar with ambigel. Thus, the porosity of NP samples can be divided into two sub-porosities. Porosity ϕ_1 is from the pores left by the polymer template and porosity ϕ_2 is due to the nanoparticle aggregation structure that prevails even in absence of polymer templates. They can be related to the total porosity by

$$1 - \emptyset = (1 - \emptyset_1)(1 - \emptyset_2) \tag{8-16}$$

Unfortunately, it remains unclear how much each form of porosity contributes to the total porosity. To make the model mathematically feasible, an assumption is given that total porosity is contributed equally by two reasons so that,

$$(1-\emptyset_1)=(1-\emptyset_2)=(1-\emptyset)^{1/2} \tag{8-17}$$

If we exclude the space left by the polymer template corresponding to porosity ϕ_1, the remaining volume can be treated as a pseudo-matrix, which has the same structure as that of AM. Then, the thermal conductivity of NP sample is analogous to SG samples so that

$$\kappa_{eff}=\kappa_{pseudo-M}\kappa_M\frac{1-{\phi_1}^{2/3}}{1-{\phi_1}^{2/3}+\phi_1}. \tag{8-18}$$

Here, scattering of the vibrational modes by large pores is not considered because most of the scattering happens at the boundary of each nanoparticle. The thermal conductivity of the pseudo-solid can be calculated from Eqn. (8-9) developed for ambigel

$$\kappa_{pseudo-solid}=(1.50-1.43\emptyset_2)\kappa_M(1-\emptyset_2)^{3.08\emptyset_2-0.08}\frac{3d_{pa}}{3d_{pa}+8\Lambda_M} \tag{8-19}$$

As a result, the effective thermal conductivity of NP sample is

$$\kappa_{eff,NP}=(1.50-1.43\emptyset_2)\kappa_M(1-\emptyset_2)^{3.08\emptyset_2-0.08}\frac{1-{\phi_1}^{2/3}}{1-{\phi_1}^{2/3}+\phi_1}\frac{3d_{pa}}{3d_{pa}+8\Lambda_M} \tag{8-20}$$

It should be noted here that the thermal conductivity of dense silica in our samples is not necessarily equal to the thermal conductivity of bulk thermal oxide reported in literature[338]. It was observed the so-called dense silica may have different thermal conductivity because of different synthesis method[339]. The thermal conductivity of silica prepared with TEOS is usually around 1 W/mK[338,339]. Thus, the parameters κ_M was set as 1 W/mK for all the models. The Λ_M in Eqn. (8-9), (8-15) and (8-20) were fitted by least square method to fit the experimental data for AM, SG, NP samples respectively. Figure 8.5 plots the above model prediction along with the experimental results for AM, SG, and NP samples. The results indicate that for total porosity ϕ < 45%, AM samples have higher thermal conductivity than NPS samples while SG samples have the smallest thermal conductivity. And for porosity > 60%, AM samples have smallest thermal conductivity.

All three models, based on kinetic theory, show excellent agreement with experimental data using Λ_M = 1.8-4.2 nm.

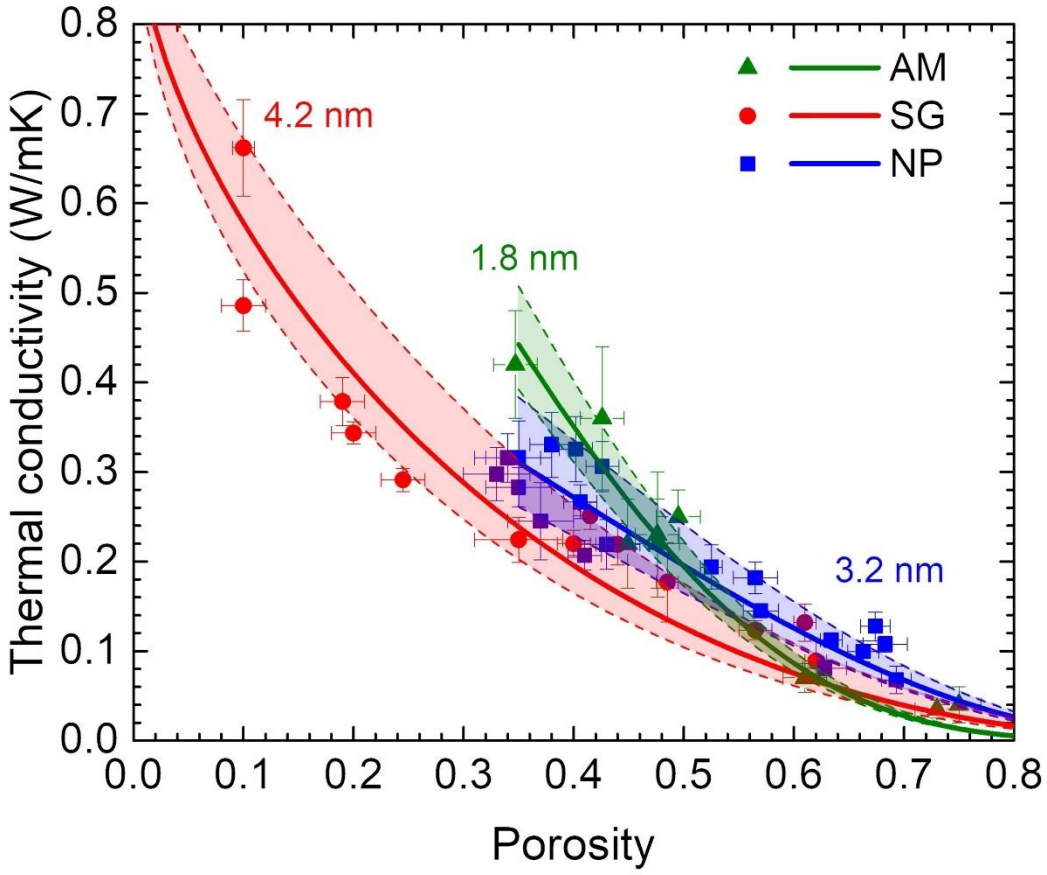

Figure 8.5 The successful application of our models on three kinds of mesoporous SiO_2 (green for AM, red for SG, and blue for NP. The overlapping between three best fitting solid curves and three sets of experimental data demonstrate agreement between our three distinct models with three different mesoporous SiO_2. The shallows stand for 30% variation of the best fitting mean free path of vibrational modes.

Although the mean free path of vibrational modes retrieved here for dense silica prepared with TEOS is much longer than the mean free path expected from the traditional knowledge about silica[9,305,310], it's on the same order of magnitude as that of recent studies[312,313]. The most recent knowledge about vibrational properties in amorphous silica revealed that there are three different modes responsible for heat transport: propagating proagons, diffusive diffusons and localized locons[312,314,331,340]. The propagons were found to travelled long distances before colliding with one another, up to more than 100 nm in amorphous silicon and 10 nm in amorphous silica[312]. This is consistent with our discovery. Another delicately designed experiment on ballistic transport across heterostructures involving silica also supports our results in which the average mean free path of vibrational modes in silica was reported to be as high as ~4 nm[313]. Therefore, although the extremely small mean free path of vibrational modes prevented us to from directly mapping the vibrational modes spectra, the mesoporous structure enables us to observe strong vibrational modes confinement effects.

8.5 Verification of carriers' scattering using size effects

To further confirm the propagating feature of vibrational modes in silica and validate our thermal conductivity models, the pore size effects on thermal conductivity of porous amorphous silica were also investigated. The strong pore size-dependent thermal conductivity of porous silicon had been widely observed because of the long mean free path of phonons in silicon and the capability of modern lab to fabricate porous silicon with variable pore size from tens to thousands of nanometers[307,341–343]. Similar experimental exploration on silica is much more challenging because of the extremely small mean free path of vibrational modes. Here we prepared SG samples

with different pore size varying from 2 nm to 25 nm with different templating polymers. The SG samples made with surfactants CTAB and Brij®C10 had very small pores between 2 and 4 nm. On the other hand, the SG samples templated with block copolymers PBO-PEO had large pores with diameter between 15 and 25 nm. All the SG samples had similar porous structure with highly ordered spherical pores.

Figure 8.6 plots the measured thermal conductivity as a function of porosity for SG samples with different pore sizes. It indicates that the SG films templated with PBO-PEO, had larger thermal conductivity than SG films templated with surfactants. The films templated with Pluronic F127 have the second highest thermal conductivity, followed by films templated with CTAB and Brij®C10. In another word, the thermal conductivity decreased with decreasing pore size for any given porosity. For the SG samples with 2-4 nm, we used two different templating polymers and observed similar thermal properties, which exclude the other potential effects brought by the polymers. The experimental results verify the existence of boundary scattering of vibrational modes in the nanostructure of amorphous silica. Figure 8.6 also plots three trend lines for thermal conductivity of SG films with different pore sizes ranging from 3 nm to 20 nm predicted by Eqn. (8-15). The model predictions (dark yellow line) for SG film with pore size of 5 nm agrees well with the samples prepared with CTAB and Brij®C10. Similarly, the model predictions (violet line) shows good consistence with SG films synthesized by PBO-PEO.

Furthermore, to quantitatively understand the ballistic transport process of vibrational modes in porous silica, we apply the variance-reduced Monte Carlo method to solve the three-dimensional spectral Boltzmann transport equation,

$$\frac{\partial f_\omega}{\partial t} + \boldsymbol{v}(\omega, p) \cdot \nabla f_\omega = -\frac{f_\omega - f_{\omega,0}}{\tau(\omega,p)} \tag{8-21}$$

where $f_\omega(\omega, p)$ is the spectral distribution of vibrational modes, and $f_{\omega,0}$ is the equilibrium Bose-Einstein distribution. $\boldsymbol{v}(\omega, p)$ and $\tau(\omega, p)$ are respectively the heat carrier's group velocity and lifetime at frequency ω and polarization p. The inputs of the model include the spectral density of state $D(\omega, p)$, the spectral group velocity $\boldsymbol{v}(\omega, p)$, and the spectral lifetime $\tau(\omega, p)$, which were obtained by fitting the molecular dynamics simulation results performed by Larkin and McGaughey[312]. The details of the simulations can be found in literatures[53,344]. The geometric structure of porous silica is simplified as one cubic cell in Figure 8.4b. Thermally insulating boundary conditions was imposed on all the inner surface of the pores. The temperature at one side of the cubic cell was fixed at 300 K whereas the heat flux was imposed on the opposite side. The temperature difference across the cell was sampled in the VMRC simulations for a given heat flux, and the effective thermal conductivity of the porous silica can be calculated from Fourier's law. The dot lines in Figure 8.6 show the thermal conductivity of porous silica calculated by VRMC simulation for different values of porosity and pore size. The suppression effects of the vibrational modes can be observed in the reduction of the effective thermal conductivity with decreased pore size from 20 to 5 nm. The consistence between the physical model predictions, experimental measurements, and Boltzman transport simulations further prove the validity of our kinetic theory based thermal conductivity model for mesoporous silica.

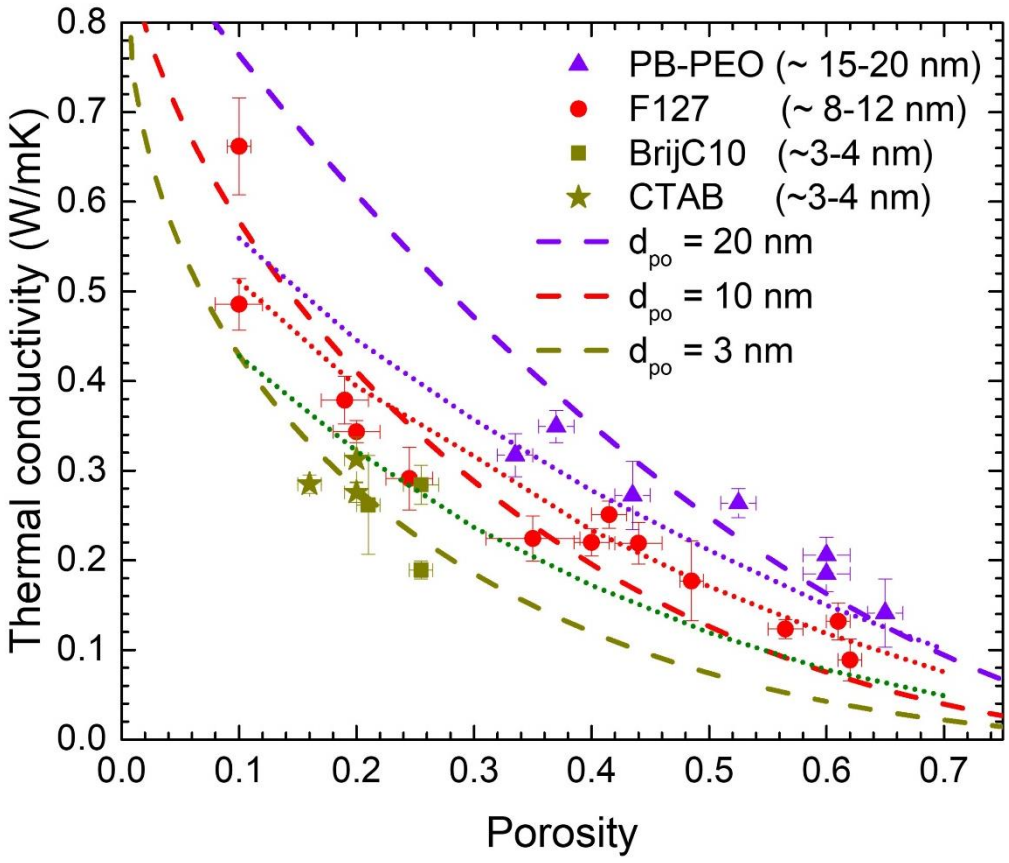

Figure 8.6 The supporting evidence of heat carriers scattering in mesoporous silica revealed by the pore size effects on thermal conductivity. The SG films prepared with PB-PEO, Pluronic F127, Brij®C10, CTAB templating polymers have different pore size ranging from ~20 nm, ~10 nm, ~3 nm and ~3 nm, respectively. The experimental thermal conductivity of samples with different pore size follow the dash trend lines according to our kinetic theory-based model and the dot trend lines from Boltzmann transport equation calculations.

8.6 Summary

In summary, we synthesized and characterized the structure-dependent thermal transport properties of three different kinds of mesoporous silica. AM had the highest thermal conductivity below porosity of 50% followed by NPS and SNG in the order of decreasing conductivity. By contrast, AM had the lowest thermal conductivity at porosities exceeding 65% followed by SG and NP. Three distinct thermal conductivity models were built for each mesoporous silica type by

considering their specific nanoarchitectures and accounting for the ballistic transport of heat carriers. All the models showed excellent agreement with experimental data and correctly captured the strong porosity dependence of thermal conductivity on AM, SG and NP samples. The mean free path of heat carriers in silica was estimated to be around 1.8-4.2 nm from all three type of nanoarchitectures. The models and the estimated mean free path of heat carriers were applied to experimental results of mesoporous silica samples with varying pore sizes and correctly explained the observed trends. Overall, this study improved the fundamental understanding of thermal transport in mesoporous and amorphous solids.

References

(1) Ball, P. Computer Engineering: Feeling the Heat. *Nature* 492, 174 (2012).

(2) U.S. Energy Information Administration. *International Energy Outlook 2016* (2016).

(3) Snyder, G. J.; Toberer, E. S. Complex Thermoelectric Materials. *Nature Materials* 7, 105 (2008).

(4) Singh, P.; Ravindra, N. M. Temperature Dependence of Solar Cell Performance—an Analysis. *Solar Energy Materials and Solar Cells* 101, 36 (2012).

(5) Green, M. A.; Hishikawa, Y.; Dunlop, E. D.; Levi, D. H.; Hohl-Ebinger, J.; Ho-Baillie, A. W. Y. Solar Cell Efficiency Tables (Version 52). *Progress in Photovoltaics: Research and Applications* 26, 427 (2018).

(6) Dresselhaus, M. S.; Chen, G.; Tang, M. Y.; Yang, R.; Lee, H.; Wang, D.; Ren, Z.; Fleurial, J. P.; Gogna, P. New Directions for Low-Dimensional Thermoelectric Materials. *Advanced Materials* 19, 1043 (2007).

(7) Cahill, D. G.; Ford, W. K.; Goodson, K. E.; Mahan, G. D.; Majumdar, A.; Maris, H. J.; Merlin, R.; Phillpot, S. R. Nanoscale Thermal Transport. *Journal of Applied Physics* 93, 793 (2003).

(8) Cahill, D. G.; Braun, P. v.; Chen, G.; Clarke, D. R.; Fan, S.; Goodson, K. E.; Keblinski, P.; King, W. P.; Mahan, G. D.; Majumdar, A.; Maris, H. J.; Phillpot, S. R.; Pop, E.; Shi, L. Nanoscale Thermal Transport. II. 2003–2012. *Applied Physics Reviews* 1, 011305 (2014).

(9) Cahill, D. G.; Pohl, R. O. Thermal Conductivity of Amorphous Solids above the Plateau. *Physical Review B* 35, 4067 (1987).

(10) Schmidt, A.; Chiesa, M.; Chen, X.; Chen, G. An Optical Pump-Probe Technique for Measuring the Thermal Conductivity of Liquids. *Review of Scientific Instruments* 79, 064902 (2008).

(11) Shi, L.; Li, D.; Yu, C.; Jang, W.; Kim, D.; Yao, Z.; Kim, P.; Majumdar, A. Measuring Thermal and Thermoelectric Properties of One-Dimensional Nanostructures Using a Microfabricated Device. *Journal of Heat Transfer* 125, 881 (2003).

(12) Balandin, A. A.; Ghosh, S.; Bao, W.; Calizo, I.; Teweldebrhan, D.; Miao, F.; Lau, C. N. Superior Thermal Conductivity of Single-Layer Graphene. *Nano Letters* 8, 902 (2008**)**.

(13) Siemens, M. E.; Li, Q.; Yang, R.; Nelson, K. A.; Anderson, E. H.; Murnane, M. M.; Kapteyn, H. C. Quasi-Ballistic Thermal Transport from Nanoscale Interfaces Observed Using Ultrafast Coherent Soft X-Ray Beams. *Nature Materials* 9, 26 (2010).

(14) Hu, Y.; Zeng, L.; Minnich, A. J.; Dresselhaus, M. S.; Chen, G. Spectral Mapping of Thermal Conductivity through Nanoscale Ballistic Transport. *Nature Nanotechnology* 10, 701 (2015).

(15) Machida, Y.; Subedi, A.; Akiba, K.; Miyake, A.; Tokunaga, M.; Akahama, Y.; Izawa, K.; Behnia, K. Observation of Poiseuille Flow of Phonons in Black Phosphorus. *Science Advances* 4, eaat3374 (2018).

(16) Fugallo, G.; Cepellotti, A.; Paulatto, L.; Lazzeri, M.; Marzari, N.; Mauri, F. Thermal conductivity of graphene and graphite: collective excitations and mean free paths. *Nano Letters* 14, 6109 (2014).

(17) Broido, D. A.; Malorny, M.; Birner, G.; Mingo, N.; Stewart, D. A. Intrinsic Lattice Thermal Conductivity of Semiconductors from First Principles. *Applied Physics Letter* 91, 231922 (2007).

(18) Esfarjani, K.; Chen, G.; Stokes, H. T. Heat Transport in Silicon from First-Principles Calculations. *Physical Review B* 84, 085204 (2011).

(19) Kang, J. S.; Li, M.; Wu, H.; Nguyen, H.; Hu, Y. Experimental Observation of High Thermal Conductivity in Boron Arsenide. *Science* 361, 575 (2018).

(20) Pietrak, K.; Winiewski, T. S. A Review of Models for Effective Thermal Conductivity of Composite Materials. *Journal Journal of Power Technologies* 95, 14 (2015).

(21) Tang, J.; Wang, H. T.; Lee, D. H.; Fardy, M.; Huo, Z.; Russell, T. P.; Yang, P. Holey Silicon as an Efficient Thermoelectric Material. *Nano Letters* 10, 4279 (2010).

(22) Abeles, B. Lattice Thermal Conductivity of Disordered Semiconductor Alloys at High Temperatures. *Physical Review* 131, 1906 (1963).

(23) Garg, J.; Bonini, N.; Kozinsky, B.; Marzari, N. Role of Disorder and Anharmonicity in the Thermal Conductivity of Silicon-Germanium Alloys: A First-Principles Study. *Physical Review Letters* 106, 045901 (2011**)**.

(24) Monachon, C.; Weber, L.; Dames, C. Thermal Boundary Conductance: A Materials Science Perspective. *Annual Review of Materials Research* 46, 433 (2016).

(25) Jiang, H.; Lee, P. S.; Li, C. 3D Carbon Based Nanostructures for Advanced Supercapacitors. *Energy and Environmental Science* 6, 41 (2013).

(26) Prasher, R. Thermal Interface Materials: Historical Perspective, Status, and Future Directions. *Proceedings of the IEEE* 94, 1571 (2006).

(27) Biswas, K.; He, J.; Blum, I. D.; Wu, C. I.; Hogan, T. P.; Seidman, D. N.; Dravid, V. P.; Kanatzidis, M. G. High-Performance Bulk Thermoelectrics with All-Scale Hierarchical Architectures. *Nature* 489, 414 (2012**)**.

(28) He, J.; Tritt, T.M. Advances in Thermoelectric Materials Research: Looking Back and Moving Forward. *Science* 357, eaak9997 (2017**)**.

(29) Shahil, K. M. F.; Balandin, A. A. Graphene-Multilayer Graphene Nanocomposites as Highly Efficient Thermal Interface Materials. *Nano Letters* 12, 861 (2012).

(30) Coquil, T.; Richman, E. K.; Hutchinson, N. J.; Tolbert, S. H.; Pilon, L. Thermal Conductivity of Cubic and Hexagonal Mesoporous Silica Thin Films. *Journal of Applied Physics* 106, 034910 (2009).

(31) Touloukian, Y. S.; Powel, R. W.; Ho, C. Y.; Klemens, P. G. Thermal Conductivity of Nonmetallic Solids. In *Thermophysical Properties of Matter*; IFI/Plenum: New York, 1970; Vol. 2, p 1389.

(32) Jang, W.; Chen, Z.; Bao, W.; Lau, C. N.; Dames, C. Thickness-Dependent Thermal Conductivity of Encased Graphene and Ultrathin Graphite. *Nano Letters* 10, 3909 (2010).

(33) Ghosh, S.; Bao, W.; Nika, D. L.; Subrina, S.; Pokatilov, E. P.; Lau, C. N.; Balandin, A. A. Dimensional Crossover of Thermal Transport in Few-Layer Graphene. *Nature Materials* 9, 555 (2010).

(34) Seol, J. H.; Jo, I.; Moore, A. L.; Lindsay, L.; Aitken, Z. H.; Pettes, M. T.; Li, X.; Yao, Z.; Huang, R.; Broido, D.; Mingo, N.; Ruoff, R. S.; Shi, L. Two-Dimensional Phonon Transport in Supported Graphene. *Science* 328, 213 (2010).

(35) Lindsay, L.; Li, W.; Carrete, J.; Mingo, N.; Broido, D. A.; Reinecke, T. L. Phonon Thermal Transport in Strained and Unstrained Graphene from First Principles. *Physical Review B* 89, 155426 (2014).

(36) Chiritescu, C.; Cahill, D. G.; Nguyen, N.; Johnson, D.; Bodapati, A.; Keblinski, P.; Zschack, P. Ultralow Thermal Conductivity in Disordered, Layered WSe2 Crystals. *Science* 315, 351 (2007).

(37) Kang, J. S.; Ke, M.; Hu, Y. Ionic Intercalation in Two-Dimensional van Der Waals Materials: In Situ Characterization and Electrochemical Control of the Anisotropic Thermal Conductivity of Black Phosphorus. *Nano Letters* 17, 1431 (2017).

(38) Jang, H.; Wood, J. D.; Ryder, C. R.; Hersam, M. C.; Cahill, D. G. Anisotropic Thermal Conductivity of Exfoliated Black Phosphorus. *Advanced Materials* 27, 8017 (2015).

(39) Sun, B.; Gu, X.; Zeng, Q.; Huang, X.; Yan, Y.; Liu, Z.; Yang, R.; Koh, Y. K. Temperature Dependence of Anisotropic Thermal-Conductivity Tensor of Bulk Black Phosphorus. *Advanced Materials* 29, 1603297 (2017).

(40) Smith, B.; Vermeersch, B.; Carrete, J.; Ou, E.; Kim, J.; Mingo, N.; Akinwande, D.; Shi, L. Temperature and Thickness Dependences of the Anisotropic In-plane Thermal Conductivity of Black Phosphorus. *Advanced Materials*, 29, 1603752 (2017).

(41) Lee, S.; Yang, F.; Suh, J.; Yang, S.; Lee, Y.; Li, G.; Choe, H. S.; Suslu, A.; Chen, Y.; Ko, C.; Park, J.; Liu, K.; Li, J.; Hippalgaonkar, K.; Urban, J. J.; Tongay, S.; Wu, J. Anisotropic In-Plane Thermal Conductivity of Black Phosphorus Nanoribbons at Temperatures Higher than 100 K. *Nature Communications* 6, 8573 (2015).

(42) Luo, Z.; Maassen, J.; Deng, Y.; Du, Y.; Garrelts, R. P.; Lundstrom, M. S.; Ye, P. D.; Xu, X. Anisotropic In-Plane Thermal Conductivity Observed in Few-Layer Black Phosphorus. *Nature Communications* 6, 8572 (2015).

(43) Zhu, J.; Park, H.; Chen, J. Y.; Gu, X.; Zhang, H.; Karthikeyan, S.; Wendel, N.; Campbell, S. A.; Dawber, M.; Du, X.; Li, M.; Wang, J. P.; Yang, R.; Wang, X. Revealing the Origins of 3D Anisotropic Thermal Conductivities of Black Phosphorus. *Advanced Electronic Materials* 2, 1600040 (2016).

(44) Shen, S.; Henry, A.; Tong, J.; Zheng, R.; Chen, G. Polyethylene Nanofibres with Very High Thermal Conductivities. *Nature Nanotechnology 5*, 251 (2010).

(45) Wang, X.; Ho, V.; Segalman, R. A.; Cahill, D. G. Thermal Conductivity of High-Modulus Polymer Fibers. *Macromolecules* 46, 4937 (2013).

(46) Hahn, D. W.; Özişik, M. N. *Heat Conduction in Anisotropic Solids*; Wiley Online Library, 2012.

(47) Gofryk, K.; Du, S.; Stanek, C. R.; Lashley, J. C.; Liu, X. Y.; Schulze, R. K.; Smith, J. L.; Safarik, D. J.; Byler, D. D.; McClellan, K. J.; Uberuaga, B. P.; Scott, B. L.; Andersson, D.

A. Anisotropic Thermal Conductivity in Uranium Dioxide. *Nature Communications* 5, 4551 (2014).

(48) Wang, M.; Lin, S. Anisotropic and Ultralow Phonon Thermal Transport in Organic–Inorganic Hybrid Perovskites: Atomistic Insights into Solar Cell Thermal Management and Thermoelectric Energy Conversion Efficiency. *Advanced Functional Materials*, 26, 5297 (2016).

(49) Graebner, J. E.; Jin, S.; Kammlott, G. W.; Herb, J. A.; Gardinier, C. F. Large Anisotropic Thermal Conductivity in Synthetic Diamond Films. *Nature* 359, 401 (1992).

(50) Sood, A.; Cho, J.; Hobart, K. D.; Feygelson, T. I.; Pate, B. B.; Asheghi, M.; Cahill, D. G.; Goodson, K. E. Anisotropic and Inhomogeneous Thermal Conduction in Suspended Thin-Film Polycrystalline Diamond. *Journal of Applied Physics* 119, 5103 (2016).

(51) Aksamija, Z.; Knezevic, I. Anisotropy and Boundary Scattering in the Lattice Thermal Conductivity of Silicon Nanomembranes. *Physical Review B* 82, 5319 (2010).

(52) Luckyanova, M. N.; Johnson, J. A.; Maznev, A. A.; Garg, J.; Jandl, A.; Bulsara, M. T.; Fitzgerald, E. A.; Nelson, K. A.; Chen, G. Anisotropy of the Thermal Conductivity in GaAs/AlAs Superlattices. *Nano Letters* 13, 3973 (2013).

(53) Kang, J. S.; Wu, H.; Hu, Y. Thermal Properties and Phonon Spectral Characterization of Synthetic Boron Phosphide for High Thermal Conductivity Applications. *Nano Letters* 17, 7507 (2017).

(54) Chen, Z.; Dames, C. An Anisotropic Model for the Minimum Thermal Conductivity. *Applied Physics Letters* 107, 193104 (2015).

(55) Won, Y.; Cho, J.; Agonafer, D.; Asheghi, M.; Goodson, K. E. Fundamental Cooling Limits for High Power Density Gallium Nitride Electronics. *IEEE Transactions on Components Packaging and Manufacturing Technology* 5, 737 (2015).

(56) Bar-Cohen, A.; Wang, P. On-Chip Thermal Management and Hot-Spot Remediation. In *Nano-Bio- Electronic, Photonic and MEMS Packaging*; 2010; pp 349–429.

(57) Ghoniem, N.; Walgraef, D. *Instabilities and Self-Organization in Materials*; Oxford University Press, 2008.

(58) Kraemer, D.; Poudel, B.; Feng, H. P.; Caylor, J. C.; Yu, B.; Yan, X.; Ma, Y.; Wang, X.; Wang, D.; Muto, A.; McEnaney, K.; Chiesa, M.; Ren, Z.; Chen, G. High-Performance Flat-

Panel Solar Thermoelectric Generators with High Thermal Concentration. *Nature Materials* 10, 532 (2011).

(59) Dames, C.; Chen, S.; Harris, C. T.; Huang, J. Y.; Ren, Z. F.; Dresselhaus, M. S.; Chen, G. A Hot-Wire Probe for Thermal Measurements of Nanowires and Nanotubes inside a Transmission Electron Microscope. *Review of Scientific Instruments 78*, 104903 (2007).

(60) Yan, X.; Poudel, B.; Ma, Y.; Liu, W. S.; Joshi, G.; Wang, H.; Lan, Y.; Wang, D.; Chen, G.; Ren, Z. F. Experimental Studies on Anisotropic Thermoelectric Properties and Structures of N-Type Bi2Te2.7Se0.3. *Nano Letters 10*, 3373 (2010).

(61) Wehmeyer, G.; Yabuki, T.; Monachon, C.; Wu, J.; Dames, C. Thermal Diodes, Regulators, and Switches: Physical Mechanisms and Potential Applications. *Applied Physics Reviews 4*, 041304 (2017).

(62) Slack, G. A. Thermal Conductivity of CaF2, MnF2, CoF2, and ZnF2 Crystals. *Physical Review 122*, 1451 (1961).

(63) Slack, G. A. Anisotropic Thermal Conductivity of Pyrolytic Graphite. *Physical Review*, *127*, 694 (1962).

(64) Parker, W. J.; Jenkins, R. J.; Butler, C. P.; Abbott, G. L. Flash Method of Determining Thermal Diffusivity, Heat Capacity, and Thermal Conductivity. *Journal of Applied Physics 32*, 1679 (1961).

(65) Golombok, M.; Shirvill, L. C. Laser Flash Thermal Conductivity Studies of Porous Metal Fiber Materials. *Journal of Applied Physics 63*, 1971 (1988).

(66) Cahill, D. G. Thermal Conductivity Measurement from 30 to 750 K: The 3ω Method. *Review of Scientific Instruments 61*, 802 (1990).

(67) Ju, Y. S. Thermal Characterization of Anisotropic Thin Dielectric Films Using Harmonic Joule Heating. *Thin Solid Films 339 1 (1990)*.

(68) Dames, C.; Chen, G. 1ω, 2ω, and 3ω Methods for Measurements of Thermal Properties. *Review of Scientific Instruments 76*, 1 (2005).

(69) Kim, P.; Shi, L.; Majumdar, A.; McEuen, P. L. Thermal Transport Measurements of Individual Multiwalled Nanotubes. *Physical Review Letters 87*, 215502 (2001).

(70) Li, D.; Wu, Y.; Kim, P.; Shi, L.; Yang, P.; Majumdar, A. Thermal Conductivity of Individual Silicon Nanowires. *Applied Physics Letters*, *83*, 2934 (2003).

(71) Mishra, V.; Hardin, C. L.; Garay, J. E.; Dames, C. A 3 Omega Method to Measure an Arbitrary Anisotropic Thermal Conductivity Tensor. *Review of Scientific Instruments* 86, 054902 (2015).

(72) Brovman, Y. M.; Small, J. P.; Hu, Y.; Fang, Y.; Lieber, C. M.; Kim, P. Electric Field Effect Thermoelectric Transport in Individual Silicon and Germanium/Silicon Nanowires. *Journal of Applied Physics* 119, 234304 (2016).

(73) Zheng, J.; Wingert, M. C.; Dechaumphai, E.; Chen, R. Sub-Picowatt/Kelvin Resistive Thermometry for Probing Nanoscale Thermal Transport. *Review of Scientific Instruments* 84, 114901 (2013).

(74) Zeng, Y.; Marconnet, A. A Direct Differential Method for Measuring Thermal Conductivity of Thin Films. *Review of Scientific Instruments* 88, 044901 (2017).

(75) D. A. Young; Thomsen, C.; Grahn, H. T.; Maris, H. J.; Tauc, J. *Phonon Scattering in Condensed Matter*; A. C. Anderson and J. P. Wolfe, Ed.; Springer: Berlin, 1986; Vol. 5.

(76) Paddock, C. A.; Eesley, G. L. Transient Thermoreflectance from Thin Metal Films. *Journal of Applied Physics* 60, 285 (1986).

(77) Capinski, W. S.; Maris, H. J. Improved Apparatus for Picosecond Pump-and-Probe Optical Measurements. *Review of Scientific Instruments* 67, 2720 (1996).

(78) Bonello, B.; Perrin, B.; Rossignol, C. Photothermal Properties of Bulk and Layered Materials by the Picosecond Acoustics Technique. *Journal of Applied Physics* 83, 3081 (1998).

(79) Taketoshi, N.; Baba, T.; Schaub, E.; Ono, A. Homodyne Detection Technique Using Spontaneously Generated Reference Signal in Picosecond Thermoreflectance Measurements. *Review of Scientific Instruments* 74, 5226 (2003).

(80) Cahill, D. G. Analysis of Heat Flow in Layered Structures for Time-Domain Thermoreflectance. *Review of Scientific Instruments* 75, 5119 (2004).

(81) Schmidt, A. J.; Chen, X.; Chen, G. Pulse Accumulation, Radial Heat Conduction, and Anisotropic Thermal Conductivity in Pump-Probe Transient Thermoreflectance. *Review of Scientific Instruments* 79, 114902 (2008).

(82) Feser, J. P.; Cahill, D. G. Probing Anisotropic Heat Transport Using Time-Domain Thermoreflectance with Offset Laser Spots. *Review of Scientific Instruments* 83, 104901 (2012).

(83) Feser, J. P.; Liu, J.; Cahill, D. G. Pump-Probe Measurements of the Thermal Conductivity Tensor for Materials Lacking in-Plane Symmetry. *Review of Scientific Instruments*, 85, 104903 (2014).

(84) Jiang, P.; Qian, X.; Yang, R. Time-Domain Thermoreflectance (TDTR) Measurements of Anisotropic Thermal Conductivity Using a Variable Spot Size Approach. *Review of Scientific Instruments* 88, 074901 (2017).

(85) Carslaw, H. S.; Jaeger, J. C. *Conduction of Heat in Solids*; Oxford University Press: New York, 1959.

(86) Bergman, T. L.; Incropera, F. P. *Fundamentals of Heat and Mass Transfer*; John Wiley & Sons, 2011.

(87) Gundrum, B. C.; Cahill, D. G.; Averback, R. S. Thermal Conductance of Metal-Metal Interfaces. *Physical Review B* 72, 245426 (2005).

(88) Shanks, H. R.; Maycock, P. D.; Sidles, P. H.; Danielson, G. C. Thermal Conductivity of Silicon from 300 to 1400°K. *Physical Review* 130, 1743 (1963).

(89) Wilson, R. B.; Cahill, D. G. Anisotropic Failure of Fourier Theory in Time-Domain Thermoreflectance Experiments. *Nat Communications, 5*, 5075 (2014).

(90) Lindsay, L.; Broido, D. A.; Reinecke, T. L. First-Principles Determination of Ultrahigh Thermal Conductivity of Boron Arsenide: A Competitor for Diamond? *Physical Review Letters* 111, 025901 (2013).

(91) Schmidt, A. J.; Collins, K. C.; Minnich, A. J.; Chen, G. Thermal Conductance and Phonon Transmissivity of Metal–Graphite Interfaces. *Journal of Applied Physics* 107, 104907 (2010).

(92) David R Lide, E. CRC Handbook of Chemistry and Physics, Internet Version 2007, (87th Edition). *Taylor and Francis Boca Raton FL* **2007**.

(93) Dobrovinskaya, E. R.; Lytvynov, L. A.; Pishchik, V. *Sapphire: Material, Manufacturing, Applications*; 2009.

(94) Jiang, P.; Qian, X.; Gu, X.; Yang, R. Probing Anisotropic Thermal Conductivity of Transition Metal Dichalcogenides MX2 (M = Mo, W and X = S, Se) Using Time-Domain Thermoreflectance. *Advanced Materials 29,* 1701068 (2017).

(95) Su, L.; Zhang, Y. Temperature Coefficients of Phonon Frequencies and Thermal Conductivity in Thin Black Phosphorus Layers. *Applied Physics Letters* 107, 071905 (2015).

(96) Zhang, Y.; Wang, J.; Liu, Q.; Gu, S.; Sun, Z.; Chu, P.K.; Yu, X. The electrical, thermal, and thermoelectric properties of black phosphorus. *APL Materials*, 8, 120903 (2020).

(97) Powers, J. M. On the Necessity of Positive Semi-Definite Conductivity and Onsager Reciprocity in Modeling Heat Conduction in Anisotropic Media. *Journal of Heat Transfer* 126, 670 (2004).

(98) Li, M.; Dai, L; Hu, Y. Machine Learning for Harnessing Thermal Energy: From Materials Discovery to System Optimization. *ACS Energy Letters* 7, 3204 (2022).

(99) Waldrop, M. M. The Chips Are down for Moore's Law. *Nature* 530, 144 (2016).

(100) *International technology roadmap for semiconductors (ITRS), 2015 ed.* http://www.itrs2.net/ (accessed 2019-08-10).

(101) Shehabi, A.; Smith, S.; Sartor, D.; Brown, R.; Herrlin, M.; Koomey, J.; Masanet, E.; Horner, N.; Azevedo, I.; Lintner, W. *United States Data Center Energy Usage Report*; Berkeley, CA, 2016.

(102) Ravichandran, N.K.; Broido, D. Non-monotonic Pressure Dependence of the Thermal Conductivity of Boron Arsenide. *Nature communications* 10, 827 (2019).

(103) Pop, E.; Sinha, S.; Goodson, K. E. Heat Generation and Transport in Nanometer-Scale Transistors. *Proceedings of the IEEE* 94, 1587 (2006).

(104) Balandin, A. A. Thermal Properties of Graphene and Nanostructured Carbon Materials. *Nature Materials* 10, 569–581 (2011).

(105) Sood, A.; Pop, E.; Asheghi, M.; Goodson, K. E. The Heat Conduction Renaissance. In *2018 17th IEEE Intersociety Conference on Thermal and Thermomechanical Phenomena in Electronic Systems (ITherm)*; IEEE, 2018; pp 1396–1402.

(106) Li, S.; Zheng, Q.; Lv, Y.; Liu, X.; Wang, X.; Huang, P. Y.; David, G.; Lv, B. High Thermal Conductivity in Cubic Boron Arsenide Crystals. *Science 361*, 579 (2018).

(107) Tian, F.; Song, B.; Chen, X.; Ravichandran, N. K.; Lv, Y.; Chen, K.; Sullivan, S.; Kim, J.; Zhou, Y.; Liu, T. H.; Goni, M.; Ding, Z.; Sun, J.; Gamage, G. A. G. U.; Sun, H.; Ziyaee, H.; Huyan, S.; Deng, L.; Zhou, J.; Schmidt, A. J.; Chen, S.; Chu, C. W.; Huang, P. Y.; Broido, D.; Shi, L.; Chen, G.; Ren, Z. Unusual High Thermal Conductivity in Boron Arsenide Bulk Crystals. *Science* 361, 582 (2018).

(108) Bar-Cohen, A.; Albrecht, J. D.; Maurer, J. J. Near-Junction Thermal Management for Wide Bandgap Devices. In *Technical Digest - IEEE Compound Semiconductor Integrated Circuit Symposium, CSIC*; 2011; pp 1–5.

(109) Eeckhout, L. Is Moore's Law Slowing Down? What's Next? IEEE Micro 37, 4 (2017).

(110) Padture, N. P.; Gell, M.; Jordan, E. H. Thermal Barrier Coatings for Gas-Turbine Engine Applications. *Science* 296, 280 (2002).

(111) Pollack, G. L. Kapitza Resistance. *Reviews of Modern Physics* 41, 48 (1969).

(112) Swartz, E. T.; Pohl, R. O. Thermal Boundary Resistance. *Review of Modern Physics* 61, 605 (1989).

(113) Novoselov, K. S.; Jiang, D.; Schedin, F.; Booth, T. J.; Khotkevich, V. V; Morozov, S. V; Geim, A. K. Two-Dimensional Atomic Crystals. *Proceedings of the National Academy of Sciences* 102, 10451 (2005).

(114) Wang, Q. H.; Kalantar-Zadeh, K.; Kis, A.; Coleman, J. N.; Strano, M. S. Electronics and Optoelectronics of Two-Dimensional Transition Metal Dichalcogenides. *Nature Nanotechnology* 7, 699 (2012).

(115) Xu, W.; Liu, W.; Schmidt, J. F.; Zhao, W.; Lu, X.; Raab, T.; Diederichs, C.; Gao, W.; Seletskiy, D. V; Xiong, Q. Correlated Fluorescence Blinking in Two-Dimensional Semiconductor Heterostructures. *Nature* 541, 62 (2017).

(116) Rivera, P.; Seyler, K. L.; Yu, H.; Schaibley, J. R.; Yan, J.; Mandrus, D. G.; Yao, W.; Xu, X. Valley-Polarized Exciton Dynamics in a 2D Semiconductor Heterostructure. *Science* 351, 688 (2016).

(117) Lin, Z.; Liu, Y.; Halim, U.; Ding, M.; Liu, Y.; Wang, Y.; Jia, C.; Chen, P.; Duan, X.; Wang, C. Solution-Processable 2D Semiconductors for High-Performance Large-Area Electronics. *Nature* 562, 254 (2018).

(118) Ling, X.; Wang, H.; Huang, S.; Xia, F.; Dresselhaus, M. S. The Renaissance of Black Phosphorus. *Proceedings of the National Academy of Sciences* 201416581 (2015).

(119) Morita, A. Semiconducting Black Phosphorus. *Applied Physics A* 39, 227 (1986).

(120) Bridgman, P. W. Two New Modifications of Phosphorus. *Journal of American Chemistry Society* 36, 1344 (1914).

(121) Sugai, S.; Shirotani, I. Raman and Infrared Reflection Spectroscopy in Black Phosphorus. *Solid State Communications* 53, 753 (1985).

(122) Wu, J.; Mao, N.; Xie, L.; Xu, H.; Zhang, J. Identifying the Crystalline Orientation of Black Phosphorus Using Angle-Resolved Polarized Raman Spectroscopy. *Angewandte Chemie* 127, 2396 (2015).

(123) Phaneuf-L'Heureux, A. L.; Favron, A.; Germain, J. F.; Lavoie, P.; Desjardins, P.; Leonelli, R.; Martel, R.; Francoeur, S. Polarization-Resolved Raman Study of Bulk-like and Davydov-Induced Vibrational Modes of Exfoliated Black Phosphorus. *Nano Letters* 16, 7761 (2016).

(124) Li, M.; Kang, J. S.; Hu, Y. Anisotropic Thermal Conductivity Measurement Using a New Asymmetric-Beam Time-Domain Thermoreflectance (AB-TDTR) Method. *Review of Scientific Instruments* 89, 08490 (2018).

(125) Yang, J.; Shen, M.; Yang, Y.; Evans, W.J.; Wei, Z.; Chen, W.; Zinn, A.A.; Chen, Y.; Prasher, R.; Xu, T.T.; Keblinski, P. Phonon Transport through Point Contacts between Graphitic Nanomaterials. *Physical Review Letters* 112, 205901 (2014).

(126) Zeng, L.; Collins, K. C.; Hu, Y.; Luckyanova, M. N.; Maznev, A. A.; Huberman, S.; Chiloyan, V.; Zhou, J.; Huang, X.; Nelson, K. A. Measuring Phonon Mean Free Path Distributions by Probing Quasiballistic Phonon Transport in Grating Nanostructures. *Scientific Reports* 5, 17131 (2015).

(127) Chen, G. *Nanoscale Energy Transport and Conversion: A Parallel Treatment of Electrons, Molecules, Phonons, and Photons*; Oxford University Press, 2005.

(128) Dove, M. T.; Dove, M. T. *Introduction to Lattice Dynamics*; Cambridge university press, 1993; Vol. 4.

(129) Reddy, P.; Castelino, K.; Majumdar, A. Diffuse Mismatch Model of Thermal Boundary Conductance Using Exact Phonon Dispersion. *Applied Physics Letters* 87, 211908 (2005).

(130) Chen, Z.; Wei, Z.; Chen, Y.; Dames, C. Anisotropic Debye Model for the Thermal Boundary Conductance. *Physical Review B* 87, 125426 (2013).

(131) Baroni, S.; de Gironcoli, S.; Dal Corso, A.; Giannozzi, P. Phonons and Related Crystal Properties from Density-Functional Perturbation Theory. *Reviews of Modern Physics* 73, 515 (2001).

(132) Togo, A.; Tanaka, I. First Principles Phonon Calculations in Materials Science. *Scripta Materialia*, 108, 1 (2015).

(133) Grimme, S. Semiempirical GGA-Type Density Functional Constructed with a Long-Range Dispersion Correction. *Journal of Computational Chemistry* 27, 1787 (2006).

(134) Brown, A.; Rundqvist, S.; IUCr. Refinement of the Crystal Structure of Black Phosphorus. *Acta Crystallographica* 19, 684 (1965).

(135) Davey, W. P. Precision Measurements of the Lattice Constants of Twelve Common Metals. *Physical Review* 25, 753 (1925).

(136) Majumdar, A.; Reddy, P. Role of Electron–Phonon Coupling in Thermal Conductance of Metal–Nonmetal Interfaces. *Applied Physics Letters* 84, 4768 (2004).

(137) Chien, H. C.; Yao, D. J.; Hsu, C. T. Measurement and Evaluation of the Interfacial Thermal Resistance between a Metal and a Dielectric. *Applied Physics Letters* 93, 231910 (2008).

(138) Guo, L.; Hodson, S. L.; Fisher, T. S.; Xu, X. Heat Transfer across Metal-Dielectric Interfaces during Ultrafast-Laser Heating. *Journal of Heat Transfer* 134, 42402 (2012).

(139) Yao, Q.; Guo, L.; Iyer, V.; Xu, X. Ultrafast Electron–Phonon Coupling at Metal-Dielectric Interface. *Heat Transfer Engineering 0*, 1 (2018).

(140) Stedman, R.; Nilsson, G. Dispersion Relations for Phonons in Aluminum at 80 and 300°K. *Physical Review* 145, 492 (1966).

(141) Fujii, Y.; Akahama, Y.; Endo, S.; Narita, S.; Yamada, Y.; Shirane, G. Inelastic Neutron Scattering Study of Acoustic Phonons of Black Phosphorus. *Solid State Communication* 44, 579 (1982).

(142) Zhang, Z.M.; Zhang, Z.M.; Luby. *Nano/microscale heat transfer*; New York: McGraw-Hill, 2007.

(143) Sadasivam, S.; Waghmare, U. V.; Fisher, T. S. Phonon-Eigenspectrum-Based Formulation of the Atomistic Green's Function Method. *Physical Review B* 96, 174302 (2017).

(144) Ong, Z. Y.; Zhang, G. Efficient Approach for Modeling Phonon Transmission Probability in Nanoscale Interfacial Thermal Transport. *Physical Review B*, 91, 174302 (2015).

(145) Giri, A.; Hopkins, P.E. A Review of Experimental and Computational Advances in Thermal Boundary Conductance and Nanoscale Thermal Transport across Solid Interfaces. *Advanced Functional Materials* 30, 1903857 (2020).

(146) Dai, J.; Tian, Z. Rigorous Formalism of Anharmonic Atomistic Green's Function for Three-Dimensional Interfaces. *Physical Review B* 101, 041301 (2020).

(147) Zhou, Y.; Hu, M. Full Quantification of Frequency-Dependent Interfacial Thermal Conductance Contributed by Two- and Three-Phonon Scattering Processes from Nonequilibrium Molecular Dynamics Simulations. *Physical Review B* 95, 115313 (2017).

(148) Jacobsen, K. W.; Norskov, J. K.; Puska, M. J. Interatomic Interactions in the Effective-Medium Theory. *Physical Review B*, 35, 7423 (1987).

(149) Jacobsen, K.W.; Stoltze, P.; Nørskov, J.K. A Semi-Empirical Effective Medium Theory for Metals and Alloys. *Surface Science* 366, 394 (1996).

(150) Jiang, J.-W. Parametrization of Stillinger–Weber Potential Based on Valence Force Field Model: Application to Single-Layer MoS_2 and Black Phosphorus. *Nanotechnology*, 26, 315706 (2015).

(151) Zhang, Y.-Y.; Pei, Q.-X.; Jiang, J.-W.; Wei, N.; Zhang, Y.-W. Thermal Conductivities of Single- and Multi-Layer Phosphorene: A Molecular Dynamics Study. *Nanoscale, 8*, 483 (2016).

(152) Puri, P.; Yang, V. Effect of Particle Size on Melting of Aluminum at Nano Scales. *Journal of Physical Chemistry C 111*, 11776 (2007).

(153) Luo, T.; Lloyd, J. R. Enhancement of Thermal Energy Transport across Graphene/Graphite and Polymer Interfaces: A Molecular Dynamics Study. *Advanced Functional Materials* 22, 2495 (2012).

(154) Reed, M. A.; Zhou, C.; Muller, C. J.; Burgin, T. P.; Tour, J. M. Conductance of a Molecular Junction. *Science* 278, 252 (1997).

(155) Joachim, C.; Gimzewski, J. K.; Aviram, A. Electronics Using Hybrid-Molecular and Mono-Molecular Devices. *Nature 408*, 541 (2000).

(156) Tao, N. J. Electron Transport in Molecular Junctions. *Nature Nanotechnology 1*, 173 (2006).

(157) Coskun, A.; Spruell, J. M.; Barin, G.; Dichtel, W. R.; Flood, A. H.; Botros, Y. Y.; Stoddart, J. F. High Hopes: Can Molecular Electronics Realise Its Potential? *Chemistry Society Reviews* 41, 4827 (2012).

(158) Love, J. C.; Estroff, L. A.; Kriebel, J. K.; Nuzzo, R. G.; Whitesides, G. M. Self-Assembled Monolayers of Thiolates on Metals as a Form of Nanotechnology. *Chemical Reviews* 105, 1103 (2005).

(159) Li, M.; Kang, J. S.; Nguyen, H. D.; Wu, H.; Aoki, T.; Hu, Y. Anisotropic Thermal Boundary Resistance across 2D Black Phosphorus: Experiment and Atomistic Modeling of Interfacial Energy Transport. *Advanced Materials 31*, 1901021 (2019).

(160) Cui, Y.; Li, M.; Hu, Y. Emerging Interface Materials for Electronics Thermal Management: Experiments, Modeling, and New Opportunities. *J Mater Chem C Mater 8*, 10568 (2020).

(161) Cui, Y.; Qin, Z.; Wu, H.; Li, M.; Hu, Y. Flexible Thermal Interface Based on Self-Assembled Boron Arsenide for High-Performance Thermal Management. *Nature Communications 12*, 1284 (2021).

(162) Lindsay, S. M.; Ratner, M. A. Molecular Transport Junctions: Clearing Mists. *Advanced Materials 19*, 23 (2007).

(163) Wang, K.; Meyhofer, E.; Reddy, P. Thermal and Thermoelectric Properties of Molecular Junctions. *Advanced Functional Materials 30*, 1904534 (2019).

(164) Wang, R. Y.; Segalman, R. A.; Majumdar, A. Room Temperature Thermal Conductance of Alkanedithiol Self-Assembled Monolayers. *Applied Physics Letters 89*, 173113 (2006).

(165) Wei, X.; Zhang, T.; Luo, T. Thermal Energy Transport across Hard-Soft Interfaces. *ACS Energy Letters 2*, 2283 (2017).

(166) Ge, Z.; Cahill, D. G.; Braun, P. V. Thermal Conductance of Hydrophilic and Hydrophobic Interfaces. *Physical Review Letters 96*, 186101 (2006).

(167) O'Brien, P. J.; Shenogin, S.; Liu, J.; Chow, P. K.; Laurencin, D.; Mutin, P. H.; Yamaguchi, M.; Keblinski, P.; Ramanath, G. Bonding-Induced Thermal Conductance Enhancement at Inorganic Heterointerfaces Using Nanomolecular Monolayers. *Nature Materials 12*, 118 (2013).

(168) Heimel, G.; Romaner, L.; Zojer, E.; Bredas, J. L. The Interface Energetics of Self-Assembled Monolayers on Metals. *Accounts of Chemical Research 41*, 721 (2008).

(169) Pervushin, K.; Riek, R.; Wider, G.; Wüthrich, K. Attenuated T2 Relaxation by Mutual Cancellation of Dipole-Dipole Coupling and Chemical Shift Anisotropy Indicates an Avenue to NMR Structures of Very Large Biological Macromolecules in Solution. *Proceedings of the National Academy of Sciences 94*, 12366 (1997).

(170) Hol, W. G. J.; Van Duijnen, P. T.; Berendsen, H. J. C. The α-Helix Dipole and the Properties of Proteins. *Nature 273*, 443 (1978).

(171) MacKerell, A. D.; Bashford, D.; Bellott, M.; Dunbrack, R. L.; Evanseck, J. D.; Field, M. J.; Fischer, S.; Gao, J.; Guo, H.; Ha, S.; Joseph-McCarthy, D.; Kuchnir, L.; Kuczera, K.; Lau, F. T. K.; Mattos, C.; Michnick, S.; Ngo, T.; Nguyen, D. T.; Prodhom, B.; Reiher, W. E.; Roux, B.; Schlenkrich, M.; Smith, J. C.; Stote, R.; Straub, J.; Watanabe, M.; Wiórkiewicz-Kuczera, J.; Yin, D.; Karplus, M. All-Atom Empirical Potential for Molecular Modeling and Dynamics Studies of Proteins. *Journal of Physical Chemistry B 102*, 3586 (1998).

(172) Chen, M. M.; Holmes, K. R. Microvascular Contributions in Tissue Heat Transfer. *Annals of the New York Academy of Sciences 335*, 137–150 (1980).

(173) Chin, A. W. H.; Chu, J. T. S.; Perera, M. R. A.; Hui, K. P. Y.; Yen, H.-L.; Chan, M. C. W.; Peiris, M.; Poon, L. L. M. Stability of SARS-CoV-2 in Different Environmental Conditions. *Lancet Microbe 1*, e145 (2020).

(174) Hohman, J. N.; Claridge, S. A.; Kim, M.; Weiss, P. S. Cage Molecules for Self-Assembly. *Materials Science and Engineering R: Reports 70*, 188 (2010).

(175) Hohman, J. N.; Zhang, P.; Morin, E. I.; Han, P.; Kim, M.; Kurland, A. R.; McClanahan, P. D.; Balema, V. P.; Weiss, P. S. Self-Assembly of Carboranethiol Isomers on Au{111}: Intermolecular Interactions Determined by Molecular Dipole Orientations. *ACS Nano 3*, 527 (2009).

(176) Mete, E.; Yilmaz, A.; Danişman, M. F. A van Der Waals Density Functional Investigation of Carboranethiol Self-Assembled Monolayers on Au(111). *Physical Chemistry Chemical Physics 18*, 12920 (2016).

(177) Li, M.; Li, C.; Wang, J.; Xiao, X.; Yue, Y. Parallel Measurement of Conductive and Convective Thermal Transport of Micro/Nanowires Based on Raman Mapping. *Applied Physics Letters 106*, 253108 (2015).

(178) Kang, J. S.; Wu, H.; Li, M.; Hu, Y. Intrinsic Low Thermal Conductivity and Phonon Renormalization Due to Strong Anharmonicity of Single-Crystal Tin Selenide. *Nano Letters 19*, 4941 (2019).

(179) Foiles, S. M.; Baskes, M. I.; Daw, M. S. Embedded-Atom-Method Functions for the Fcc Metals Cu, Ag, Au, Ni, Pd, Pt, and Their Alloys. *Physical Review B 33*, 7983 (1986).

(180) Timofeeva, T. V.; Suponitsky, K. Y.; Yanovsky, A. I.; Allinger, N. L. The MM3 Force Field for 12-Vertex Boranes and Carboranes. *Journal of organometallic chemistry*, *536*, 481 (1997).

(181) Berendsen, H. J. C.; Grigera, J. R.; Straatsma, T. P. The Missing Term in Effective Pair Potentials. *Journal of Physical Chemistry 91*, 6269 (1987).

(182) Jorgensen, W. L.; Maxwell, D. S.; Tirado-Rives, J. Development and Testing of the OPLS All-Atom Force Field on Conformational Energetics and Properties of Organic Liquids. *Journal of American Chemistry Society 118*, 11225 (1996).

(183) Canongia Lopes, J. N.; Deschamps, J.; Pádua, A. A. H. Modeling Ionic Liquids Using a Systematic All-Atom Force Field. *Journal of Physical Chemistry B* **2004**, *108*, 2038–2047.

(184) Plimpton, S. Fast Parallel Algorithms for Short-Range Molecular Dynamics. *Journal of Computational Physics 117*, 1 (1995).

(185) Aizcorbe, A. Moore's Law, Competition, and Intel's Productivity in the Mid-1990s. *American Economic Review 95*, 305 (2005).

(186) Qin, Z.; Li, M.; Flohn, J.; Hu, Y. Thermal management materials for energy-efficient and sustainable future buildings. Chemical Communications *57*, 12236 (2022).

(187) Arden, W.M. The International Technology Roadmap for Semiconductors—Perspectives and Challenges for the Next 15 Years. *Current Opinion in Solid State and Materials Science* 6, 371 (2002).

(188) Bubnova, O. Thermal Release. *Nature Nanotechnology 13*, 620 (2018).

(189) Protik, N.H.; Carrete, J.; Katcho, N.A.; Mingo, N.; Broido, D. Ab Initio Study of the Effect of Vacancies on the Thermal Conductivity of Boron Arsenide. *Physical Review B 94*, 045207 (2016).

(190) Broido, D. A.; Lindsay, L.; Reinecke, T. L. Ab Initio Study of the Unusual Thermal Transport Properties of Boron Arsenide and Related Materials. *Physical Review B 88*, 214303 (2013).

(191) Mingo, N.; Broido, D. A. Lattice Thermal Conductivity Crossovers in Semiconductor Nanowires. *Physical Review Letters*, *93*, 246106 (2004).

(192) Feng, T.; Lindsay, L.; Ruan, X. Four-Phonon Scattering Significantly Reduces Intrinsic Thermal Conductivity of Solids. *Physical Review B*, *96*, 161201 (2017).

(193) Ward, A.; Broido, D. A.; Stewart, D. A.; Deinzer, G. Ab Initio Theory of the Lattice Thermal Conductivity in Diamond. *Physical Review B 80*, 125203 (2009).

(194) Lindsay, L. First Principles Peierls-Boltzmann Phonon Thermal Transport: A Topical Review. *Nanoscale and Microscale Thermophysical Engineering* 20, 67 (2016).

(195) Zeng, L.; Collins, K.C.; Hu, Y.; Luckyanova, M.N.; Maznev, A.A.; Huberman, S.; Chiloyan, V.; Zhou, J.; Huang, X.; Nelson, K.A.; Chen, G. Measuring Phonon Mean Free Path Distributions by Probing Quasiballistic Phonon Transport in Grating Nanostructures. *Scientific Reports 5*, 1 (2015).

(196) Fan, H.; Wu, H.; Lindsay, L.; Hu, Y. Ab Initio Investigation of Single-Layer High Thermal Conductivity Boron Compounds. *Physical Review B* 100, 85420 (2019).

(197) Dames, C. Ultrahigh Thermal Conductivity Confirmed in Boron Arsenide. *Science* 361, 549 (2018).

(198) Chen, K.; Song, B.; Ravichandran, N.K.; Zheng, Q.; Chen, X.; Lee, H.; Sun, H.; Li, S.; Udalamatta Gamage, G.A.G.; Tian, F.; Ding, Z. Ultrahigh Thermal Conductivity in Isotope-Enriched Cubic Boron Nitride. *Science* 367, 555 (2020).

(199) Zheng, Q.; Li, S.; Li, C.; Lv, Y.; Liu, X.; Huang, P.Y.; Broido, D.A.; Lv, B.; Cahill, D.G. High Thermal Conductivity in Isotopically Enriched Cubic Boron Phosphide. *Advanced Functional Materials* 28, 1805116 (2018).

(200) Woo, K.; Lee, K.; Kovnir, K. BP: Synthesis and Properties of Boron Phosphide. *Materials Research Express* 3, 074003 (2016).

(201) Kang, J. S.; Li, M.; Wu, H.; Nguyen, H.; Hu, Y. Basic Physical Properties of Cubic Boron Arsenide. *Applied Physics Letters* 115, 122103 (2019).

(202) Li, M.; Kang, J. S.; Hu, Y. Anisotropic Thermal Boundary Resistance across 2D Black Phosphorus: Experiment and Atomistic Modeling of Interfacial Energy Transport. *Advanced Materials* 31, 1901021 (2019).

(203) Zhang, Y.; Ma, J.; Wei, N.; Yang, J.; Pei, Q.X. Recent Progress in the Development of Thermal Interface Materials: A Review. *Physical Chemistry Chemical Physics* 23 753 (2021).

(204) Gmelin, E.; Asen-Palmer, M.; Reuther, M.; Villar, R. Thermal Boundary Resistance of Mechanical Contacts between Solids at Sub-Ambient Temperatures. *Reviews of Modern Physic Journal of Physics D: Applied Physics*, 32, R19 (1999).

(205) Ziman, J. M. *Electrons and Phonons: The Theory of Transport Phenomena in Solids.*; 1960.

(206) Kittel, C. *Introduction to Solid State Physics*; Wiley New York, 1976.

(207) Cho, J.; Li, Z.; Bozorg-Grayeli, E.; Kodama, T.; Francis, D.; Ejeckam, F.; Faili, F.; Asheghi, M.; Goodson, K. E. Improved Thermal Interfaces of GaN-Diamond Composite Substrates

for HEMT Applications. *IEEE Transactions on Components, Packaging and Manufacturing Technology* 3, 79 (2013).

(208) Pomeroy, J. W.; Bernardoni, M.; Dumka, D. C.; Fanning, D. M.; Kuball, M. Low Thermal Resistance GaN-on-Diamond Transistors Characterized by Three-Dimensional Raman Thermography Mapping. *Applied Physics Letters* 104, 083513 (2014).

(209) Liu, D.; Sun, H.; Pomeroy, J. W.; Francis, D.; Faili, F.; Twitchen, D. J.; Kuball, M. GaN-on-Diamond Electronic Device Reliability: Mechanical and Thermo-Mechanical Integrity. *Applied Physics Letters* 107, 251902 (2015).

(210) Liu, F.; Parajuli, P.; Rao, R.; Wei, P.C.; Karunarathne, A.; Bhattacharya, S.; Podila, R.; He, J.; Maruyama, B.; Priyadarshan, G.; Gladden, J.R. Phonon Anharmonicity in Single-Crystalline SnSe. *Physical Review B* 98, 224309 (2018).

(211) Marszewski, M.; King, S.C.; Galy, T.; Kashanchi, G.N.; Dashti, A.; Yan, Y.; Li, M.; Butts, D.M.; McNeil, P.E.; Lan, E.; Dunn, B. Transparent Silica Aerogel Slabs Synthesized from Nanoparticle Colloidal Suspensions at Near Ambient Conditions on Omniphobic Liquid Substrates. *Journal of Colloid and Interface Science* 606, 884 (2022).

(212) Stoner, R. J.; Maris, H. J.; Anthony, T. R.; Banholzer, W. F. Measurements of the Kapitza Conductance between Diamond and Several Metals. *Physical Review Letters*, 68, 1563 (1992).

(213) Chen, J.; Xu, X.; Zhou, J.; Li, B. Interfacial Thermal Resistance: Past, Present, and Future: Reviews of Modern Physics 94, 025002 (2022).

(214) Giannozzi, P.; Baroni, S.; Bonini, N.; Calandra, M.; Car, R.; Cavazzoni, C.; Ceresoli, D.; Chiarotti, G. L.; Cococcioni, M.; Dabo, I.; Dal Corso, A.; De Gironcoli, S.; Fabris, S.; Fratesi, G.; Gebauer, R.; Gerstmann, U.; Gougoussis, C.; Kokalj, A.; Lazzeri, M.; Martin-Samos, L.; Marzari, N.; Mauri, F.; Mazzarello, R.; Paolini, S.; Pasquarello, A.; Paulatto, L.; Sbraccia, C.; Scandolo, S.; Sclauzero, G.; Seitsonen, A. P.; Smogunov, A.; Umari, P.; Wentzcovitch, R. M. QUANTUM ESPRESSO: A Modular and Open-Source Software Project for Quantum Simulations of Materials. *Journal of Physics Condensed Matter* 21, 395502 (2019).

(215) Stedman, R.; Almqvist, L.; Nilsson, G. Phonon-Frequency Distributions and Heat Capacities of Aluminum and Lead. *Physical Review* 162,549 (1967).

(216) Sharma, P. K.; Singh, N. Phonon Dispersion in Noble Metals. *Physical Review B* 4, 4636 (1971).

(217) Dutton, D. H.; Brockhouse, B. N.; Miller, A. P. Crystal Dynamics of Platinum by Inelastic Neutron Scattering. *Canadian Journal of Physics* 50, 2915 (1972).

(218) Aggarwal, K. G. Lattice Dynamics of Diamond. *Proceedings of the Physical Society* 91, 381 (1967).

(219) Landauer, R. Spatial Variation of Currents and Fields Due to Localized Scatterers in Metallic Conduction. *IBM Journal of Research and Development* 44, 251 (2000).

(220) Ḃttiker, M.; Imry, Y.; Landauer, R.; Pinhas, S. Generalized Many-Channel Conductance Formula with Application to Small Rings. *Physical Review B* 31, 6207 (1985).

(221) Snyder, N. S. Heat Transport through Helium II: Kapitza Conductance. *Cryogenics* 10, 89 (1970).

(222) Kaviany, M. *Heat Transfer Physics*; Cambridge University Press, 2014.

(223) Brommer, P.; Kiselev, A.; Schopf, D.; Beck, P.; Roth, J.; Trebin, H. R. Classical Interaction Potentials for Diverse Materials from Ab Initio Data: A Review of Potfit. *Modelling and Simulation in Materials Science and Engineering* 23, 074002 (2015).

(224) Erhart, P.; Albe, K. Analytical Potential for Atomistic Simulations of Silicon, Carbon, and Silicon Carbide. *Physical Review B* 71, 035211 (2005).

(225) Daw, M.S. Model of Metallic Cohesion: The Embedded-Atom Method. *Physical Review B* 39, 7441 (1989).

(226) Delhommelle, J.; Millié, P. Inadequacy of the Lorentz-Berthelot Combining Rules for Accurate Predictions of Equilibrium Properties by Molecular Simulation. *Molecular Physics* 99, 619 (2001).

(227) Rappé, A. K.; Casewit, C. J.; Colwell, K. S.; Goddard, W. A.; Skiff, W. M. UFF, a Full Periodic Table Force Field for Molecular Mechanics and Molecular Dynamics Simulations. *Journal of American Chemistry Society* 114, 10024 (1992).

(228) Pinches, M.R.S.; Tildesley, D.J.; Smith, W. Large Scale Molecular Dynamics on Parallel Computers using the Link-Cell Algorithm. *Molecular Simulation* 6, 51 (1991).

(229) Ayers, J. E. *Heteroepitaxy of Semiconductors: Theory, Growth, and Characterization*; CRC Press, New York, 2007.

(230) Hu, Y.; Kuemmeth, F.; Lieber, C. M.; Marcus, C. M. Hole Spin Relaxation in Ge-Si Core-Shell Nanowire Qubits. *Nature Nanotechnology* 7, 47 (2012).

(231) Péraud, J.-P. M.; Hadjiconstantinou, N. G. An Alternative Approach to Efficient Simulation of Micro/Nanoscale Phonon Transport. *Applied Physics Letters* 101, 153114 (2012).

(232) United States Department of Energy. *Insulation Materials*. https://www.energy.gov/energysaver/weatherize/insulation/insulation-materials.

(233) Jelle, B. P. Traditional, State-of-the-Art and Future Thermal Building Insulation Materials and Solutions - Properties, Requirements and Possibilities. *Energy and Buildings* 43, 2549 (2011).

(234) Papadopoulos, A. M. State of the Art in Thermal Insulation Materials and Aims for Future Developments. *Energy and Building* 37, 77 (2005).

(235) Kistler, S. S. Coherent Expanded Aerogels and Jellies. *Nature* 127, 741 (1931).

(236) Lu, X., Arduini-Schuster, M. C., Kuhn, J., Nilsson, O., Fricke, J., & Pekala, R. W. Thermal Conductivity of Monolithic Organic Aerogels. *Science* 255 5047 (1992).

(237) Mohanan, J. L.; Arachchige, I. U.; Brock, S. L. Porous Semiconductor Chalcogenide Aerogels. *Science*, 307, 397 (2005).

(238) Qian, F.; Lan, P. C.; Freyman, M. C.; Chen, W.; Kou, T.; Olson, T. Y.; Zhu, C.; Worsley, M. A.; Duoss, E. B.; Spadaccini, C. M.; Baumann, T.; Han, T. Y. J. Ultralight Conductive Silver Nanowire Aerogels. *Nano Letters* 17, 7171 (2017).

(239) Guo, F.; Jiang, Y.; Xu, Z.; Xiao, Y.; Fang, B.; Liu, Y.; Gao, W.; Zhao, P.; Wang, H.; Gao, C. Highly Stretchable Carbon Aerogels. *Nature Communications* 9, 881 (2018).

(240) Jung, S. M.; Jung, H. Y.; Dresselhaus, M. S.; Jung, Y. J.; Kong, J. A Facile Route for 3D Aerogels from Nanostructured 1D and 2D Materials. *Scientific Report* 2, 849 (2012).

(241) Bryning, M. B.; Milkie, D. E.; Islam, M. F.; Hough, L. A.; Kikkawa, J. M.; Yodh, A. G. Carbon Nanotube Aerogels. *Advanced Materials*, 19, 661 (2017).

(242) Sun, H.; Xu, Z.; Gao, C. Multifunctional, Ultra-Flyweight, Synergistically Assembled Carbon Aerogels. *Advanced Materials* 25, 2554 (2013).

(243) Cao, A. Super-Compressible Foamlike Carbon Nanotube Films. *Science* 310, 1307 (2005).

(244) Chen, Z.; Ren, W.; Gao, L.; Liu, B.; Pei, S.; Cheng, H. M. Three-Dimensional Flexible and Conductive Interconnected Graphene Networks Grown by Chemical Vapour Deposition. *Nature Materials* 10, 424 (2011).

(245) Nardecchia, S.; Carriazo, D.; Ferrer, M. L.; Gutiérrez, M. C.; del Monte, F. Three Dimensional Macroporous Architectures and Aerogels Built of Carbon Nanotubes and/or Graphene: Synthesis and Applications. *Chemical Society Reviews* 42, 794 (2013).

(246) Wei, T. Y.; Chang, T. F.; Lu, S. Y.; Chang, Y. C. Preparation of Monolithic Silica Aerogel of Low Thermal Conductivity by Ambient Pressure Drying. *Journal of the American Ceramic Society* 90, 2003 (2007).

(247) Assael, M. J.; Antoniadis, K. D.; Wakeham, W. A. Historical Evolution of the Transient Hot-Wire Technique. *International Journal of Thermophysics* 31, 1051 (2010).

(248) Wen, D.; Ding, Y. Effective Thermal Conductivity of Aqueous Suspensions of Carbon Nanotubes (Carbon Nanotube Nanofluids). *Journal of Thermophysics and Heat Transfer* 18, 481 (2004).

(249) Healy, J. J.; De Groot, J. J.; Kestin, J. The Theory of the Transient Hot-Wire Method for Measuring Thermal Conductivity. *Physica B+ C* 82 392 (1976).

(250) Wei, L. C.; Ehrlich, L. E.; Powell-Palm, M. J.; Montgomery, C.; Beuth, J.; Malen, J. A. Thermal Conductivity of Metal Powders for Powder Bed Additive Manufacturing. *Additive Manufacturing* 21, 201 (2018).

(251) Zheng, R.; Gao, J.; Wang, J.; Chen, G. Reversible Temperature Regulation of Electrical and Thermal Conductivity Using Liquid–Solid Phase Transitions. *Nat Communications* 2, 289 (2011).

(252) Stops, D. W. Effect of Temperature Upon the Thermal Conductivity of Gases. *Nature* 164, 966 (1949).

(253) Zhao, D.; Qian, X.; Gu, X.; Jajja, S. A.; Yang, R. Measurement Techniques for Thermal Conductivity and Interfacial Thermal Conductance of Bulk and Thin Film Materials. *Journal of Electronic Packaging* 138, 040802 (2016).

(254) Cohen, E.; Glicksman, L. Analysis of the Transient Hot-Wire Method to Measure Thermal Conductivity of Silica Aerogel: Influence of Wire Length, and Radiation Properties. *J Heat Transfer* 136, 41301 (2014).

(255) Eiermann, K.; Hellwege, K. Thermal Conductivity of High Polymers From− 180° C. to 90° C. *Journal of Polymer Science* 57, 99 (1962).

(256) Montgomery, R. B. Viscosity and Thermal Conductivity of Air and Diffusivity of Water Vapor in Air. *Journal of Meteorology* 4, 193 (1947).

(257) Hrubesh, L. W.; Pekala, R. W. Thermal Properties of Organic and Inorganic Aerogels. *Journal of Materials Research* 9, 731 (1994).

(258) Hopkins, P. E.; Kaehr, B.; Piekos, E. S.; Dunphy, D.; Jeffrey Brinker, C. Minimum Thermal Conductivity Considerations in Aerogel Thin Films. *Journal of Applied Physics* 111, 113532 (2012).

(259) Lu, X.; Wang, P.; Arduini-Schuster, M. C.; Kuhn, J.; Büttner, D.; Nilsson, O.; Heinemann, U.; Fricke, J. Thermal Transport in Organic and Opacified Silica Monolithic Aerogels. *Journal of Non-Crystalline Solids* 145, 207 (1992).

(260) Tang, G. H.; Bi, C.; Zhao, Y.; Tao, W. Q. Thermal Transport in Nano-Porous Insulation of Aerogel: Factors, Models and Outlook. *Energy* 90, 701 (2015).

(261) Woodside, W.; Messmer, J. H. Thermal Conductivity of Porous Media. I. Unconsolidated Sands. *Journal of Applied Physics* 32, 1688 (1961).

(262) Drelich, J.; Chibowski, E.; Meng, D. D.; Terpilowski, K. Hydrophilic and Superhydrophilic Surfaces and Materials. *Soft Matter* 7, 9804 (2011).

(263) Koch, K.; Barthlott, W. Superhydrophobic and Superhydrophilic Plant Surfaces: An Inspiration for Biomimetic Materials. *Philosophical Transactions of the Royal Society of London A: Mathematical, Physical and Engineering Sciences* 367, 1487 (2009).

(264) Karapanagiotis, I.; Manoudis, P. N.; Zurba, A.; Lampakis, D. From Hydrophobic to Superhydrophobic and Superhydrophilic Siloxanes by Thermal Treatment. *Langmuir* 30, 13235 (2014).

(265) Drelich, J.; Marmur, A. Physics and Applications of Superhydrophobic and Superhydrophilic Surfaces and Coatings. *Surface Innovations* 2, 211 (2014).

(266) Darmanin, T.; Guittard, F. Superhydrophobic and Superoleophobic Properties in Nature. *Materials Today* 18, 273 (2015).

(267) Yao, X.; Gao, J.; Song, Y.; Jiang, L. Superoleophobic Surfaces with Controllable Oil Adhesion and Their Application in Oil Transportation. *Advanced Functional Materirals* 21, 4270 (2011).

(268) Liu, T.; Kim, C.-J. Turning a Surface Superrepellent Even to Completely Wetting Liquids. *Science* 346, 1096 (2014).

(269) Wong, T. S.; Kang, S. H.; Tang, S. K. Y.; Smythe, E. J.; Hatton, B. D.; Grinthal, A.; Aizenberg, J. Bioinspired Self-Repairing Slippery Surfaces with Pressure-Stable Omniphobicity. *Nature* 477, 7365 (2011).

(270) Cassie, A. B. D.; Baxter, S. Wettability of Porous Surfaces. *Transactions of the Faraday Society* 40, 546 (1944).

(271) Wenzel, R. N. Resistance of Solid Surfaces to Wetting by Water. *Industrial & Engineering Chemistry* 28, 988 (1936).

(272) Bormashenko, E. Progress in Understanding Wetting Transitions on Rough Surfaces. *Advances in Colloid Interface Science* 222, 92 (2015).

(273) Doshi, D. A.; Shah, P. B.; Singh, S.; Branson, E. D.; Malanoski, A. P.; Watkins, E. B.; Majewski, J.; van Swol, F.; Brinker, C. J. Investigating the Interface of Superhydrophobic Surfaces in Contact with Water. *Langmuir* 21, 7805 (2005).

(274) Smirnova, I.; Mamic, J.; Arlt, W. Adsorption of Drugs on Silica Aerogels. *Langmuir* 19, 8521 (2003).

(275) Lendlein, A.; Langer, R. Biodegradable, Elastic Shape-Memory Polymers for Potential Biomedical Applications. *Science* 296, 1673 (2002).

(276) Ge, J.; Shi, L.-A.; Wang, Y.-C.; Zhao, H.-Y.; Yao, H.-B.; Zhu, Y.-B.; Zhang, Y.; Zhu, H.-W.; Wu, H.-A.; Yu, S.-H. Joule-Heated Graphene-Wrapped Sponge Enables Fast Clean-up of Viscous Crude-Oil Spill. *Nature Nanotechnology* 12, 434 (2017).

(277) Thekdi, A.; Nimbalkar, S. U. *Industrial Waste Heat Recovery-Potential Applications, Available Technologies and Crosscutting R&d Opportunities*; Oak Ridge National Lab.(ORNL), Oak Ridge, TN (United States), 2015.

(278) Koumoto, K.; Terasaki, I.; Funahashi, R. Complex Oxide Materials for Potential Thermoelectric Applications. *MRS bulletin* 31, 206 (2006).

(279) Yang, J.; Caillat, T. Thermoelectric Materials for Space and Automotive Power Generation. *MRS Bulletin* 31, 224 (2006).

(280) Zhang, X.; Zhao, L.D. Thermoelectric Materials: Energy Conversion between Heat and Electricity. *Journal of Materiomics* 1, 92 (2015).

(281) Christensen, M.; Johnsen, S.; Iversen, B. B. Thermoelectric Clathrates of Type I. *Dalton transactions* 39, 978 (2010).

(282) Meng, X.; Liu, Z.; Cui, B.; Qin, D.; Geng, H.; Cai, W.; Fu, L.; He, J.; Ren, Z.; Sui, J. Grain Boundary Engineering for Achieving High Thermoelectric Performance in N-type Skutterudites. *Advanced Energy Materials* 7, 1602582 (2017).

(283) Lin, Z.; Hollar, C.; Kang, J. S.; Yin, A.; Wang, Y.; Shiu, H.; Huang, Y.; Hu, Y.; Zhang, Y.; Duan, X. A Solution Processable High-performance Thermoelectric Copper Selenide Thin Film. *Advanced Materials* 29, 1606662 (2017).

(284) Yang, L.; Chen, Z.; Dargusch, M. S.; Zou, J. High Performance Thermoelectric Materials: Progress and Their Applications. *Advanced Energy Materials* 8, 1701797 (2018).

(285) Sootsman, J. R.; Chung, D. Y.; Kanatzidis, M. G. New and Old Concepts in Thermoelectric Materials.. *Angewandte Chemie International Edition* 48, 8616 (2009).

(286) Zhao, L.-D.; Chang, C.; Tan, G.; Kanatzidis, M. G. SnSe: A Remarkable New Thermoelectric Material. *Energy and Environmental Science* 9, 3044 (2016).

(287) Zhao, L.-D. D.; Tan, G.; Hao, S.; He, J.; Pei, Y.; Chi, H.; Wang, H.; Gong, S.; Xu, H.; Dravid, V. P.; Uher, C.; Snyder, G. J.; Wolverton, C.; Kanatzidis, M. G. Ultrahigh Power Factor and Thermoelectric Performance in Hole-Doped Single-Crystal SnSe. *Science*, 351, 141 (2016)

(288) Kestin, J.; Wakeham, W.A. A Contribution to the Theory of the Transient Hot-Wire Technique for Thermal Conductivity Measurements. *Physica A: Statistical Mechanics and its Applications* 92, 102 (1978).

(289) Li, M.; Qin, Z.; Cui, Y.; Yang, C.; Deng, C.; Wang, Y.; Kang, J. S.; Xia, H.; Hu, Y. Ultralight and Flexible Monolithic Polymer Aerogel with Extraordinary Thermal Insulation by A Facile Ambient Process. *Advanced Mater Interfaces* 6 1900314 (2019).

(290) Andersson, P.; Bäckström, G. Thermal Conductivity of Solids under Pressure by The Transient Hot Wire Method. *Review of Scientific Instruments* 47, 205 (1976).

(291) Zahid, F.; Lake, R. Thermoelectric Properties of Bi_2Te_3 Atomic Quintuple Thin Films. *Applied Physics Letters* 97, 212102 (2010).

(292) Kim, S. il; Lee, K. H.; Mun, H. A.; Kim, H. S.; Hwang, S. W.; Roh, J. W.; Yang, D. J.; Shin, W. H.; Li, X. S.; Lee, Y. H. Dense Dislocation Arrays Embedded in Grain Boundaries for High-Performance Bulk Thermoelectrics. *Science* 348, 109–114 (2015).

(293) Yu, J. K.; Mitrovic, S.; Tham, D.; Varghese, J.; Heath, J. R. Reduction of Thermal Conductivity in Phononic Nanomesh Structures. *Nature Nanotechnology* 5, 718 (2010).

(294) Poudel, B.; Hao, Q.; Ma, Y.; Lan, Y.; Minnich, A.; Yu, B.; Yan, X.; Wang, D.; Muto, A.; Vashaee, D.; Chen, X.; Liu, J.; Dresselhaus, M. S.; Chen, G.; Ren, Z. High-Thermoelectric Performance of Nanostructured Bismuth Antimony Telluride Bulk Alloys. *Science* 320, 634 (2008).

(295) Zhao, L.D.; Wu, H.J.; Hao, S.Q.; Wu, C.I.; Zhou, X.Y.; Biswas, K.; He, J.Q.; Hogan, T.P.; Uher, C.; Wolverton, C.; Dravid, V.P. All-Scale Hierarchical Thermoelectrics: MgTe in PbTe Facilitates Valence Band Convergence and Suppresses Bipolar Thermal Transport for High Performance. *Energy & Environmental Science* 6, 3346 (2013).

(296) Tang, F.; Li, L.; Chen, D. Mesoporous Silica Nanoparticles: Synthesis, Biocompatibility and Drug Delivery. *Advanced Materials* 24, 1504 (2012).

(297) Daiguji, H.; Hwang, J.; Takahashi, A.; Kataoka, S.; Endo, A. Ion Transport in Mesoporous Silica SBA-16 Thin Films with 3D Cubic Structures. *Langmuir* 28, 3671 (2012).

(298) Hwang, J.; Daiguji, H. Proton Transport in Mesoporous Silica SBA-16 Thin Films with Three-Dimensional Cubic Structures. *Langmuir* 29, 2406 (2013).

(299) Hwang, J.; Kataoka, S.; Endo, A.; Daiguji, H. Enhanced Energy Harvesting by Concentration Gradient-Driven Ion Transport in SBA-15 Mesoporous Silica Thin Films. *Lab Chip* 16, 3824 (2016).

(300) Liu, C.; Guo, J.; Yang, W.; Hu, J.; Wang, C.; Fu, S. Magnetic Mesoporous Silica Microspheres with Thermo-Sensitive Polymer Shell for Controlled Drug Release. *Journal of Material Chemistry* 19, 4764 (2009).

(301) Chung, P. W.; Kumar, R.; Pruski, M.; Lin, V. S. Y. Temperature Responsive Solution Partition of Organic-Inorganic Hybrid Poly(N-Isopropylacrylamide)-Coated Mesoporous Silica Nanospheres. *Advanced Functional Materials* 18, 1390 (2008).

(302) Choi, S. G.; Ha, T. J.; Yu, B. G.; Jaung, S. P.; Kwon, O.; Park, H. H. Improvement of Uncooled Infrared Imaging Detector by Using Mesoporous Silica as a Thermal Isolation Layer. *Ceramics International* 34, 833 (2008).

(303) Hu, C.; Morgen, M.; Ho, P. S.; Jain, A.; Gill, W. N.; Plawsky, J. L.; Wayner, P. C. Thermal Conductivity Study of Porous Low-k Dielectric Materials. *Applied Physics Letters* 77, 145 (2000).

(304) Chen, H.; Ginzburg, V.V.; Yang, J.; Yang, Y.; Liu, W.; Huang, Y.; Du, L; Chen, B.A. Thermal Conductivity of Polymer-Based Composites: Fundamentals and Applications. Progress in Polymer Science 59, 41 (2016).

(305) Costescu, R. M.; Bullen, A. J.; Matamis, G.; O'Hara, K. E.; Cahill, D. G. Thermal Conductivity and Sound Velocities of Hydrogen-Silsesquioxane Low-k Dielectrics. *Physical Review B* 65, 942051 (2002).

(306) Cuce, E.; Cuce, P.M.; Wood, C.J.; Riffat, S.B. Toward Aerogel based Thermal Superinsulation in Buildings: A Comprehensive Review. *Renewable and Sustainable Energy Reviews* 34, 273 (2014).

(307) Song, D.; Chen, G. Thermal Conductivity of Periodic Microporous Silicon Films. *Applied Physics Letters* 84, 687 (2004).

(308) Seol, J. H.; Barth, D. S.; Zhu, J.; Ćoso, D.; Hippalgaonkar, K.; Lim, J.; Han, J.; Zhang, X.; Majumdar, A. Tunable Thermal Conductivity in Mesoporous Silicon by Slight Porosity Change. *Applied Physics Letters* 111, 3164 (2017).

(309) Fang, J.; Pilon, L. Scaling Laws for Thermal Conductivity of Crystalline Nanoporous Silicon Based on Molecular Dynamics Simulations. *Journal of Applied Physics 110*, 064305 (2011).

(310) Cahill, D. G.; Watson, S. K.; Pohl, R. O. Lower Limit to the Thermal Conductivity of Disordered Crystals. *Physical Review B 46*, 6131 (1992).

(311) Kittel, C. Interpretation of the Thermal Conductivity of Glasses. *Physical Review 75*, 972 (1949).

(312) Larkin, J. M.; McGaughey, A. J. H. Thermal Conductivity Accumulation in Amorphous Silica and Amorphous Silicon. *Physical Review B* 89, 144303 (2014).

(313) Yang, L.; Zhang, Q.; Cui, Z.; Gerboth, M.; Zhao, Y.; Xu, T. T.; Walker, D. G.; Li, D. Ballistic Phonon Penetration Depth in Amorphous Silicon Dioxide. *Nano Letters*, 17, 7218 (2017).

(314) Wingert, M. C.; Zheng, J.; Kwon, S.; Chen, R. Thermal Transport in Amorphous Materials: A Review. *Semiconductor Science and Technology* 31, 3003 (2016).

(315) Tolbert, S. H. Mesoporous Silica: Holey Quasicrystals. *Nature Materials* 11, 749 (2012).

(316) Coquil, T.; Reitz, C.; Brezesinski, T.; Nemanick, E. J.; Tolbert, S. H.; Pilon, L. Thermal Conductivity of Ordered Mesoporous Titania Films Made from Nanocrystalline Building Blocks and Sol−Gel Reagents. *The Journal of Physical Chemistry C* 114, 12451 (2010).

(317) Marszewski, M.; Butts, D.; Lan, E.; Yan, Y.; King, S. C.; McNeil, P. E.; Galy, T.; Dunn, B.; Tolbert, S. H.; Hu, Y. Effect of Surface Hydroxyl Groups on Heat Capacity of Mesoporous Silica. *Applied Physics Letters* 112, 201903 (2018).

(318) Membreno, D.; Smith, L.; Dunn, B. Silica Sol-Gel Chemistry: Creating Materials and Architectures for Energy Generation and Storage. *Journal of Solgel Science and Technology* 70, 203 (2014).

(319) Venkateswara Rao, A.; Bhagat, S. D.; Hirashima, H.; Pajonk, G. M. Synthesis of Flexible Silica Aerogels Using Methyltrimethoxysilane (MTMS) Precursor. *Journal of Colloidal Interface Science* 300, 279 (2006).

(320) W., S. D.; Keefer, K. D.; Schaefer, D. W.; Keefer, K. D.; W., S. D.; Keefer, K. D. Structure of Random Porous Materials: Silica Aerogel. *Physical Review Letters* 56, 2199 (1986).

(321) Kruk, M.; Jaroniec, M.; Sayari, A. Application of Large Pore MCM-41 Molecular Sieves To Improve Pore Size Analysis Using Nitrogen Adsorption Measurements. *Langmuir* **1997**, *13*, 6267–6273.

(322) Barrett, E. P.; Joyner, L. G.; Halenda, P. P. The Determination of Pore Volume and Area Distributions in Porous Substances. I. Computations from Nitrogen Isotherms. *Journal of American Chemistry Society*, 73, 373 (1951).

(323) Jain, A.; Rogojevic, S.; Ponoth, S.; Gill, W.N.; Plawsky, J.L.; Simonyi, E.; Chen, S.T.; Ho, P.S. Processing Dependent Thermal Conductivity of Nanoporous Silica Xerogel Films. *Journal of Applied Physics* 91, 3275 (2002).

(324) Talebian, E.; Talebian, M. A General Review on the Derivation of Clausius-Mossotti Relation. *Optik (Stuttg)* 124, 2324 (2013).

(325) Norris, A. N.; Callegari, A. J.; Sheng, P. A Generalized Differential Effective Medium Theory. *Journal of the Mechanics and Physics of Solids* 33, 525 (1985).

(326) Russell, H. W. Principles of Heat Flow in Porous Insulators. *Journal of the American Ceramic Society* 18, 1 (1935).

(327) Zeng, S.Q.; Hunt, A.; Greif, R. Theoretical Modeling of Carbon Content to Minimize Heat Transfer in Silica Aerogel. *Journal of Non-Crystalline Solids* 186, 271 (1995).

(328) Anderson, O.L. The Debye Temperature of Vitreous Silica. *Journal of Physics and Chemistry of Solids*, 12, 41 (1959).

(329) Goodson, K. E.; Filk, M. I.; Su, L. T.; Antoniadis, D. A. Prediction and Measurement of the Thermal Conductivity of Amorphous Dielectric Layers. *Journal of Physics D: Applied Physics* 116, 317 (1994).

(330) Kwon, S.; Zheng, J.; Wingert, M.C.; Cui, S.; Chen, R. Unusually High and Anisotropic Thermal Conductivity in Amorphous Silicon Nanostructures. *ACS nano* 11, 2470 (2017).

(331) Allen, P. B.; Feldman, J. L. Thermal Conductivity of Disordered Harmonic Solids. *Physical Review B* 48, 12581 (1993).

(332) Seyf, H. R.; Yates, L.; Bougher, T. L.; Graham, S.; Cola, B. A.; Detchprohm, T.; Ji, M. H.; Kim, J.; Dupuis, R.; Lv, W.; Henry, A. Rethinking Phonons: The Issue of Disorder. *NPJ Computational Materials* 3, 49 (2017).

(333) Dietler, G.; Aubert, C.; Cannell, D. S.; Wiltzius, P. Gelation of Colloidal Silica. *Physical Review Letters 57*, 3117 (1986).

(334) Scott, G. D.; Kilgour, D. M. The Density of Random Close Packing of Spheres. *Journal of Physics D: Applied Physics* 2, 863 (1969).

(335) Progelhof, R. C.; Throne, J. L.; Ruetsch, R. R. Methods for Predicting the Thermal Conductivity of Composite Systems: A Review. *Polymer Engineering Science* 16, 615 (1976).

(336) Chen, G. Nonlocal and Nonequilibrium Heat Conduction in the Vicinity of Nanoparticles. *Journal of Heat Transfer* 118, 539 (1996).

(337) Majumdar, A. Microscale Heat Conduction in Dielectric Thin Films. *Journal of Heat Transfer* 115, 7 (2008).

(338) Alam, M.T.; Pulavarthy, R.A.; Bielefeld, J.; King, S.W.; Haque, M.A. Thermal Conductivity Measurement of Low-K Dielectric Films: Effect of Porosity and Density. *Journal of Electronic Materials* 43, 746 (2014).

(339) Yamane, T.; Nagai, N.; Katayama, S.; Todoki, M. Measurement of Thermal Conductivity of Silicon Dioxide Thin Films Using a 3ω Method. *Journal of Applied Physics* 91, 9772 (2002).

(340) Allen, P. B.; Feldman, J. L.; Fabian, J.; Wooten, F. Diffusons, Locons and Propagons: Character of Atomie Vibrations in Amorphous Si. *Philosophical Magazine B: Physics of*

Condensed Matter; Statistical Mechanics, Electronic, Optical and Magnetic Properties 79, 1715 (1999).

(341) Lee, J.; Lim, J.; Yang, P. Ballistic Phonon Transport in Holey Silicon. *Nano Letters* 15, 3273 (2015).

(342) Kim, K; Murphy, T.E. Strong Anisotropic Thermal Conductivity of Nanoporous Silicon. *Journal of Applied Physics* 118, 154304 (2015).

(343) Ma, J.; Gelda, D.; Valavala, K.V.; Sinha, S. Peak Thermoelectric Power Factor of Holey Silicon Films. *Journal of Applied Physics* 128, 115109 (2020).

(344) Radtke, G.A.; Hadjiconstantinou, N.G. Variance-reduced Particle Simulation of the Boltzmann Transport Equation in the Relaxation-Time Approximation. *Physical Review E*, 79, 056711 (2009).